Deliverable 2.16: Conceptual model formulation for a mechanistic based model implementing the initial SOTA knowledge (models and parameters) in existing numerical tools

Work Package 2

The project has received funding from the European Union's Horizon 2020 research and innovation programme under grant agreement No 847593.

http://www.ejp-eurad.eu/

Document information

Project Acronym	**EURAD**
Project Title	**European Joint Programme on Radioactive Waste Management**
Project Type	**European Joint Programme (EJP)**
EC grant agreement No.	**847593**
Project starting / end date	**1st June 2019 – 30 May 2024**
Work Package No.	**2**
Work Package Title	**Assessment of Chemical Evolution of ILW and HLW Disposal Cells**
Work Package Acronym	**ACED**
Deliverable No.	**D2.16**
Deliverable Title	**Conceptual model formulation for a mechanistic based model implementing the initial SOTA knowledge (models and parameters) in existing numerical tools**
Lead Beneficiary	**ENRESA(UDC)**
Contractual Delivery Date	**May 2020**
Actual Delivery Date	**July 2022**
Type	**Report**
Dissemination level	**PU**
Authors	**Javier Samper (UDC), Luis Montenegro (UDC), Laurent De Windt (MINES ParisTech), Vanessa Montoya (UFZ, SCK CEN), Jaime Garibay-Rodríguez (UFZ), Dalia Grigaliuniene (LEI), Asta Narkuniene (LEI), Povilas Poskas (LEI), Benoit Cochepin (ANDRA)**

To be cited as:

Samper J., Montenegro L., De Windt L., Montoya V., Garibay-Rodríguez J., Grigaliuniene D., Narkuniene A., Poskas P., Cochepin, B. (2022): Conceptual model formulation for a mechanistic based model implementing the initial SOTA knowledge (models and parameters) in existing numerical tools. Final version as of 15.07.2022 of deliverable D2.16 of the HORIZON 2020 project EURAD. EC Grant agreement no: 847593.

Disclaimer

Acknowledgement

This document is a deliverable of the European Joint Programme on Radioactive Waste Management (EURAD). EURAD has received funding from the European Union's Horizon 2020 research and innovation programme under grant agreement No 847593.

Status of deliverable		
	By	Date
Delivered (Lead Beneficiary)	ENRESA (UDC)	July 18, 2020
Reviewed (Reviewers)	J. Griffioen L. Martin R. Plukiene L. Vondrovic	November, 2021
Verified (WP Leader)	D. Jacques	May 23, 2022
Verified (PMO)	B. Grambow	June 02, 2022
Verified (WP Leader)	D. Jacques	July 15, 2022
Approved (PMO)	L. Théodon	July 18, 2022
Submitted to EC (Coordinator)	Andra	July 18, 2022

Executive Summary

This deliverable presents conceptual and mathematical formulations of mechanistic-based models which take into account the initial state-of-the-art knowledge on models and parameters and are linked to the existing numerical tools. The conceptual, mathematical and numerical models are proposed for the following reference systems: 1) HLW disposal cell in granite; 2) HLW disposal cell in clay; 3) ILW disposal cell in granite; and 4) ILW disposal cell in clay.

HLW disposal cell in granite

The reactive transport model of the geochemical evolution of a HLW disposal cell in granite involves the following interfaces: bentonite/granite host rock, bentonite/carbon-steel and carbon-steel canister/vitrified waste. A reference case and several sensitivity cases are proposed. The reference case starts when the 75 cm thick FEBEX bentonite buffer is saturated. Partial desaturation is not considered to be a relevant scenario for the bentonite in the HLW disposal cell in granite. Hydrogen generation due to corrosion is not expected to produce a partial desaturation of the bentonite barrier. The model is non-isothermal and accounts for the thermal transient of decreasing temperatures until the thermal pulse dissipates. The excavation damaged zone is disregarded in the base case. Its relevance will be evaluated in a sensitivity case by considering that the permeability, porosity and effective diffusion of the EDZ are larger than those of the intact Spanish Reference granitic rock. Anaerobic corrosion of the canister will be uniform, consume water and generate H_2. The main geochemical processes in the transient phase include: 1) The precipitation of iron corrosion products at the canister/bentonite interface, 2) The destabilization of montmorillonite, 3) The replacement of bentonite minerals by Fe-rich smectites and non-swelling Fe-rich phyllosilicates; and 4) The cementation of bentonite due to the precipitation of iron corrosion products and SiO_2 coming from montmorillonite transformation. Canister corrosion will lead to an increase in the concentration of dissolved Fe^{2+} and a decrease of Eh. The precipitation of the corrosion products at the canister will decrease the porosity of the bentonite and lead to pore clogging near the canister.

The model of the reference and sensitivity cases of the HLW disposal cell in granite will consider three successive periods. The first one (period I) will cover the oxic transient stage. Period II will start when the bentonite barrier is fully saturated and the anoxic conditions are prevailing. Canister corrosion, the interactions of corrosion products and the bentonite and the interactions of bentonite and granite will be considered in this period. Finally, period III will start after canister failure and will consider glass alteration and the interactions of glass with corrosion products and uncorroded iron. It is important to point out that only periods II and III will be considered in the model. This approach is consistent with that used for the HLW disposal cell in clay. A simple glass dissolution model derived from ACED Task 3 will be used for the numerical model at the scale of the disposal cell and consider the French reference SON-68 vitrified waste. The interactions of the glass and corrosion products will start in period III after canister failure. The following sensitivity cases are proposed: 1) The Belgian reference glass SM539; 2) An early breached canister with corrosion products and remaining uncorroded metallic iron; 3) MX-80 bentonite buffer 35 cm thick; 4) EDZ and a fracture zone in the granitic rock; 5) A change in the chloride concentration of the SRG porewater; and 6) The Czech Reference Crystalline rock. All the simulation runs, including the base and the sensitivity cases, will consider non-isothermal conditions. Partial desaturation of the bentonite barrier will not be considered. Models will be performed with the reactive transport codes $CORE^{2D}$ V5 and INVERSE-FADES-CORE V2, which rely on the thermodynamic database ThermoChimie v10.a.

HLW disposal cell in clay

The contribution of Subtask 4.1 to the high level waste (HLW) disposal cell in a clay sedimentary formation is based on the Belgium, Dutch and French national concepts. The first two programs rely upon supercontainers containing the vitrified waste and their steel overpack encased in prefabricated cylindrical concrete buffer materials. The concrete is made of OPC/CEM I cement and limestone aggregates. The pH has to be kept at high values during the thermal phase, and much longer beyond,

in order to keep the carbon steel overpack passivated, to limit corrosion and radionuclide release. In the French concept, the annular gap between a carbon steel sleeve (liner) and the host rock is filled with a bentonite/cement grout that imposes a corrosion-limiting environmental condition during the thermal phase only. The alkalinity of the grout is moderate (pH ~ 11) and should have been neutralized readily afterwards to prevent the dissolution of the nuclear glass under alkaline pH and radionuclide release. The nuclear glass is inserted in a carbon steel overpack. It has been decided to start from a generic configuration of the HLW disposal cell in a clay host rock as a base case and to perform variants that will fulfil more explicitly features of the Belgian/Dutch concept or features of the French concept. Eventually, a partly water desaturated degree can be modelled as an optional case with diffusion of gas (H_2, CO_2) in the system leading to cement carbonation.

Subtask 4.1 tackles with the full design of the cell over very long duration (10^5 years). The base case includes the nuclear glass (40 cm in diameter), the low alloy steel overpack (5 cm thick), the OPC-based concrete buffer (5, 30, 75 and 100 cm thick), the Callovo-Oxfordian claystone (several meter thick in the calculations). A bentonite/cement grout buffer (with a low pH cement) is an alternative composition for the 5 cm thickness. The first period for the narrative evolution and conceptual model deals with the chemical alterations before the breaching of the steel overpack (considering a thermal transient stage over 1000 y, then 25 °C). The first objective is to assess the coupled lifetime of the cement-based buffer and steel overpack as a function of the cement buffer thickness and composition. Enhanced diffusion properties are also investigated due to a transversal network of interconnected cracks within the degraded cement buffer. Glass alteration is only considered in the second period after the breaching of the canister with corrosion products and remaining uncorroded metallic iron. Different types of the corrosion products will be tested. The cement buffer is in an advanced state of chemical degradation which composition and pH will have been modelled in the first period. Eventually, a partly water desaturated degree can be modelled as an optional case with diffusion of gas (H_2, CO_2) in the system.

The main mathematical features of the reactive transport model are presented in a second section. The geochemical, mineralogical and diffusion parameters of all the materials (CEM I concrete, grout, argillite) have been compiled. Kinetic rates for carbon steel corrosion have been selected from alkaline to neutral pH values. The vitrified waste is represented by the ISG (international simple glass) model with a kinetic dissolution rate law resulting from the combination of an initial forward dissolution rate and long-term residual dissolution rate.

The modelling of Subtask 4.1 will be performed with the reactive transport codes HYTEC and iCP (interface COMSOL-PHREEQC). Those codes are interfaced with the ThermoChimie database, relevant for clayey and cement phases as well as iron corrosion products, and dataset for modelling the sorption processes of the host rock and corrosion products. The reactive transport models developed in Subtask 4.1 are able to couple different types of chemical processes for the entire multi barrier systems of the HLW disposal cell in clay host rock. The cement/clay interactions will have an effect on the integrity of the buffer but as well on the corrosion of steel overpack, e.g. by implementing a kinetic rate constant of corrosion which is pH-dependent. The cement durability cannot be separated from the evolution of the porosity and transport properties at the materials around the cement/clay interface. Carbonation may be enhanced due to the diffusion of gaseous CO_2 from the host rock, gaseous diffusion progressing faster than aqueous diffusion. The dissolution of glass is explicitly coupled with the barriers and host-rock influences through the reactive transport of dissolved silica and by the precipitation of iron silicate phases.

ILW disposal cell in clay

The contribution of Subtask 4.1 to the ILW disposal cell in a clay sedimentary formation is based on the concepts and design defined for building up a repository in indurated clay rocks (i.e. Switzerland and France). However, the defined multibarrier system (i.e waste matrix, containers, backfill material) is also common for other concepts where plastic clays are considered (i.e. Belgium and the Netherlands). Specifically, the studied disposal concept is based on a multi-barrier system including the waste matrix

(in the primary coli or drum), the disposal container, the mortar backfill in the emplacement tunnel and the clay host rock (Callovo Oxfordian). Reinforced of the tunnels walls with a shotcrete is also part of the concept. It is assumed that the disposal cell contains a number of stacked waste containers (with organic or metallic waste). In addition, a backfilling material between the waste containers is considered and in the case of the organic waste, 6 different waste packages are also inside the containers. The dimensions of the multibarrier system are 11 x 13 m without including the host rock and the EDZ. Hydration models for the four different CEM I cementitious materials (i.e. functional concrete walls of the containers, backfill mortar between the waste containers, vault backill mortar and shotcrete liner) have been performed to determine the initial hydrated cement phases in the reactive transport model. All the materials have been conceptualized as homogeneous porous media. Diffusion is the main transport mechanism and no temperature effects has been considered. Aqueous complexation reactions, mineral dissolution/precipitation reactions, cation exchange and surface complexation reactions are part of the model. When considering changes of porosity due to precipitation/dissolution of minerals, standard molar volumes are used. All this information is contained in the same chemical thermodynamic database, CEMDATA v18.1. Additional thermodynamic data for some clay minerals not found in CEMDATA is retrieved and adapted to match the same master species of CEMDATA from the latest version of the ThermoChimie database. Simulations will be for 100 000 years and will be performed with the T-H-M-C code OpenGeoSys v.6.

ILW disposal cell in granite

The contribution of Subtask 4.1 to the ILW disposal cell in a crystalline rock is based on the concepts and design available in Finland, Sweden, UK and Lithuania. The same multibarrier system considered for the ILW disposal cell in clay is used here except the host rock. In this case the Spanish granitic rock is considered and not EDZ is present. Advective flow from the host rock is considered and no temperature effects has been considered. Aqueous complexation reactions, mineral dissolution/precipitation reactions, cation exchange and surface complexation reactions are part of the model. When considering changes of porosity due to precipitation/dissolution of minerals, standard molar volumes are used. All this information is contained in the same chemical thermodynamic database, CEMDATA v18.1. Simulations will be for 100 000 years and will be performed with the T-H-M-C code OpenGeoSys v.6.

Table of content

List of Figures

List of Tables

Abbreviations

CEC: Cation Exchange Capacity

CEM: Concrete-Equivalent Mortar

EDZ: Excavated Disturbed Zone

HLW: High-Level radioactive Waste

ILW: Intermediate radioactive Waste

ISG: International Simple Glass

OPC Ordinary Portland Cement

PFE: Porosity Feedback Effect

RTM: Reactive Transport Model

SF: Spent Fuel

SRG: Spanish Reference Granite

TSO: Technical Safety Office

URF: Underground Research Facility

WMO: Waste Management Organization

1. Introduction

Most radioactive disposal strategies rely on a multiple barrier system, consisting of both natural and engineered materials, to prevent or delay the contact of groundwater with the waste and radionuclide release to the environment. Reactive transport models (RTM) can simulate the transport and chemical reactions of multiple solutes (and gases) and their chemical interactions within the multi-barrier system over various temporal and spatial scales (Bildstein *et al*., 2019). Reactive transport models have become an invaluable component in assessing the potential performance of a repository, which requires understanding how the barriers evolve in space and time (De Windt and Spycher, 2019; Idiart *et al*., 2020).

1.1. Aims and scope

Task 4 of the ACED Work Package aims at simulating the interactions of the waste packages with each other and with the immediate surrounding near field environment and the host rock within the framework of the ILW and HLW disposal concepts at the scale of a disposal cell.

The main objectives of this task include: 1) The integration of the available knowledge on critical processes and features from Tasks 1, 2 and 3 into conceptual, mathematical and numerical models to simulate the chemical evolution of representative ILW and HLW disposal concepts at the disposal cell scale; 2) The application of model abstraction techniques to describe the key features of the chemical evolution with more robust and manageable models; and 3) The identification of the interactive processes, parameters and features affecting the chemical evolution at the disposal cell scale.

Task 4 addresses the following key questions: 1) Upscaling the experimental degradation processes to the scale of a disposal cell; 2) The interactions among the chemical deterioration processes; and 3) The integration of all the knowledge gained within the ACED WP into a robust and manageable numerical model, which reflects the current state-of-the-art (SOTA).

Task 4 is divided into the following subtasks:

1) Subtask 4.1: Conceptual and mathematical formulation for a mechanistic based model (reactive transport model) to simulate the chemical evolution at the disposal cell scale.
2) Subtask 4.2: Model abstraction methodologies.
3) Subtask 4.3: Application of the model for a wide range of conditions and parameter values.

This deliverable D2.16, which is one of the two deliverables of the ACED Subtask 4.1, compiles the conceptual and mathematical formulations of mechanistic-based models which take into account the initial SOTA knowledge on models and parameters and are linked to the existing numerical tools. The conceptual, mathematical and numerical models are proposed for the following reference systems: 1) HLW disposal cell in granite; 2) HLW disposal cell in clay; 3) ILW disposal cell in granite; and 4) ILW disposal cell in clay.

It is important to point out that Subtask 4.1 tackles with the full design of the cell, not only at the waste package scale, as well as the effect of optional disposal cell concepts on the long-term (100.000 years) durability of the materials.

The resulting complexity of the models of Subtask 4.1 and the associated numerical limitations will serve as triggers for new developments in the ACED Subtask 4.2: Model abstraction methodologies. The results of the reactive transport models developed in Subtask 4.1 will be used for building abstracted models and look-up tables in Subtask 4.2. The complex model will subsequently be redefined based on the current capabilities of the existing numerical tools. Then, the implementation into these tools, using the highest level of complexity as possible at that point in time, and interpretation of the results follows. In a second step, an update of the model is foreseen based on the knowledge gained in Tasks 2 and 3

of ACED and other EURAD WPs and the numerical methods/tools in the DONUT WP. This two-step approach guarantees an early start of Tasks 4.2 and 4.3.

1.2. Structure of the report

This deliverable is divided in 7 chapters. Chapter 2 presents the conceptual, mathematical and numerical models and the computer codes for the HLW disposal cell in granite. This chapter was prepared by ENRESA (UDC) with contributions from UFZ (Vanessa Montoya) and SURAO (Antonín Vokál) to the Narrative Evolution (Section 2.2.1). Chapter 3 deals with the conceptual, mathematical and numerical models and the corresponding computer code for the HLW disposal cell in clay. It was prepared by IRSN (MINES Paris Tech) with contributions from COVRA, SCK and ANDRA. Chapters 4 and 5 present the conceptual, mathematical and numerical models, and the numerical tools of the ILW disposal cells in clay and granite, respectively. These two chapters were prepared by FZJ (UFZ) with contributions from COVRA and SCK to Chapter 4 and from VTT and LEI to Chapter 5. The integration, communalities and differences from HLW and ILW reference concepts is presented in Chapter 6.

Chapters 2, 3, 4 and 5 share the same structure. Each chapter starts with the description of the disposal cell concept. Then, the conceptual and the mathematical models are described. Next, the values of the key chemical, thermal, hydrodynamic and mechanical parameters are presented. Then, the expected outcomes of each chapter and a brief description of the reactive transport codes to be used for modelling are presented. Finally, each chapter ends with a short summary and conclusions.

2. Conceptual, mathematical and numerical models and numerical tools for the HLW disposal cell in granite

2.1. Description of the disposal cell concept

The materials and dimensions of the waste form, the overpack, the engineered barrier and the host rock selected for the HLW disposal cell in granite were defined by De Windt et al. (2020). The selected materials are the same in ACED Tasks 3 and 4. The generic configuration of the HLW disposal cell concept in granitic host rock includes (mostly adapted from De Windt *et al*., 2020):

1) The vitrified waste (40 cm in diameter) which is explicitly considered in the reactive transport model and is coupled with the rest of the engineered barrier components.
2) The overpack (5 cm thick) which is a carbon-steel canister considered as Fe(0).
3) The bentonite-base buffer (75 cm thick) which is composed of water-saturated FEBEX bentonite with a dry density of 1600 kg/m^3.
4) The Spanish Reference Granitic host rock (several meters thick in the calculations).

The layout of the representative HLW disposal cell concept in a granitic host rock is shown in Figure 2.1. The HLW disposal cell concept in granite is based on the Spanish spent fuel reference concept in granite, known as ENRESA 2000 (ENRESA, 2001). The main differences are the type of waste (vitrified waste vs. spent fuel) and the dimensions of the carbon-steel canister (45 cm in diameter for vitrified waste and 90 cm for spent fuel). In ENRESA (2001) the carbon steel canisters are placed in long horizontal disposal drifts. Canisters are surrounded by high-density bentonite. Access is accomplished by means of "main drifts" which run perpendicular to the disposal drifts. The main drifts meet at a central area, which includes the required underground infrastructure. Communications between the surface and the central underground area are accomplished by 3 access shafts and a ramp. Figure 2.2 shows a scheme of the underground infrastructure in the spent-fuel repository concept in granite.

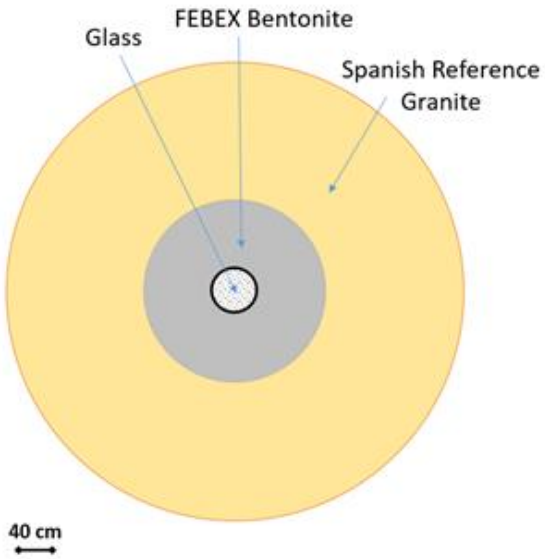

Figure 2.1. Layout of the representative HLW disposal cell concept in a granitic host rock which includes: vitrified waste (40 cm diameter), steel canister (5 cm thick), FEBEX bentonite (75 cm thickness) and Spanish Reference Granite.

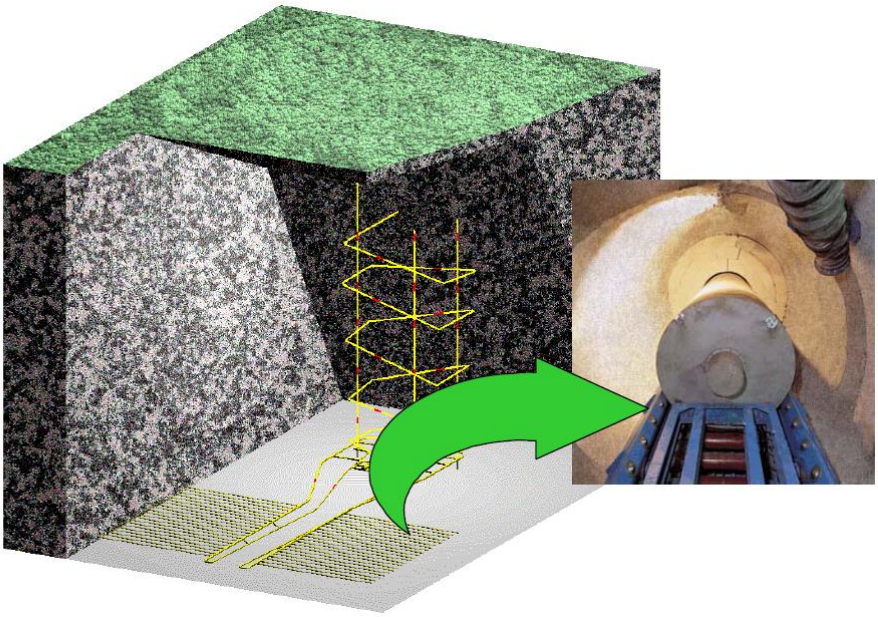

Figure 2.2. Underground installations of a radioactive waste repository in granite according to the spent-fuel Spanish Reference Concept (ENRESA, 2001).

The canister measures 4.54 m in length and 0.90 m in diameter on the Spanish spent fuel reference concept in granite (ENRESA, 2001). The thickness of the wall of the spent-fuel canister in the Spanish concept is 0.10 m at the cylindrical shield and 0.12 m at the ends, and is capable of withstanding the pressures to which it is subjected under disposal conditions. After being unloaded from the reactor, the fuel elements are temporarily stored for their thermal power to decay to a level at which they may be disposed. It should be pointed out that the thickness of the overpack in the Spanish concept is larger than that adopted for the ACED disposal cell in granite, which is equal to 5 cm to take it to the thickness of the ocerpack in the ACED disposal cell concept in clay.

Canisters are disposed in cylindrical disposal cells, constructed with blocks of precompacted bentonite of 1.700 kg/m^3 dry density to achieve a final dry density of 1.600 kg/m^3. The blocks are initially unsaturated with a gravimetric water content of 14%. The disposal drifts of 500 m in length and 2.4 m in diameter (Figure 2.3) are located at a depth of 500 m in the granitic host formation. Canisters are separated 2 m apart from each other. Galleries are separated 35 m to prevent exceeding a temperature of 100 ºC in the bentonite. The detailed dimensions of a disposal cell are shown in Figure 2.4.

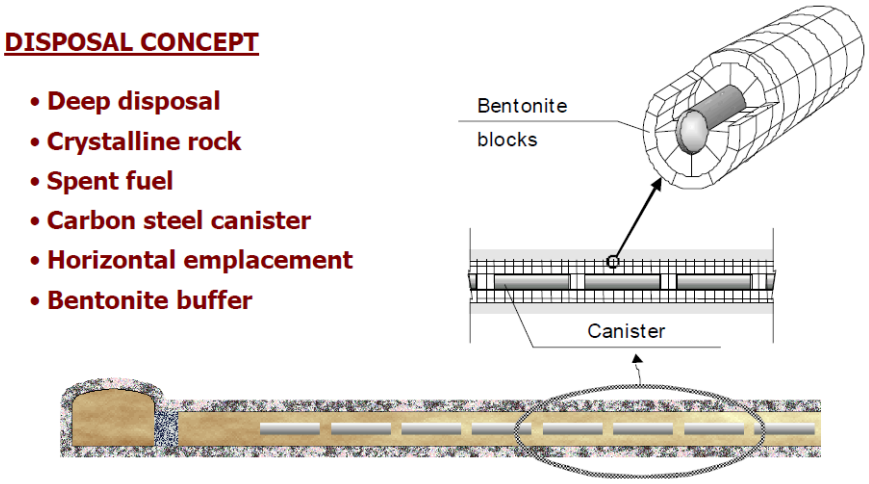

Figure 2.3. Longitudinal section of a disposal drift in the spent fuel Spanish repository concept in granite (ENRESA, 2001).

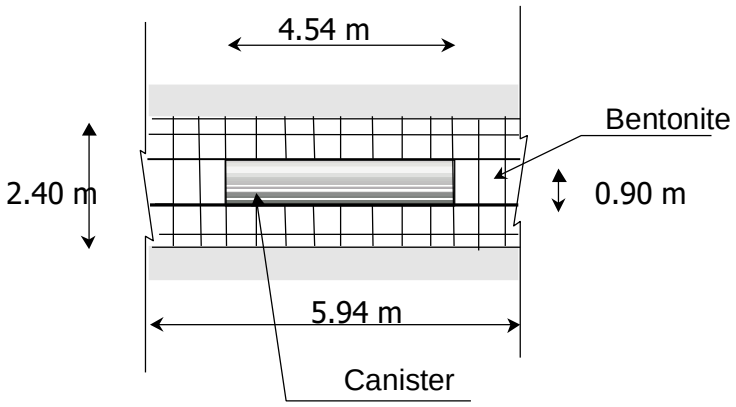

Figure 2.4. Dimensions of a disposal cell in the spent fuel Spanish repository concept in granite (ENRESA, 2001).

Disposal drifts are sealed with a 6 m long seal made of bentonite blocks and closed with a concrete plug at its entry. After completion of all the disposal drifts, main drifts, ramp, shafts and other remaining rock cavities will be backfilled with a mixture of bentonite and natural sand or an appropriate crushed material. The backfilling material will consist of 10 % bentonite (increasing up to 20 % at the top of the drifts) and suitably graded sand.

The granitic formation is selected to have a low fracture density, tectonic stability, low seismicity and appropriate geochemical conditions (see Section 2.2.1.1).

It is important to point out that the reference HLW disposal cell concept in granite is a generic concept which is not specific of any country, but aims at being representative for several national concepts. In fact, the Spanish HLW disposal cell concept in granite does not include vitrified waste. For simplification purposes, it was decided to select for the disposal cell in granite the same type of glass (French Reference SON-68 glass) as that of the HLW disposal cell in clay (see Chapter 3). One of the sensitivity cases accounts for the Belgian reference glass SM539.

2.2. Conceptual model

2.2.1. Narrative evolution

The HLW disposal cell in granite involves the following interfaces: bentonite/granite host rock, bentonite/carbon-steel and carbon-steel canister/vitrified waste. This section presents the conceptual description of the geochemical evolution of these three interfaces. The content of this section has been prepared based on EURAD Deliverables 2.4 (Neeft *et al*., 2019) and 2.5 (Deissmann *et al*., 2020). The term canister is used here to refer to the carbon-steel container to shorten the notation. The reference base case is described first. Later, several sensitivity cases are proposed for the reactive transport model of the geochemical evolution of the HLW disposal cell in granite. The model of the reference and sensitivity cases of the HLW disposal cell in granite will consider three successive periods. The first one (period I) will cover the oxic transient stage. Period II starts when the bentonite barrier is fully saturated and the anoxic conditions are prevailing. Canister corrosion, the interactions of corrosion products and the bentonite and the interactions of bentonite and granite will be considered in this period. Finally, period III will start after canister failure and will consider glass alteration and the interactions of glass with corrosion products and uncorroded iron. It is important to point out that only periods II and III will be considered in the model. These three periods are consistent with those adopted for the HLW disposal cell in clay (*Figure* 3.4). The treatment of the chemical evolution for other national programmes in crystalline rocks such as those of Sweden and Finland has been compiled in Deliverable D2.4 of ACED WP (Neeft et al., 2019).

2.2.1.1. Bentonite/granite host rock interface

Dry bentonite blocks are emplaced in a HLW disposal cell in granite. The initial porosity of the FEBEX bentonite is 0.4 and the saturation degree is about 58% (Samper *et al*., 2016). The granitic chemical pore water composition in the Spanish Reference case is of Na^+/HCO_3^- type. Cl^- and Na^+ are the dominant ions in the bentonite porewater (Samper *et al*., 2016). Dissolved sulphate in the bentonite comes from the oxidation of trace amounts of pyrite and gypsum dissolution. The initial concentrations of most solutes in the bentonite (except for dissolved HCO_3^- and SiO_2) are larger than the concentrations in the granitic porewater.

The temperature at the bentonite/granite interface just after the repository closure during the thermal transient period could range from 50 to 65 ºC. The hydration of the bentonite barrier will have progressed and the saturation degree near the canister will have increased (Figure 2.5).

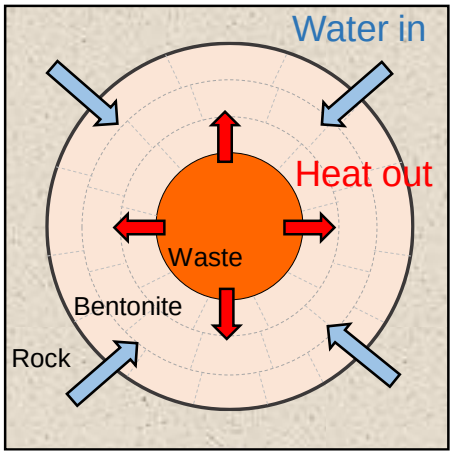

Figure 2.5. Schematic diagram of the thermal and hydrodynamic conditions in the initial heating and hydration stage of the repository.

The initial suction gradient in the bentonite/granite is very large. The granitic groundwater flow is mostly through rock fractures and the excavation damaged zone (EDZ) which may have formed around the galleries. The contribution of the granitic rock matrix is expected to be much smaller. Solute advection from the granite into the bentonite is the most relevant transport process during the period of bentonite barrier saturation. The flow of granitic groundwater into the bentonite will lead to the saturation of the bentonite. Bentonite hydration is expected to be homogenous due to the gaps between the bentonite blocks and the gaps between the bentonite barrier and the gallery wall.

The flow of granitic groundwater leads to a decrease of the concentrations of dissolved species in the bentonite. Dilution of the chemical concentration of bentonite porewater and mineral dissolution in bentonite are the two main processes produced by bentonite saturation with granitic water. Water flow decreases quickly once the outer crown of the bentonite barrier becomes near saturated. Later, bentonite hydration continues at a smaller rate and the advective solute flux becomes less relevant compared to the diffusive solute flux.

The concentration of dissolved Cl^- near the canister during the initial transient heating and hydration stage of the bentonite barrier will increase due to the evaporation of the bentonite porewater and decrease at the granite/bentonite interface due to the hydration of the barrier with granite groundwater, and also to a net movement of the dissolved Cl^- with the incoming water towards the internal part of the barrier. The concentrations of other dissolved species such as Na^+, K^+ and SO_4^{2-} will also increase near the canister due to water evaporation and decrease near the bentonite/granite interface. Mineral dissolution/precipitation and cation exchange reactions will affect the dissolved concentrations of the reactive species. Dissolved Na^+ and K^+ will exchange with Ca^{2+} and Mg^{2+} in the exchange sites (Samper *et al*., 2018). The pH in the bentonite porewater is mostly buffered by surface protonation reactions on the edges of the bentonite particles. The time evolution of the pH will also be affected by the thermal gradient and calcite dissolution/precipitation.

The transient hydration stage is estimated to last from 20 to 50 years. Once the bentonite barrier has reached nearly full saturation, most of the dissolved species in the bentonite solutes will diffuse backwards from the bentonite into the granite (Buil *et al*., 2010) under non isothermal conditions.

The thermal gradients across the bentonite barrier may last from 3000 to 5000 years. The concentration of dissolved SiO_2 in the bentonite porewater will keep decreasing due to the precipitation inducing by the decrease in temperature. The pH will increase in this stage due to the combined effect of the temperature decrease and calcite dissolution. The redox potential will decrease due to the decrease in temperature and magnetite precipitation.

The temperature in the repository after the thermal transient stage will become uniform and approximately equal to the ambient rock temperature of 32ºC (ENRESA, 2001). Calcite will keep dissolving in the bentonite except at the canister/bentonite interface where calcite will precipitate due to the increase in pH induced by canister corrosion. Far from this interface, the concentration of dissolved Ca^{2+} will decrease due to solute diffusion from the bentonite into the granite. The dissolution/precipitation of quartz and gypsum will be small. The concentrations of dissolved Na^{+}, K^{+}, Mg^{2+}, Cl^{-} and SO_4^{2-} in the bentonite porewater will decrease, reaching steady state values after tens of thousands of years. The concentration of dissolved HCO_3^{-} will increase due to calcite dissolution and HCO_3^{-} diffusion from the granite into bentonite. The concentration of dissolved iron will decrease due to magnetite precipitation and diffusion from the bentonite into the granite.

The granitic rock will be treated as an equivalent porous medium with a uniform distribution of hydraulic conductivity and porosity. Cation exchange and surface complexation reactions will not be considered in the granite. The mineralogical composition of the granite and the chemical composition of the granitic pore water are presented in Section 2.3. The excavation damaged zone (EDZ) will be disregarded in the base case. The relevance of a highly-conductive fracture zone normal to the gallery and the EDZ will be analyzed in a sensitivity case by considering an increased permeability, porosity and effective diffusion coefficient in the fracture zone and the EDZ with respect to the intact granitic rock. Small-scale fractures will be taken into account by adopting the equivalent porous medium model. Several hypotheses will be considered for the hydraulic head gradient and groundwater flow in the granite (parallel and perpendicular to the axis of the galleries). The changes in the permeability and transport parameters of the granitic rock due to mineral dissolution/precipitation will be considered in the manner indicated in Section 2.2.5.

2.2.1.2. Canister/bentonite interface

The geochemical evolution near the canister/bentonite interface is controlled by the changing environmental variables such as the bentonite degree of saturation, the temperature, the redox potential, the pH and the concentrations of dissolved species. These variables change with time during the disposal cell life from the initial post-closure stage until the system reaches anoxic conditions. Similarly, the processes occurring at the canister/bentonite interface evolve with time in response to the temporal changes in the environmental conditions of the repository. The following three phases can be distinguished: (1) Initial post-closure phase, (2) Transient phase; and (3) Saturated and anoxic phase.

The temperature at the canister surface in the initial post-closure phase in a HLW disposal cell in granite will be about 100 ºC. A thermally-induced drying at the canister-bentonite interface will occur. Oxidizing conditions will prevail with presence of oxygen. General corrosion is expected to occur with low corrosion rates. The most likely corrosion products under these oxidizing and unsaturated conditions include hematite, goethite and lepidocrocite (Gdowski and Bullen, 1988; Gdowski and Estill, 1996; Yandrisevits *et al*., 2017). No significant changes in the properties of the canister and the bentonite are expected.

The temperature at the canister/bentonite interface during the transient heating and hydration stage decreases from 100 ºC to 30ºC after 3000 years. Aerobic conditions will evolve gradually to anaerobic conditions depending on the oxygen diffusion coefficient in the bentonite, the corrosion rate, the dissolution of redox-sensitive mineral phases present in the bentonite and microbial activity. The corrosion rate will increase due to the high temperature and high humidity. Generalized corrosion will be the dominant corrosion mechanism in this phase. Localized corrosion can occur as long as oxygen is not consumed. The main geochemical processes in the transient phase include: 1) The precipitation of iron corrosion products at the canister/bentonite interface, 2) The destabilization of montmorillonite, 3) The replacement of bentonite minerals by Fe-rich smectites or non-swelling Fe-rich phyllosilicates; and 4) The cementation of bentonite due to the precipitation of iron corrosion products and SiO_2 coming from montmorillonite transformation. Microbial canister corrosion is not considered in the model because microbial processes are beyond the scope of the ACED WP. Moreover, the oxidant and reducing species produced by the water radiolysis in the bentonite could influence the canister corrosion.

However, alpha radiolysis can be disregarded for vitrified waste given the large thickness of the container and the limited travel path of alpha particles in water (40 µm).

The temperature at the canister will have dropped significantly in the saturated and anoxic phase. Oxygen will be fully consumed and reducing conditions will prevail. Anaerobic corrosion of the canister will be uniform and consume water and generate H_2. As pointed by Ortiz *et al*. (2002), it is likely that H_2(g) will migrate through the bentonite by cyclic opening and closure of discrete preferential pathways. The base case will account for the diffusion of dissolved H_2(aq) while H_2(g) migration will be neglected. H_2(g) migration could be dealt with in a sensitivity run.

The corrosion rate in this phase will be low. The final corrosion products depend on the concentrations of dissolved carbonate, Cl^- and sulphide and the redox potential. The possible products of the anaerobic steel corrosion include magnetite, iron carbonates and iron sulphides. The reduction of the bentonite structural Fe(III) could also occur, leading to the transformation of bentonite into Fe-rich non-swelling phyllosilicates such as berthierine, cronstedtite or chlorite. Sorption sites on the bentonite can be filled by ferrous ions, which can compete with radionuclides, while the high-surface area of the Fe(II)/Fe(III) corrosion products will provide additional sorption sites for radionuclides. After canister failure, the bentonite porewater will get in contact with the inner part of the canister.

Canister corrosion will lead to an increase in the concentration of dissolved Fe^{2+} and a decrease of Eh. The precipitation of the corrosion products at the canister could decrease the porosity of the bentonite and could lead to pore clogging near the canister (Samper *et al*., 2016). It is important to point out that the smectite dissolution could be relevant for the long-term geochemical evolution of the bentonite (Cama et al., 2000; Rozalén et al., 2008). Smectite dissolution will decrease the CEC and sorption capacity of the bentonite, lead to the precipitation of secondary mineral phases such as analcime and could increase the porosity of the bentonite (Fernández et al., 2009, Savage et al., 2011, Wilson et al., 2015).

The porosity changes in the bentonite due to mineral alteration processes as canister corrosion or smectite dissolution and the associated change of transport parameters are important processes which influence the geochemical evolution in the bentonite barrier. If porosity increases substantially, preferential migration pathways could develop, accelerating solute transport. On the other hand, a significant porosity decrease may inhibit solute transport. Therefore, the porosity feedback effect (PFE) could be especially relevant in the long-term geochemical evolution of a HLW disposal cell in granite. The thickness of the zone affected by pore clogging is expected to be smaller when the porosity feedback effect is accounted for (Águila *et al*., 2020).

2.2.1.3. Vitrified waste/canister interface

The interactions of the vitrified waste and the canister in a HLW disposal cell in granite are expected to be similar to those of a HLW disposal cell in clay. The alteration and dissolution of the vitrified waste in contact with water is controlled by several inter-related processes at the glass surface such as water diffusion, ion exchange between hydrogenated species and alkalis weakly bound to glass formers (also known as interdiffusion), hydrolysis of Si-O-M bonds (M = Si, Al, Zr, Fe, Zn, etc.), condensation of more or less detached species from the glass surface, and precipitation of crystalline phases from amorphous phases and soluble species. The alteration is also influenced by the canister and the formation of the corrosion products.

These mechanisms may contribute to or control the apparent dissolution rate depending on the glass composition and the chemical and physical conditions near the glass surface (Gin *et al*., 2013). As a result of these processes, the glass components and the radionuclides may: 1) Stay at the glass surface and form an amorphous, porous, hydrated material known as the gel layer; 2) Precipitate into stable crystalline phases (generally located at the surface of the gel); and 3) Remain as aqueous species.

Figure 2.6 illustrates the different stages of the alteration and dissolution of HLW borosilicate glasses as a function of time under repository conditions (Gin *et al*., 2013). Glass dissolution starts with glass

hydration and interdiffusion, which induces ion exchange between hydronium ions and alkali in the glassy matrix (De Echave *et al*., 2018). This process creates a hydrated glass layer that dissolves by hydrolysis of the silicate network. The dissolution rate of glass is maximum under these diluted conditions. This is the so-called initial stage regime. Then, the hydrolysis rate decreases due to silicon saturation and the formation of a passivating gel. Finally, secondary phases precipitate at the surface of the gel and the glass alteration rate decreases considerably, reaching the residual-rate regime. This last regime may be dominant over time, but it has been observed that in some special cases (pH > 10.5 at T = 90 ºC or at T >> 90 ºC), a resumption of glass alteration can be triggered by the precipitation of some secondary phases such as zeolites and calcium silicate hydrates.

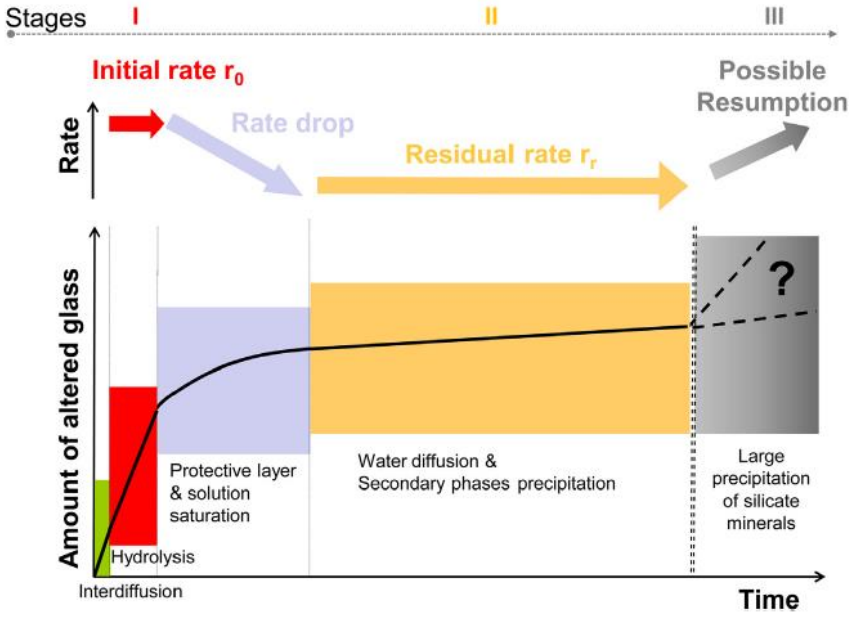

Figure 2.6. Stages of nuclear glass corrosion and related potential rate-limiting mechanisms (Gin et al., 2013).

The duration and the glass alteration rate of each stage depends on glass composition and the chemical conditions (temperature, pH, water composition) near the surface of the glass. Under repository conditions, water is the main factor causing glass degradation and radionuclide release.

The alteration and dissolution of the glass by water starts after the canister failure due mainly to corrosion processes and the lithostatic pressure. The corrosion products of the metallic container surround the glass and influence its alteration (Figure 2.7). Understanding the glass/canister interactions and their consequences on the long-term behavior of the glass requires knowing the main processes involved in the alteration of the glass. The materials surrounding the glass influence glass alteration by (Deissman *et al*., 2020): (1) Modifying the composition and properties of the solution which interacts with the glass (pH, redox potential, ionic strength and the concentrations of dissolved species); (2) Acting as a medium for the nucleation and growth of secondary mineral phases; (3) Restricting the transport of the dissolved species involved in glass alteration; and (4) Stabilizing (in the case of calcium) or destabilizing (in the case of magnesium) the hydrated glass layer.

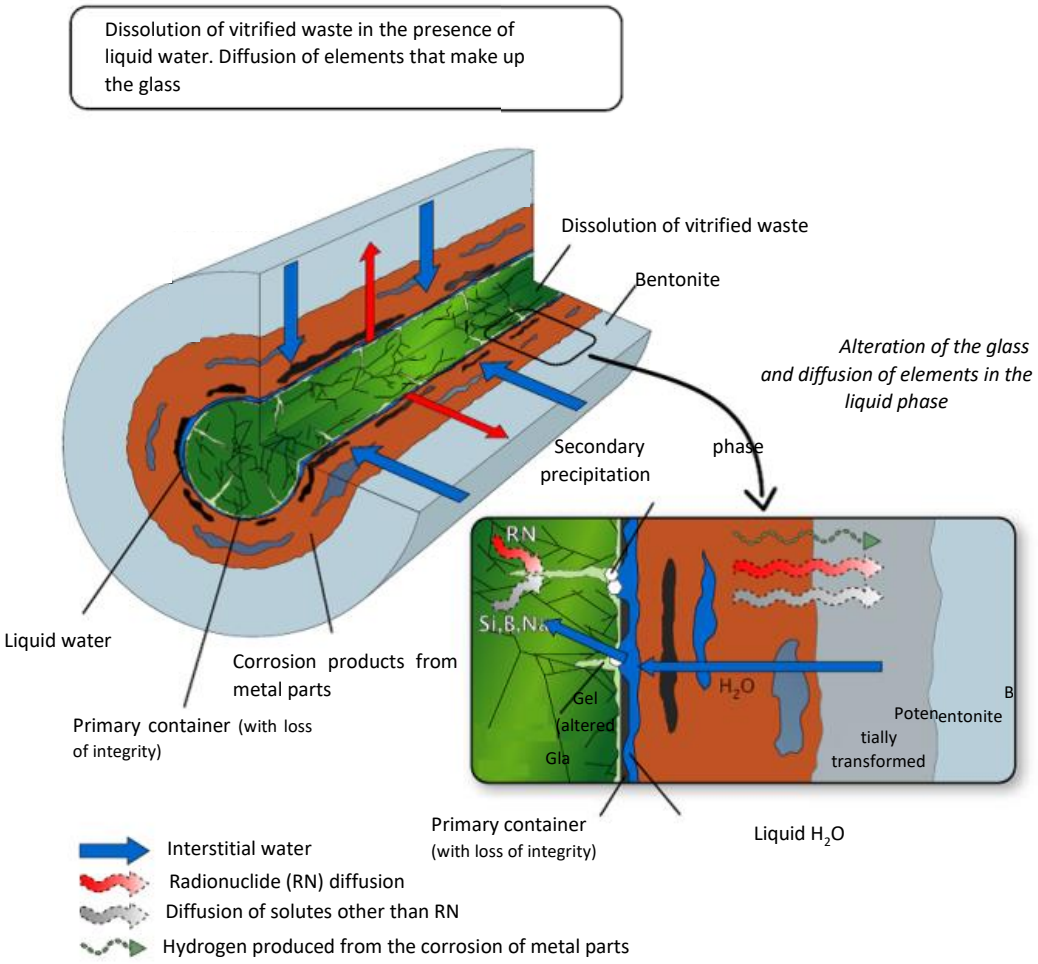

Figure 2.7. Diagram showing a glass package and the surrounding environment after container failure (modified from Deissmann et al., 2020).

The interactions of the silicon released by glass dissolution with the metallic iron and the corrosion products contribute to reach higher alteration rates with time, which are maintained over longer periods of time than in the absence of iron or corrosion products. However, this impact is only perceptible at a local scale, and is significantly attenuated as the distance from the glass to the iron source increases. The depletion of the concentrations of silicon and other elements in a lesser extent such as Al and Ca due to the interactions between silicon and corrosion products contribute to the detriment of the formation of the protective or passivating gel at the glass surface.

The possible mechanisms of glass alteration include (Rébiscoul *et al*., 2015): (1) Silicon sorption at the surface sites of the corrosion products and silica precipitation at the iron source; (2) The precipitation of iron silicates and phyllosicates such as greenalite, berthierine, cronstedtite, hectorite, saponite, nontronite and montmorillonite); (3) The modification of the structure and protective properties of the gel; and (4) The increase in pH associated with the iron corrosion reaction.

The first two mechanisms (silicon sorption/precipitation and iron silicate precipitation) have similar consequences. They both lead to the consumption of cross-linking elements by corrosion products, mainly silicon, but also to a lesser extent, aluminum and calcium. Silicon depletion may start as soon as glass alteration starts or may be delayed when the glass and the iron are not close enough. Silicon depletion leads to (Lemmens, 2001): (1) The increase of glass dissolution, and (2) The formation of a gel with less silicon content, which is, therefore, less protective. Both of these effects work to the

detriment of the formation of a protective layer, delaying the saturation of the aqueous solution needed for its formation. In the first case, the effect works by making the initial phase alteration rate, r_0, last longer, and, in the second case, by slowing down the rate drop (Figure 2.6). However, these two possible mechanisms of glass alteration (silicon sorption/precipitation and iron silicate precipitation) occur at different time scales. The impact of sorption is maintained for a very short period of time relative to the time scales considered for geological disposal while the precipitation of iron silicates may be less extensive in the short term, but potentially significant in the long term.

The third glass alteration mechanism occurs when the gel that forms at the glass surface is highly enriched in iron due to the precipitation of nano-crystalline phases within the gel. This Fe retention in the gel could modify the structure and protective properties of the gel.

The last mechanism of glass alteration is related to the increase in pH associated with the anoxic corrosion of iron in an aqueous system. The increase in pH favors the glass alteration and the formation of magnesium silicates.

Since the canister corrosion occurs from outside to inside, it can be expected that: (1) Most of the iron will react with the bentonite before canister failure, (2) There will be a small amount of uncorroded iron available to react with the glass after canister failure; and (3) The remaining iron corrosion products and iron-rich phyllosilicates will probably be less reactive towards the glass than the uncorroded iron.

The available comprehensive mechanistic glass models such as GRAAL or GLASSOL will be used in the numerical analyses of ACED Task 3. The results of such analyses will provide simpler glass dissolution models for the numerical models at the scale of the disposal cell of ACED Task 4. The vitrified waste will be considered as an equivalent porous medium accessible only to water. The ISG (international simple glass) model will be used for glass alteration. The kinetic glass dissolution includes an initial dissolution rate and a long-term residual rate.

2.2.1.4. Sensitivity cases

Sensitivity cases were selected based on the following criteria:

1) A priori expert evaluation of potentially relevant processes and features for the long-term geochemical evolution of the repository. Examples of these processes and features include: the consideration of an early breached canister, the consideration of the EDZ and a fracture zone in the host rock
2) The variants needed to account for the differences in the components, geometry and properties of the different materials in different national concepts. Examples of these variants include: vitrified waste (SM539 glass instead of SON-68 glass), the type of bentonite (FEBEX and MX80) bentonite and the host rock (Spanish granite and Check reference crystalline rock)

The proposed sensitivity cases for the reactive transport model of the geochemical evolution in a HLW disposal cell in granite are listed in Table 2.1.

Sensitivity Case 1 will consider the vitrified waste from the Belgian reference SM539 in period III. The vitrified waste will be considered as an equivalent porous medium accessible only to water. Similar to the Base Case with the French reference SON-68 vitrified waste, a simple glass dissolution model such as GRAAL or GLASSOL derived from ACED Task 3 will be used to simulate the Belgian reference SM539 alteration in the numerical models at the scale of the disposal cell of ACED Task 4. Sensitivity Case 2 will address the scenario of an early canister failure with corrosion products and remaining uncorroded metallic iron. The corroded layers will be treated as fully-saturated equivalent porous medium. The corrosion products will be derived from model results.

Compacted MX-80 bentonite (instead of FEBEX bentonite) with a thickness of 35 cm will be considered in the Sensitivity Case 3 (Figure 2.8). The Sensitivity Case 4 will consider a highly-conductive fracture zone normal to the gallery and an excavation damaged zone (EDZ) in period II (Figure 2.8). The Sensitivity Case 5 will consider in periods II and III a granitic porewater with a chloride concentration

greater than the value used in the base case. The Sensitivity Case 6 will consider the conditions of the Reference Czech crystalline rock (Figure 2.8).

Other possible sensitivity cases include: 1) Detailed glass alteration models; and 2) $H_2(g)$ migration.

Table 2.1. Base case and sensitivity cases proposed for the reactive transport model of the HLW disposal cell in granite. The sensitivity cases are variants of the base case. The specific feature of each sensitivity case is highlighted with boldface. Non-isothermal conditions are assumed in all the cases. Partial desaturation is disregarded.

Case	Period	Steel canister	Bentonite buffer	Host rock	Nuclear Glass
Base	II	Chemical form: Fe(0) Thickness = 5 cm	Water-saturated FEBEX bentonite Thickness =75 cm	Spanish Reference Granite (SRG)	No
	III	Porous, partly filled with corrosion products			SON-68 (French reference)
Sensitivity 1	II	Chemical form: Fe(0) Thickness = 5 cm	Water-saturated FEBEX bentonite Thickness =75 cm	SRG	No
	III	Porous, partly filled with corrosion products			**SM539 (Belgian reference)**
Sensitivity 2	II	**An early breached canister with corrosion products and remaining uncorroded metallic iron**	Water-saturated FEBEX bentonite Thickness =75 cm	SRG	**SON-68**
	III				SON-68
Sensitivity 3	II	Chemical form: Fe(0) Thickness = 5 cm	**MX80 bentonite Thickness = 35 cm**	SRG	No
	III	Porous, partly filled with corrosion products			SON-68
Sensitivity 4	II	Chemical form: Fe(0) Thickness = 5 cm	Water-saturated FEBEX bentonite Thickness =75 cm	**SRG with a highly fractured zone. EDZ is considered**	No
	III	Porous, partly filled with corrosion products			SON-68
Sensitivity 5	II	Chemical form: Fe(0) Thickness = 5 cm	Water-saturated FEBEX bentonite Thickness =75 cm	**SRG with a change in the Cl^- porewater concentration**	No
	III	Porous, partly filled with corrosion products			SON-68
Sensitivity 6	II	Chemical form: Fe(0) Thickness = 5 cm	Water-saturated FEBEX bentonite Thickness =75 cm	**Czech Reference Crystalline Rock**	No
	III	Porous, partly filled with corrosion products			SON-68

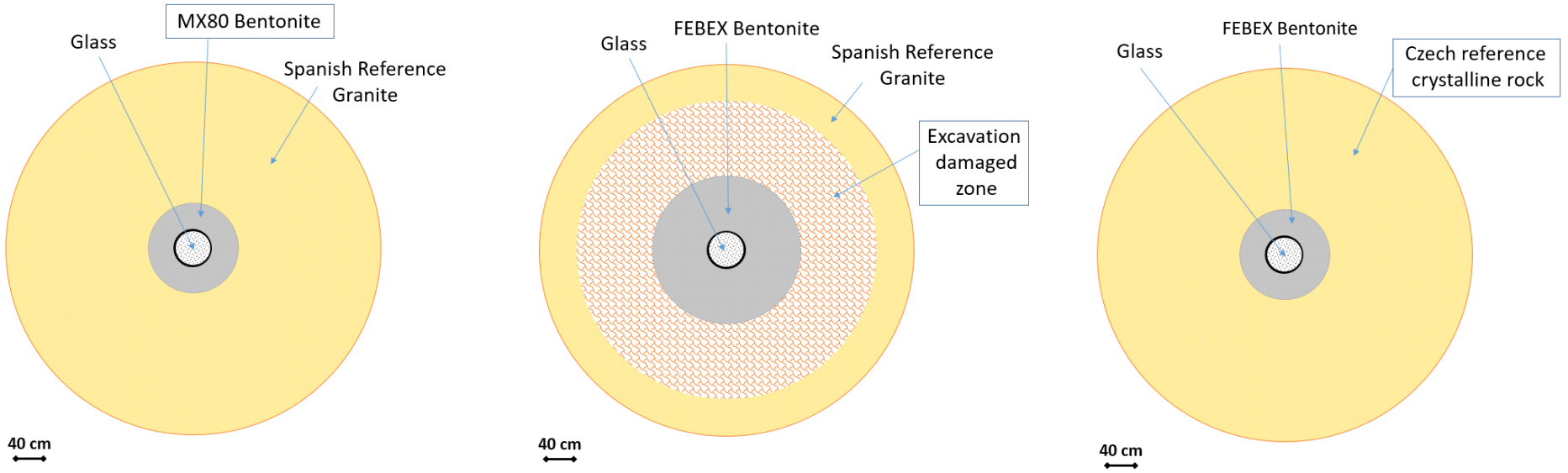

Figure 2.8. Geometric configurations of the sensitivity cases considered for a HLW disposal cell in granite. Sensitivity case 3 considers MX bentonite (35 cm thick). Sensitivity case 4 considers an excavation damaged zone (EDZ) of 1 m thickness. Sensitivity case 6 considers the Czech reference crystalline rock.

2.2.2. Hydrodynamic processes

Although the bentonite blocks are initially unsaturated, the reactive transport model of the HLW disposal cell in granite assumes that the bentonite is initially water-saturated because the bentonite barrier will become fully saturated in less than 50 years (Zheng and Samper, 2008).

The model accounts for molecular diffusion. The hydraulic conductivity of the bentonite is extremely low ($6 \cdot 10^{-14}$ m/s). Therefore, advection is negligible and solute diffusion is the main solute transport mechanism. All the water is assumed to be accessible to solutes.

Solute transport through the granite is simulated with a prescribed water flux parallel to the axis of the gallery at the bentonite/granite interface. Other assumptions will be considered in the sensitivity cases.

As pointed by Ortiz *et al*. (2002), it is assumed in the model that H_2(g) will migrate through a cyclic opening and closure of discrete preferential pathways. Therefore, partial desaturation of the bentonite barrier due to the formation of gas phase is considered to be negligible and will be disregarded in the HLW disposal cell in granite. The model will consider the diffusion of dissolved, H_2(aq).

2.2.3. Thermal processes

The thermal transient stage and the cooling of the vitrified waste will be considered in the reactive transport model of the HLW disposal cell in granite. Figure 2.9 shows the time evolution of the temperature at the canister-bentonite and the bentonite-granite interfaces computed by E. Neeft with the thermal parameters the dry and saturated FEBEX bentonite for a HLW disposal cell in granite (Neeft, 2020). These calculations are based on the requirement that the temperature in the bentonite buffer does not exceed 100°C and correspond to the following geometric configuration: 1) Vitrified waste (0.42 m of diameter), 2) Stainless steel (5 mm thick), 3) Air gap (13 mm thick), 4) Carbon-steel overpack (7.5 cm), 5) Bentonite buffer (75 cm); and 6) Granitic rock (100 m long).

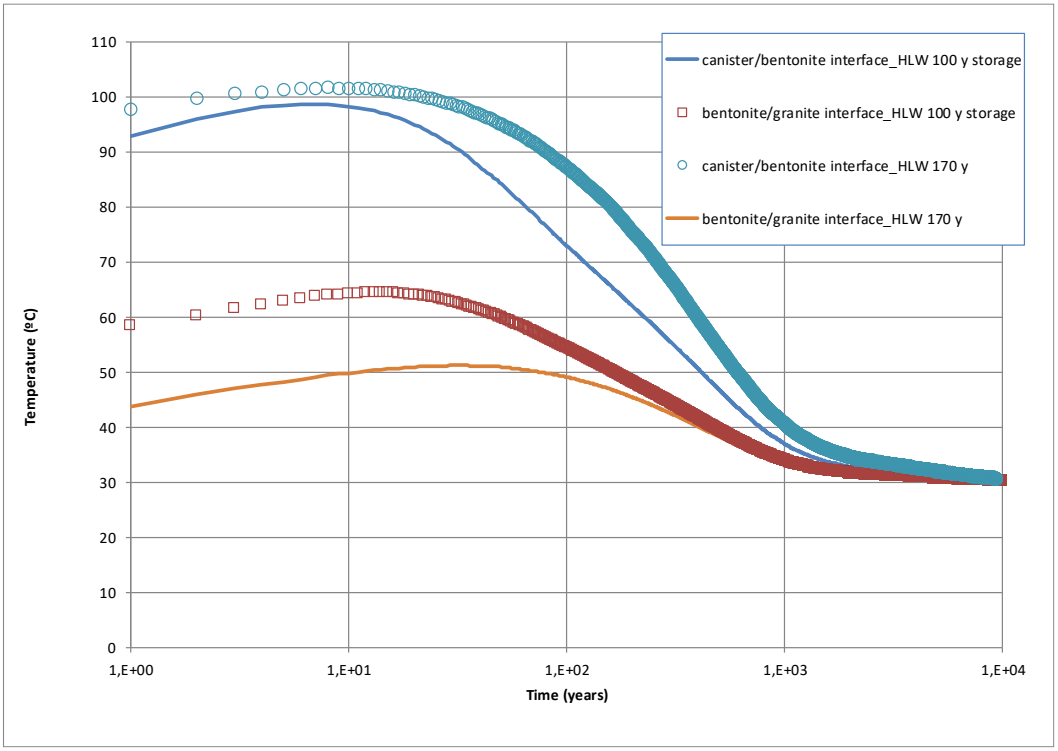

Figure 2.9. Calculated time evolution of the temperature in a HLW disposal cell in granite after 100 years of storage (wet bentonite) and 170 years of storage (dry bentonite) at the canister-bentonite and the bentonite-granite interfaces (Neeft, 2020; personal communication).

The thermal properties for the bentonite buffer and the granitic host rock used in the calculations were taken from the Spanish Reference Granite (Neeft *et al*., 2019). The time evolution of the temperatures at the canister-bentonite and the bentonite-granite interfaces was calculated by assuming a storage time during which the fuel elements are kept releasing heat and radioactivity to acceptable levels. The considered storage times range from 100 to 170 years (Neeft, 2020).

A calculated temperature of 32°C, which is almost the undisturbed granitic host rock temperature, is achieved after about 3000 years at the interface between carbon steel and wet bentonite (after 100 years of storage). The heat emission of the waste dries the bentonite. This drying reduces the thermal conductivity of bentonite and increases the period in time to achieve 32°C. This calculated temperature is reached at the interface between carbon steel and dry bentonite (after 170 years of storage) in less than 5000 years.

All the runs (base and sensitivity cases) in the reactive transport model of the HLW disposal cell in granite will be non-isothermal.

2.2.4. Chemical processes

The conceptual geochemical model of the HLW disposal cell in granite includes the following processes: 1) Carbon-steel canister corrosion, 2) Vitrified waste dissolution, 3) Aqueous complexation; 4) Acid/base; 5) Redox; 6) Mineral dissolution/precipitation; 7) Cation exchange of Ca^{2+}, Mg^{2+}, Fe^{2+}, Na^{+} and K^{+}; and 8) Surface complexation of H^{+} on three types of sorption sites (strong sites: $S^{s}OH$, weak 1 sites: $S^{w1}OH$ and weak 2 sites: $S^{w2}OH$). While aqueous complexation, acid/base, redox and dissolution/precipitation reactions take place in all the materials considered in the HLW disposal cell, cation exchange and surface complexation reactions occur only in the bentonite barrier.

The geochemical system is defined in terms of primary species (H_2O, H^{+}, $O_2(aq)$, Ca^{2+}, Mg^{2+}, Na^{+}, K^{+}, Fe^{2+}, Al^{3+}, Cl^{-}, SO_4^{2-}, HCO_3^{-}, $SiO_2(aq)$, $S^{s}OH$, $S^{w1}OH$, $S^{w2}OH$). The secondary aqueous species will be identified from speciation runs performed with EQ3/6 (Wolery, 1992). Minerals will be assumed at chemical equilibrium or kinetically-controlled. The Gaines-Thomas convention will be used for cation exchange reactions (Appelo and Postma, 1993). The secondary surface complexation species will be ($S^{s}OH^{2+}$, $S^{s}O^{-}$, $S^{w1}OH^{2+}$, $S^{w1}O^{-}$, $S^{w2}OH^{2+}$, $S^{w2}O^{-}$). Surface complexation reactions will be modelled with the non-electrostatic triple-site sorption model of Bradbury and Baeyens (1997) and (2005).

All the reactions are assumed at chemical equilibrium, except for the dissolution/precipitation of some minerals which are kinetically controlled. The following kinetic rate law will be used for carbon-steel corrosion, smectite dissolution, and the precipitation of magnetite, analcime, and Fe-phyllosilicates (cronstedtite):

$$r_m = s_m k_m e^{\frac{-Ea}{RT}} \left(\prod_{i=1}^{N_T} a_i^{p_{mi}} \right) \left| \left(\Omega_m^{\theta} - 1\right)^{\eta} \right| \qquad [\ 2.1\ ]$$

where r_m is the dissolution/precipitation rate (mol/m²/s), k_m is the kinetic rate constant (mol/m²/s) at 25ºC, E_a is the activation energy, R is the gas constant (J/K·mol), T is the temperature (K), Ω_m is the saturation index which is equal to the ratio of the ion activity product to the equilibrium constant (dimensionless), Ɵ and η are empirical parameters, $|\cdot|$ is the absolute value operator, and $\prod_{i=1}^{N_T} a_i^{p_{mi}}$ is a catalytic term which accounts for the activities a_i of the aqueous species and p_{mi} is the exponent for the i-th aqueous species in the m-th mineral phase dissolution reaction. Variable s_m is taken equal to -1 for precipitation and 1 for dissolution to ensure that the dissolution/precipitation rate is always positive for dissolution and negative for precipitation for any values of the parameters Ɵ and η.

The dissolution/precipitation rate in mol/m^2/s, r_m, is multiplied by the mineral specific surface area, σ, to get the dissolution/precipitation rate in mol/m^3/s, R_m. The specific surface area σ is defined as the surface area of the mineral per unit fluid volume.

2.2.5. Porosity feedback effect

The changes in porosity caused by mineral dissolution/precipitation and the associated changes in flow, transport and chemical parameters of porous and fractured media are relevant for the geochemical time-evolution of natural and engineered underground systems. The realistic representation of natural systems requires modeling tools accounting for porosity changes.

Águila *et al*. (2020) investigated the relevance of the dynamic update of the flow, transport and chemical parameters in reactive transport models with mineral dissolution/precipitation. CORE^{2D}V5 was developed to take into account the porosity feedback effect (PFE) due to mineral dissolution/precipitation under isothermal and non-isothermal conditions. Now, CORE^{2D}V5 considers porosity changes and updates flow, transport and chemical parameters. The porosity, ϕ, is updated each time step from the computed values of the mineral volume fractions, f_m, according to:

$$\phi = 1 - \sum_{m=1}^{N_p} f_m \qquad [\ 2.2\ ]$$

The changes in the permeability of the granite are calculated from the Kozeny-Carman equation (Carman, 1937). This is one of the most widely accepted permeability-porosity relationships which relates the properties of the porous medium to the flow resistance in pore channels. The Kozeny-Carman equation provides an expression to relate the permeability, k, to the porosity through:

$$k = k_0 \frac{(1-\phi_0)^2}{(1-\phi)^2}\left(\frac{\phi}{\phi_0}\right)^3 \qquad [\ 2.3\ ]$$

The pore diffusion coefficients are updated by using the Archie's law (Archie, 1942) which describes the ratio between the effective diffusion of a solute in a porous medium, D_e, and its diffusion coefficient in pure water, D_0 which depends on the tortuosity of the medium (t) and the constrictivity (d). This ratio is often described in terms of the geometric factor:

$$\frac{D_e}{D_0} = \frac{\delta}{\tau} = \phi^m \qquad [\ 2.4\ ]$$

The specific surface of the minerals in saturated porous media (expressed as the surface of mineral per unit volume of water) is updated each time step according to:

$$A_m^{t+1} = A_m^t \frac{\phi^t}{\phi^{t+1}} \qquad [\ 2.5\ ]$$

The change in the mineral specific surface will be taken into account for kinetic mineral dissolution/precipitation and for updating the CEC and the density of surface complexation sites.

Equations [2.3], [2.4] and [2.5] are commonly implemented in reactive transport codes in a continuum approach to update flow and transport parameters from porosity changes provoked by mineral dissolution/precipitation (Steefel *et al*., 2015; Hommel *et al*., 2018; Poonoosamy *et al*., 2018). Although these empirical relationships may not be representative of the pore scale processes (Seigneur *et al*., 2019), they have proven useful to provide a quantitative interpretation of observational data under dynamic conditions.

Águila *et al*. (2020) concluded that the PFE is especially relevant in long-term problems with mineral dissolution/precipitation leading to strong porosity changes. The PFE was analyzed with a non-isothermal geochemically-reactive transport model of the long-term ($4{\cdot}10^4$ years) interactions of compacted bentonite with corrosion products and concrete in a spent fuel radioactive waste repository

in clay. The model predicts pore clogging in the concrete and at the concrete-clay interface. The thickness of the zone affected by pore clogging computed with the PFE is smaller than that computed without the PFE.

2.3. Mathematical model

2.3.1. Equations

This section presents the mathematical formulation of solute and heat transport and the geochemical reactions considered in the reactive transport of the HLW disposal cell in granite.

2.3.1.1. Transport of conservative solutes

Dissolved species in saturated media are subject to various physical and chemical transport and accumulation processes. The main transport processes are: (1) advection, (2) molecular diffusion and (3) hydrodynamic dispersion. Each of these processes produces a solute mass flux F (mass of solutes crossing a unit surface area of medium per unit time).

Advection refers to solute migration associated to water flow. Solutes move with water. If water flows at a specific discharge q (volumetric water flux), the advective mass flux F_A is given by:

$$\mathbf{F}_A = \mathbf{q}c \qquad [\ 2.6\ ]$$

where c is the solute concentration, usually expressed as solute mass (gram or mol in reactive solute transport) per unit fluid volume. Solutes migrate at an average velocity v given by:

$$\mathbf{v} = \frac{\mathbf{q}}{\theta} \qquad [\ 2.7\ ]$$

where θ is the volumetric water content which is equal to the porosity ϕ for saturated media. The advective mass flux can also be obtained as:

$$F_A = \theta v c \qquad [\ 2.8\ ]$$

Molecular diffusion is a transport mechanism related to the continuous Brownian motion of solute and fluid molecules. For pure water, molecular diffusion produces a mixing effect which obeys Fick's Law. This law states that solute flux due to diffusion F_D is proportional to the concentration gradient ∇c:

$$\mathbf{F}_D = -D_0 \nabla c \qquad [\ 2.9\ ]$$

where D_0 is the molecular diffusion coefficient in water. Solutes in a porous medium can only diffuse along fluid pores following tortuous paths. The effective molecular diffusion coefficient in a porous medium, D_e, is smaller than that for pure water (see Eq. [2.4]).

The diffusive flux in porous media is given by:

$$F_D = -D_e \nabla c \qquad [\ 2.10\ ]$$

In addition to molecular diffusion there is a mixing phenomenon known as hydrodynamic dispersion which also produces a solute flux, $\mathbf{F}_H$.

The equation governing solute transport through porous media is derived from the principle of mass conservation. This principle states that for any reference elementary volume of medium, the net flux plus sink/source terms must be equal to the time rate of change of the solute mass contained in the reference volume. Solute mass per unit volume of medium is equal to θc. The net mass flux is given by minus the divergence of the total flux vector. Therefore, mass conservation leads to the following equation:

$$-\nabla\cdot\left(\mathbf{F}_A+\mathbf{F}_D+\mathbf{F}_H\right)=\frac{\partial(\theta c)}{\partial t} \qquad [\ 2.11\ ]$$

where $\nabla\cdot(\ )$ is the divergence operator which when applied to a vector F of components (F_x, F_y, F_z) is equal to:

$$\nabla\cdot(\mathbf{F})=\frac{\partial F_x}{\partial x}+\frac{\partial F_y}{\partial y}+\frac{\partial F_z}{\partial z} \qquad [\ 2.12\ ]$$

Substitution of mass fluxes $\mathbf{F_A}$ (Eq. [2.6]), $\mathbf{F_D}$ (Eq. [2.9]) and $\mathbf{F_H}$ into the continuity Eq. [2.11] leads to:

$$\nabla\cdot\left(\theta\mathbf{D}\nabla c\right)-c\nabla\cdot\mathbf{q}-\nabla c\cdot\mathbf{q}=\frac{\partial(\theta c)}{\partial t} \qquad [\ 2.13\ ]$$

Possible solute sinks and sources are added to the left-hand-side of the equation. For a fluid source of water flux w (per unit volume of medium) having a concentration c^* and a solute sink/source term R (solute mass added per unit time and unit fluid volume) the transport equation becomes:

$$\nabla\cdot\left(\theta\mathbf{D}\nabla c\right)-\mathbf{q}\cdot\nabla c+w\left(c^*-c\right)+\theta R=\theta\frac{\partial c}{\partial t} \qquad [\ 2.14\ ]$$

2.3.1.2. Heat transport

Heat transport in porous media is governed by: (1) Conduction in the solid matrix, (2) Transport by the fluid phase (advection), (3) Conduction in the fluid phase; and (4) Heat exchange between the two phases depending on their temperature difference. The first phenomenon would produce a heat equation relative to the mean temperature T_s of the solid. The second and third would resemble the dispersion equation for the fluid with the fluid temperature T playing the role of the concentration. The fourth would be related to the exchange mechanisms between the solid and the liquid phase. However, in practice, except for a few cases, it can be safely assumed that the temperature of the solid and that of the fluid become identical almost at once, and that there is only one temperature T in the porous medium. All the theory on solute transport can then be applied to heat transfer in porous media.

A single temperature is calculated for the porous medium. Heat transport processes include advection in a manner similar to that of the solutes and dispersion. Pure conduction in the two phases, solid plus liquid, takes the place of molecular diffusion, while the heterogeneity of the real velocity gives rise to an anisotropic “fictitious thermal conductivity”, equivalent to the mechanical dispersion, which experience shows to be a linear function of the modulus of the velocity vector (De Marsily, 1986).

The principle of heat conservation (analogous to the solute mass balance) for a saturated porous media is the following:

$$\nabla\cdot\left(\boldsymbol{\lambda}\nabla T-\rho_w c_w\mathbf{q}T\right)=\phi\rho_w c_w\frac{\partial T}{\partial t}+(1-\phi)\rho_s c_s\frac{\partial T_s}{\partial t}=\rho_m c_m\frac{\partial T}{\partial t} \qquad [\ 2.15\ ]$$

where λ is the thermal conductivity tensor, T is temperature, ϕ is porosity, ρ_w is the mass of water per unit volume, c_w is the specific heat of the water, ρ_s and c_s are the mass per unit volume and specific heat of the solid at a temperature $T_s = T$, and ρ_m and c_m are the mass per unit volume and specific heat of the entire porous medium (water plus solid) so that:

$$\rho_m c_m=\phi\rho_w c_w+(1-\phi)\rho_s c_s \qquad [\ 2.16\ ]$$

The tensor of thermal conductivity λ combines the isotropic conductivity λ_0 of the porous medium (water plus solid) in the absence of flow and a term for the macrodispersivity linked to the heterogeneity of the velocity, which is a linear function of this velocity.

2.3.1.3. Chemical reactions

A chemical system is made up of a set of atomic constituents or elements. A chemical species is defined as any chemical entity distinguishable from the rest due to its elemental composition and by the phase at which it is present. Not all species are needed to describe fully the chemical system. The subset of species which is strictly necessary is made up of what are known as components. These components can be chosen arbitrarily among all species. Although the N_E atomic constituents could serve as a set of components, they are never used as such because the constituents themselves are rarely present in aqueous phases. For this reason, it is more convenient to select as components a subset of N_C chemical species. These species are also known as the primary species.

CORE^{2D} v5 allows the user to define a set of aqueous species in the database as a primary species. The code checks that this set of species are initially independent and are able to form together with the sorbed primary species the rest of species (such as secondary species or aqueous complexes, minerals, gases and surface complexes) as a linear combination of primary species:

$$Q_j^S = \sum_{i=1}^{N_C} \nu_{ji} Q_i^P \qquad j = 1....N_s \qquad [\ 2.17\ ]$$

where Q_j^s and Q_i^P are the chemical formulae of the j-th secondary species and the i-th primary species respectively; γ_{ij} is the stoichiometric coefficient of the i-th primary species in the dissociation reaction of the j-th species and N_s is the total number of secondary species.

In CORE^{2D} v5 all the reactions are assumed at chemical equilibrium, except for the mineral dissolution/precipitation which can also be kinetically-controlled. At a given pressure and temperature, the Gibbs free energy of the system reaches a minimum, and the system cannot spontaneously carry out any chemical work. The derivation from this principle of equilibrium leads to the well-known Mass-Action law expression:

$$\mathbf{K}_{j(p,T)} = e^{-\frac{\Delta G^\circ}{RT}} \equiv a_j^{-1} \prod_{i=1}^{N_T} a_i^{\nu_{ji}} \qquad [\ 2.18\ ]$$

where $\mathbf{K_j}$ is the equilibrium constant which depends on the pressure and temperature of the system, $\mathbf{a_i}$ and $\mathbf{a_j}$ are the thermodynamic activities of the i-th and j-th species, respectively, N_C is the total number of primary species and γ_{ij} is the stoichiometric coefficient of the i-th primary species in the dissociation reaction of the j-th species. As a convention the stoichiometric coefficients are positive for species on the right hand side of the reaction, and negative for those on the left hand side. The reactions are always written as the dissociation of a mole of secondary species.

2.3.1.4. Aqueous complexation reactions

The continuous motion of dissolved ions together with their large number per unit volume cause numerous collisions making possible the formation of ion pairs and/or dissolved complexes which usually have an ephemeral live (on the order of 10^{-10} s). Since these reactions are almost instantaneous, they can be effectively considered as equilibrium reactions. The equilibrium constant relates the average number of ions pairs or complexes which are being formed. Applying the Mass-Action Law to the dissociation of the j-th secondary species, one has:

$$K_j = a_j^{-1} \prod_{i=1}^{N_c} a_i^{\nu_{ji}} \qquad [\ 2.19\ ]$$

where a_i and a_j are the thermodynamic activities of the species j and i, respectively, and ν_{ji} is the stoichiometric coefficient of the i-th primary species in the j-th secondary species. This equation allows one expressing the concentration of secondary species or aqueous complexes x_j in terms of primary species concentrations c_i:

$$x_j = K_j^{-1}\gamma_j^{-1}\prod_{i=1}^{N_c} c_i^{\nu_{ji}}\gamma_i^{\nu_{ji}} \qquad [\ 2.20\ ]$$

where x_j and c_i are molal concentrations and γ_j and γ_i are thermodynamic activity coefficients.

For non-concentrated solutions (less than 1 mol/kg) the value of the activity coefficient of the i-th aqueous species can be calculated according to the extended Debye-Hückel equation:

$$\log \gamma_i = -\frac{Az_i^2(I)^{\frac{1}{2}}}{1+Ba_i(I)^{\frac{1}{2}}} + bI \qquad [\ 2.21\ ]$$

where I is the ionic strength of the solution; z_i and a_i are the electric charge and the ionic radius in solution of the i-th aqueous species, respectively; A and B are constants which depend on temperature and dielectric constant of water, and b is a constant of a given species determined from fitting experimental data. The values of A, B and b at different temperatures are tabulated in Helgeson and Kirkham (1974). The value of the ionic strength is calculated as:

$$I = \frac{1}{2}\sum_{i=1}^{N_T} c_i z_i^2 \qquad [\ 2.22\ ]$$

The activity of water can be calculated according to Garrels and Christ (1965) as:

$$a_{H_2O} = 1 - 0.018\sum_{i=2}^{N_T} c_i \qquad [\ 2.23\ ]$$

where summation index i includes all the species in solution except water. The expressions of log γ_i and a_{H2O} are only valid for diluted solutions (I ≤ 0.1 M).

Accordingly, the total dissolved concentration of a given component C_k can be written in an explicit form as a function of the concentration of the N_C primary species:

$$C_k = c_k + \sum_{j=1}^{N_x}\nu_{jk}x_j = c_k + \sum_{j=1}^{N_x}\nu_{jk}K_j^{-1}\gamma_j^{-1}\prod_{i=1}^{N_c} c_{ji}^{\nu_{ji}}\gamma^{\nu_{ji}} \qquad [\ 2.24\ ]$$

where N_x is the number of secondary species. Notice the difference between the concentration of primary species c_k and the total concentration C_k. As shown before, the chemical composition of an aqueous system containing N_E species can be expressed in terms of the concentrations of N_C components (primary species). This is of great relevance for reactive solute transport modeling because instead of N_E transport equations only N_C equations have to be solved. The concentration of the N_x secondary species can be explicitly computed from the concentrations of primary species. This results in a significant reduction of computing time.

2.3.1.5. Acid-base reactions

These reactions include those involving the transfer of protons H^+. Proton concentration in the solution is obtained by defining a new variable measuring the proton excess or total proton concentration, C_H, which is defined as:

$$C_H = c_{H^+} + \sum_{j=1}^{N_x} \nu_{jH} x_j \qquad [\ 2.25\ ]$$

where c_{H+} is the concentration of free protons and ν_{jH} are the stoichiometric coefficients of protons in the acid-base reactions of formation of secondary aqueous species. The total concentration, C_H, represents the net proton balance or "proton excess" of all acid-base reactions taking place in the solution. Contrary to the total concentrations of all other components, C_H in some cases may take on negative values.

2.3.1.6. Redox reactions

The transfer of electrons between two different atoms changes their chemical valence. This transfer is known as an oxidation-reduction reaction. The redox potential of a chemical system can be described by means of redox pairs such as O_2/H_2O, SO_4^{2-}/H_2S, Fe^{3+}/Fe^{2+}, etc. Usually, the redox potential is governed by the most abundant redox pair. Even though this approach seems to be the most adequate, it is rarely used due to the difficulty of obtaining the analytical concentrations of the two species of a redox pair.

Among the different alternative approaches to describe redox reactions the external approach considers hypothetical electron activity as an aqueous component or a master species. Contrary to the protons, which exist in reality as dissolved species, the electron concentration is a hypothetical variable. The definition of this virtual concentration is useful because it allows to complete the redox half-reactions and treat them as the rest of the chemical reactions in the aqueous phase. Each half redox reaction is completed by adding electrons as transferable species. The activity coefficient of this hypothetical species is assumed to be equal to one. It is possible then to define the total electron concentration C_e as:

$$C_e = c_e + \sum_{j=1}^{N_x} \nu_{je} x_j \qquad [\ 2.26\ ]$$

where c_e is the "free electron concentration" and ν_{je} is the stoichiometric coefficient of the electron in j-th half-redox reaction.

Similar to acid-base reactions, the total concentration C_e represents the net electron balance or "electron excess" for all redox reactions. Thus, C_e may take on positive or negative values. In this way, redox reactions can be treated in the same way as the rest of equations. Once the "free electron concentration", c_e, is known, the calculation of other redox indicators, such as the counter-part species of a redox pair, the concentration of dissolved oxygen ($O_2(aq)$), or the fugacity of oxygen gas ($O_2(g)$), can be easily calculated by considering them as secondary species.

2.3.1.7. Cation exchange

Cation exchange takes place when free cations in solution exchange with interlayer cations. This process can be described as an equilibrium reaction between an exchangeable cation and an exchange site. The equilibrium constant is usually known as the exchange coefficient because its value depends on the ionic strength of the solution. A general expression for cation exchange reactions according to the Gaines-Thomas convention is (Appelo and Postma, 1993):

$$\frac{1}{\nu_i} S_i + \frac{1}{\nu_j}\left(X_{\nu_j} - S_j\right) \Leftrightarrow \frac{1}{\nu_i}\left(X_{\nu_i} - S_i\right) + \frac{1}{\nu_j} S_j \qquad [\ 2.27\ ]$$

where ν_i and ν_j are the stoichiometric coefficients (equal to their charges) of dissolved and interlayer cations, respectively; S_i and S_j denote dissolved cationic species and $\left(X_{\nu_i} - S_i\right)$ and $\left(X_{\nu_j} - S_j\right)$

represent exchange sites or exchange interlayer cations. The equilibrium equation for cation exchange is obtained from the Mass Action Law:

$$K_{ij}^{*} = \frac{\overline{w}_i^{1/\nu_i} \cdot a_j^{1/\nu_j}}{\overline{w}_j^{1/\nu_j} \cdot a_i^{1/\nu_i}} \qquad [\ 2.28\ ]$$

where K_{ij}^{*} is the exchange coefficient or selectivity, a_j is the activity of the j-th dissolved species and $\overline{W}_i$ is the activity of the i-th exchanged species. Activities of dissolved cations are related to concentrations according to the Debye-Hückel theory. Activities of interlayer cations are approximated by their equivalent fractions of the number of exchange sites. Thus, the activity of the interlayer cation $\overline{W}_i$ is assumed to be equal to its equivalent fraction β_i, and is calculated as:

$$\overline{w}_i \cong \beta_i = \frac{w_i}{\sum_{i=1}^{N_w} w_i} \qquad [\ 2.29\ ]$$

where w_i is the concentration of the i-th interlayer cation and N_W is the total number of the interlayer cations. The sum of concentrations of surface sites or interlayer cations is the so-called cation exchange capacity (CEC). Substituting Equation [2.29] into Equation [2.28] yields the general equation for cation exchange:

$$K_{ij}^{*} = \frac{\beta_i^{1/\nu_i} \cdot (c_j \gamma_j)^{1/\nu_j}}{\beta_j^{1/\nu_j} \cdot (c_i \gamma_i)^{1/\nu_i}} \qquad [\ 2.30\ ]$$

where the activity of each dissolved species a_i has been expressed as the product of its concentration c_i time its activity coefficients γ_i .From this equation, the equivalent fraction of the j-th interlayer cation can be expressed as:

$$\beta_j = \left(K_{ij}^{*}\right)^{-\nu_j} c_j \gamma_j \left(\frac{\beta_i}{c_i \gamma_i}\right)^{\nu_j/\nu_i} \qquad j = 1,2,\cdots,N_w \qquad [\ 2.31\ ]$$

From the definition of equivalent fraction, one has:

$$\sum_{j=1}^{N_w} \beta_j = 1 \qquad [\ 2.32\ ]$$

Substituting Equation [2.31] into Equation [2.32] results in:

$$\sum_{j=1}^{N_w} \left(K_{ij}^{*}\right)^{-\nu_j} c_j \gamma_j \left(\frac{\beta_i}{c_i \gamma_i}\right)^{\nu_j/\nu_i} = 1 \qquad [\ 2.33\ ]$$

which for given dissolved concentrations c_j can be solved for the single unknown β_i. This equation is quadratic when cation exchange involves only homovalent and divalent cations. However, when cation exchange involves also trivalent cations a cubic equation is obtained. Once the equivalent fraction β_i is known the rest of exchange fractions can be calculated from Equation [2.31]. The concentration of the

i-th exchanged cation w_j (in moles per liter of fluid) can be obtained from the i-th equivalent fraction according to Equation [2.29] through:

$$w_j = \beta_j \, CEC \, \rho_s \, z_j \frac{(1-\phi)}{100\phi} \qquad [\ 2.34\ ]$$

where CEC is the cation exchange capacity (usually measured as the number of milli equivalents of cations per 100 gram of solid), ϕ is the porosity, ρ_S is the density of the solids (Kg of solids per dm^3 of solids) and z_j is the cation charge.

2.3.1.8. Mineral dissolution/precipitation reactions

Under equilibrium conditions, mineral dissolution/precipitation reactions can be described by the Mass Action Law which states that:

$$X_m \lambda_m K_m = \prod_{i=1}^{N_c} c_i^{\nu^p_{mi}} \gamma^{\nu^p_{mi}} \qquad [\ 2.35\ ]$$

where X_m is the molar fraction of the m-th solid phase, λ_m is its thermodynamic activity coefficient (X_m and λ_m are taken equal to 1 for pure phases), c_i and γ_i are the concentration and activity coefficient of the i-th dissolved primary species, ν^p_{mi} is the stoichiometric coefficient in the m-th solid phase, and Km is the corresponding equilibrium constant. The equilibrium condition provides a relationship among the concentrations of the involved aqueous species. The mass transfer needed to achieve this condition is not specified. In fact, the equation does not include the concentration of the m-th solid phase, and therefore the amount of dissolved/precipitated mineral cannot be computed explicitly. This is an important feature of this type of reactions that is not shared neither by homogeneous reactions nor by the rest of heterogeneous reactions.

2.3.1.9. Sorption

Many minerals such as metal oxides, hydroxides, and layered silicates exhibit electrically charged surfaces in the presence of natural waters. These surfaces contain ionizable functional groups as the silanol groups in hydrated silica (Si-OH), being responsible for chemical reactions at the surface.

The sorption of solutes at the solid surfaces can be described by a set of chemical reactions taking place between aqueous species and specific surface sites (surface complexation). These surface reactions include proton exchange, cation and anion binding via ligand exchange at surface hydroxyl sites (represented here as XOH to avoid confusion with other chemical species). The sorption of a metal, M, can be represented as:

$$XOH + M^{z+} = XOM^{(z-1)+} + H^+ \qquad [\ 2.36\ ]$$

At equilibrium, the sorption reactions can be described by the Mass Action Law equation:

$$K_{int\,r} = \frac{[XOM^{(z-1)+}]\, a_{H^+}}{[XOH]\, a_{M^{z+}}} \qquad [\ 2.37\ ]$$

where K_{intr} is the intrinsic equilibrium constant related to the chemical reaction, usually referred to as the intrinsic constant (Dzombak and Morel, 1990), *a* is the thermodynamic activity of aqueous species and the terms in brackets represent the concentrations of surface complexes (as moles per kg of water). It should be noticed that the electrostatic terms are disregarded in this formulation of surface complexation reactions.

Sorption can also be modelled with the K_d model, which assumes that the concentrations of sorbed, s, and dissolved species, c, are related through the distribution coefficient K_d, according to:

$$s = K_d\, c \qquad [\ 2.38\ ]$$

In this case, sorption can be included directly into the transport equation by introducing the retardation coefficient, Re.

2.3.1.10. Carbon steel corrosion

The available oxygen in the HLW disposal cell in granite will be consumed soon after its closure, and anaerobic conditions will prevail in the long term. The canister will be treated as a porous material made of 100% metallic iron, Fe(s), which corrodes according to:

$$Fe(s) + 2H_2O \rightleftarrows Fe^{2+} + 2OH^- + H_2(g) \qquad [\ 2.39\ ]$$

By rewriting this reaction in terms of the primary species used in the numerical model, one obtains:

$$Fe(s) + 2H^+ + 0.5O_2(aq) \rightleftarrows Fe^{2+} + H_2O \qquad [\ 2.40\ ]$$

The carbon-steel corrosion is kinetically controlled. It should be noticed that η = 0 for constant canister corrosion. The corrosion rate, r_c, in μm/year is calculated as:

$$r_c = \frac{r_m M_w}{\rho} \qquad [\ 2.41\ ]$$

where ρ is the density of the carbon steel (7860 kg/m^3), M_w is its molecular weight (55.85 g/mol) and r_m is the Fe(s) dissolution/precipitation rate (mol/m^2/year).

Besides constant carbon-steel corrosion rate other time-varying corrosion rates depending on ambient conditions (T, pH, Eh) will be considered. The dependence of the corrosion rate on temperature was analysed by Samper *et al*. (2016). They considered that carbon-steel canister dissolves according to the kinetic law of Equation [2.1] with an activation energy equal to 11 KJ/mol (Feron *et al*., 2008). A constant corrosion rate of 2 μm/year was used for the reference run. The results of the sensitivity run which accounts for the thermal field and the influence of temperature on corrosion showed that the corrosion rate increases from 2 to 4.75 μm/y and then decreases smoothly. Canister corrosion in the sensitivity run was faster than in the reference run. They also concluded that: (1) The computed concentration of dissolved Fe^{2+} and the pH in the sensitivity run increase initially faster than those of the reference run, (2) The precipitation of corrosion products occurs before, and their migration into the bentonite in the sensitivity run is lower than in the reference run; and (3) The porosity of the bentonite near the canister decreases faster than those computed in the reference run.

Samper *et al*. (2016) mentioned that there is no well-established geochemical model which considers the effect of the ambient chemical conditions (pH, Eh, Fe, …) on the corrosion rate in reactive transport models. They analysed the dependence of the corrosion rate on pH, Eh and the concentration of Fe^{2+} by performing an isothermal sensitivity run similar to the reference run, but accounting for a variable corrosion rate, r_m, which depends on pH, Eh and the concentration of dissolved iron. Model results show that canister corrosion slows down at t = 10^3 years and the canister is fully corroded at t = $8{\cdot}10^5$ years. This reduction of the corrosion rate leads to important changes in the patterns of the concentration of dissolved Fe^{2+}, pH, Eh, sorption and mineral dissolution/precipitation at t = 10^3 years. They also concluded that: (1) Magnetite and siderite precipitation in the sensitivity run is significantly smaller than that of the reference run, (2) The thickness of the zone where these minerals precipitate is significantly larger than that of the reference run, although the cumulative amount of mineral precipitation near the

canister is smaller; and (3) The reduction of the porosity due to mineral dissolution/precipitation affects a thickness of bentonite of about 45 cm.

The following hypotheses and conceptual models will be considered for modeling canister corrosion: 1) The canister is a porous material where corrosion takes place and corrosion products precipitate; 2) The corrosion front penetrates into the canister as the corrosion progresses until the canister is entirely corroded as reported by Lu (2009); and 3) The anaerobic component of the conceptual geochemical model of steel corrosion and Fe diffusion mechanisms of Hadi *et al*. (2019). These authors proposed a conceptual model of Fe diffusion at the steel-bentonite interface where diffusion of Fe^{2+} occurs only when anaerobic corrosion starts occurring once O_2 is depleted at the surface of the steel and sufficient water saturation conditions are met. Diffusion then proceeds in two stages. During the first stage, Fe^{2+} diffusion inside the bentonite competes with O_2 diffusion toward the interface and Fe is accumulated as Fe^{3+} oxi-hydroxides (mainly goethite) near the interface. Fe^{2+} diffuses into the bentonite once O_2 is depleted in the bentonite.

2.3.2. List of parameters

This section includes the list of the key hydrodynamic, thermal and geochemical parameters. The hydrodynamic and transport parameters of the bentonite and granite include porosity, intrinsic permeability and effective diffusion coefficients. The thermal parameters include specific heat and the thermal conductivity of the solids.

The reactive transport model requires the following geochemical parameters:

1) The mineralogical composition of the bentonite and the granite.
2) The cation exchange reactions, CEC, cation selectivity coefficients and concentrations of exchanged cations of the bentonite.
3) The types and concentrations of sorption sites and their protolysis constants of the bentonite.
4) The equilibrium constants for aqueous complexes.
5) The solubility constants for mineral phases in the bentonite and the granite.
6) The kinetic parameters (rate constants, specific surfaces, catalytics terms, …) of the kinetically controlled mineral dissolution/precipitation reactions.
7) Canister corrosion rate and its dependence on pH.

Parameter values used in the reference calculation are listed in Section 2.4.

2.3.3. Initial and boundary conditions

This section includes the initial and the boundary conditions of the water flow and the solute and heat transport. The chemical composition of the initial and boundary porewaters are also included.

2.3.3.1. Solute transport

The solution of the transient solute transport equation requires knowing:

1) Transport parameters which include: the porosity and the diffusion coefficient.
2) Sinks and sources: w, C* and R.
3) Initial conditions: $C_0(x,y)$ at $t = t_0$.
4) Boundary conditions.

The initial condition c_0 is either prescribed or may correspond to the solution of a steady-state transport problem such as:

$$\nabla\cdot\left(\theta\mathbf{D}\nabla c_0\right)-\mathbf{q}\nabla c_0+w_0\left(c_0^*-c_0\right)+\theta R_0=0 \qquad [\ 2.42\ ]$$

The following boundary conditions will be used:

1) Dirichlet condition, according to which the concentration along the boundary Γ_1 is given by:

$$c\big|_{\Gamma_1} = \tilde{c} \qquad [\ 2.43\ ]$$

where $\tilde{c}$ is a prescribed concentration, which may vary in space and time.

2) Neumann condition, according to which the diffusive flux normal to the boundary Γ_2 is prescribed and equal to F'$_D$:

$$-\theta \mathbf{D} \nabla c \cdot \mathbf{n}\big|_{\Gamma_2} = F_D' \qquad [\ 2.44\ ]$$

where n is the unit vector normal to the boundary.

3) Cauchy mixed condition, according to which the total solute flux normal to the boundary $\Gamma 3$ is prescribed and equal to F_0:

$$\left(-\theta \mathbf{D} \nabla c + \mathbf{q} c\right) \cdot \mathbf{n}\big|_{\Gamma_3} = F_0 \qquad [\ 2.45\ ]$$

In outflow boundaries F_0 will be taken equal to the advective flux c**q**·**n**.

2.3.3.2. Heat transport

A Dirichlet condition (prescribed temperature) will be used for the inner and the outer boundaries.

2.4. Parameter values

This section presents the values of the key chemical, thermal and hydrodynamic parameters considered in the reactive transport model of the HLW disposal cell in granite.

2.4.1. Flow and transport parameters

The FEBEX bentonite is considered saturated with a thickness of 75 cm. The hydraulic conductivity of the bentonite is extremely low, with a value of $6 \cdot 10^{-14}$ m/s (Samper *et al*., 2016). Therefore, solute advection is negligible and diffusion is the main solute transport mechanism. All the water is assumed to be accessible to solutes.

The bentonite porosity, ϕ, is equal to 0.407. The effective diffusion coefficient, D_e, of the bentonite is equal to $4.07 \cdot 10^{-11}$ m^2/s (Samper *et al*., 2016). The solid density of the bentonite is 2700 kg/m^3. The specific heat capacity and the saturated thermal conductivity of the bentonite are equal to 846.4 J/kgºC and 1.15 W/mºC, respectively (Samper *et al*., 2016).

The porosity of the SRG granite is equal to 0.005 (Samper et al., 2008). Its hydraulic conductivity is equal to $8.72 \cdot 10^{-12}$ m/s (Samper et al., 2008). The effective diffusion coefficient, D_e, of the granite is equal to $5.02 \cdot 10^{-14}$ m^2/s (Samper *et al*., 2008). The thermal and hydrodynamic parameters of the bentonite and granite considered in the reactive transport model of a HLW disposal cell in granite are listed in Table 2.2 (Samper *et al*., 2016, 2018).

Table 2.2. Thermal and hydrodynamic parameters of the bentonite and granite (Zheng and Samper 2008; Zheng et al., 2011, based on ENRESA 2006, Samper et al., 2016, 2018).

Parameter	Bentonite	Granite
Hydraulic conductivity (m/s)	$6\ 10^{-14}$	$8.72 \cdot 10^{-12}$
Liquid viscosity (kg/m s)	$7 \cdot 10^{-5}(T-44)^{-1.562}$	$661.2 \cdot 10^{-3}(T-44)^{-1.562}$
Solid density (kg/m^3)	2700	$2700e^{(-2 \cdot 10^{-6}(T-12))}$
Solid specific heat (J/kg ºC)	846.4	1029
Solid thermal conductivity (W/m ºC)	1.23	1.5

2.4.2. Chemical parameters

The chemical composition of the initial bentonite porewater (Samper *et al*., 2016) is listed in Table 2.3. The main mineral component of the bentonite is the smectite. The initial accessory mineral volume fractions considered in the bentonite are: calcite (1%), quartz (1%) and gypsum (0.08%). The cation exchange capacity (CEC) of the bentonite is 102 meq/100 g (Fernandez *et al*., 2004). Cation selectivity coefficients for exchanged Ca^{2+}, Mg^{2+}, K^{+} and Fe^{+} were derived from Samper *et al.* (2008) and Tournassat (2003). Surface complexation reactions in the bentonite are modelled with the triple sorption site model of Bradbury and Baeyens (1997, 2005). The total concentration of sorption sites is 0.322 mol/L. The first type of sorption sites corresponds with the strong sites which have a large binding affinity but a small concentration (0.0079 mol/L). The other two types are the weak #1 and #2 sites which have binding constants weaker than those of the strong sites although their concentrations (0.16 mol/L) are larger than those of the strong sites.

Table 2.4 shows the protolysis constants for surface complexation reactions for a triple-site sorption model and the selectivity constants for cation exchange reactions in the FEBEX bentonite.

Table 2.3. Chemical composition of the initial FEBEX bentonite porewater (Samper et al., 2016).

Species (mol/L)	**FEBEX bentonite porewater**
pH	6.46
Eh (V)	-0.078
Ca^{2+}	$3.32 \cdot 10^{-2}$
Mg^{2+}	$3.67 \cdot 10^{-2}$
Na^{+}	$1.88 \cdot 10^{-1}$
K^{+}	$1.55 \cdot 10^{-3}$
Fe^{2+}	$1.43 \cdot 10^{-4}$
Al^{3+}	$1.0 \cdot 10^{-8}$
Cl^{-}	$2.75 \cdot 10^{-1}$
HCO_3^{-}	$7.59 \cdot 10^{-3}$
SO_4^{2-}	$2.05 \cdot 10^{-2}$
SiO_2 (aq)	$9.67 \cdot 10^{-5}$

Table 2.4. Protolysis constants for surface complexation reactions for a triple-site sorption model (Bradbury and Bayens, 2005); and the selectivity constants for cation exchange reactions in the FEBEX bentonite (ENRESA, 2006).

Cation exchange		**$K_{Na\text{-}cation}$**
	$Na^+ + X\text{-}K \Leftrightarrow K^+ + X\text{-}Na$	0.138
	$Na^+ + 0.5\ X_2\text{-}Ca \Leftrightarrow 0.5\ Ca^{2+} + X\text{-}Na$	0.2924
	$Na^+ + 0.5\ X_2\text{-}Mg \Leftrightarrow 0.5\ Mg^{2+} + X\text{-}Na$	0.2881
	$Na^+ + 0.5\ X_2\text{-}Fe \Leftrightarrow 0.5\ Fe^{2+} + X\text{-}Na$	0.5
Surface complexation		**Log K_{25}**
$S^SOH_2^+$	$\equiv S^SOH_2^+ \Leftrightarrow \equiv S^SOH + H^+$	-4.5
S^SO^-	$\equiv S^SO^- + H^+ \Leftrightarrow \equiv S^SOH$	7.9
S^SOFe^+	$\equiv S^SOFe^+ \Leftrightarrow \equiv S^SOH + Fe^{2+} - H^+$	0.6
S^SOFeOH	$\equiv S^SOFeOH \Leftrightarrow \equiv S^SOH + Fe^{2+} - 2H^+ + H_2O$	10.0
$S^SOFe(OH)_2^-$	$\equiv S^SOFe(OH)_2^- \Leftrightarrow \equiv S^SOH + Fe^{2+} - 3H^+ + 2H_2O$	20.0
$S^{w1}OH_2^+$	$\equiv S^{W1}OH_2^+ \Leftrightarrow \equiv S^{W1}OH + H^+$	-4.5
$S^{w1}O^-$	$\equiv S^{W1}O^- + H^+ \Leftrightarrow \equiv S^{W1}OH$	7.9
$S^{w1}OFe^+$	$\equiv S^{W1}OFe^+ \Leftrightarrow \equiv S^{W1}OH + Fe^{2+} - H^+$	3.3
$S^{w2}OH_2^+$	$\equiv S^{W2}OH_2^+ \Leftrightarrow \equiv S^{W2}OH + H^+$	-6.0
$S^{w2}O^-$	$\equiv S^{W2}O^- + H^+ \Leftrightarrow \equiv S^{W2}OH$	+10.5

The chemical composition of the granite boundary water (Samper *et al*., 2016) is listed in Table 2.5. A simple set of minerals will be initially considered in the granite. The initial mineral volume fractions will be the following: calcite (5%) and chalcedony (20%). Besides this mineral assemblage other accessory mineral phases could be considered in the granite. Additional data will be derived from the data collected in several uranium mines in Spain by Gómez *et al*. (2006). They reported geological, hydrogeological and hydrochemical studies of two uranium mines in fractured media in Spain: El Berrocal site (Toledo) and Los Ratones Mine (Caceres).

Table 2.5. Chemical composition of the granite boundary water (Samper et al., 2016).

Species (mol/L)	Granite boundary water
pH	7.825
Eh (V)	-0.188
Ca^{2+}	$1.522 \cdot 10^{-4}$
Mg^{2+}	$1.604 \cdot 10^{-4}$
Na^+	$4.350 \cdot 10^{-3}$
K^+	$5.371 \cdot 10^{-5}$
Fe^{2+}	$1.791 \cdot 10^{-8}$
Al^{3+}	$1.85 \cdot 10^{-8}$
Cl^-	$3.949 \cdot 10^{-4}$
HCO_3^-	$5.049 \cdot 10^{-3}$
SO_4^{2-}	$1.561 \cdot 10^{-5}$
SiO_2 (aq)	$3.761 \cdot 10^{-4}$

2.4.3. Parameters for the sensitivity cases

This section presents the parameters required for the proposed sensitivity cases of the reactive transport model of the geochemical evolution in a HLW disposal cell in granite. These cases are listed in Table 2.1.

Sensitivity Case 1 will consider the vitrified waste from the Belgian reference SM539. The vitrified waste will be considered as an equivalent porous medium accessible only to water. Similar to the base case with the French reference SON-68 vitrified waste, a simple glass dissolution model such as GRAAL or GLASSOL derived from ACED Task 3 will be used to simulate the Belgian reference SM539 alteration in the numerical models at the scale of the disposal cell of ACED Task 4. The chemical parameters for the vitrified waste will be provided by ACED Task 3.

Sensitivity Case 2 will address the scenario of a breached canister with corrosion products and remaining uncorroded metallic iron. The corroded layers will be treated as fully-saturated equivalent porous medium. The corrosion products will be derived from model results.

Compacted MX-80 bentonite (instead of FEBEX betonite) with a thickness of 35 cm will be considered in the Sensitivity Case 3. The compacted MX-80 bentonite mainly consists of a low charge montmorillonite with Na^+ and Ca^{2+} as interlayer cations. The porosity of the MX-80 bentonite is equal to 0.39 for an initial dry density of 1.6 g/cm^3. The porewater composition of compacted MX-80 bentonite will be taken from Bradbury and Baeyens (2003) who provided a geochemical model for the chemical composition as a function of dry density and by taking into account montmorillonite swelling, the semi-permeable membrane effects, different types of water (interlayer, double layer and free water), the highly effective buffering characteristics of exchangeable cations and the amphoteric edge sites. The former buffer the cation concentrations and the latter fix the pH in the porewater of a resaturated bentonite at a value of 8. Bradbury and Baeyens (2003) assumed that the free water is the accessible porosity for chloride. This assumption will be considered in the Sensitivity Case 3. The chemical composition of the MX-80 bentonite porewater at pH = 8 and for a dry density of 1600 kg/m^3 is listed in Table 2.6 .The calculated porewater is a NaCl/Na_2SO_4 type water with a relatively high ionic strength (I = 0.327 M).

Montmorillonite is the main mineral component of the MX-80 bentonite. Its content ranges from 65 to 75%. The initial accessory mineral volume fractions of the MX-80 bentonite include (Pusch, 2001): Quartz (10-14%), feldspars (5-9%), mica and chlorite (2-4%), carbonates and chlorite (3-5%). The cation exchange capacity (CEC) of the MX-80 bentonite is 78.7 meq/100 g (Bradbury and Baeyens, 2002). Cation selectivity coefficients for exchanged Ca^{2+}, Mg^{2+} and K^+ have been taken from Bradbury and Baeyens (2002). The cation occupancies and the selectivity coefficients for cation exchange reactions in the MX-80 bentonite are listed in Table 2.7. Surface complexation reactions in the MX-80 bentonite are modelled with the triple sorption site model of Bradbury and Baeyens (1997, 2005). The total concentrations of sorption sites and the protolysis constants for the surface complexation reactions are similar to those adopted for the Base Case in the FEBEX bentonite (

Table 2.4)**Erreur ! Source du renvoi introuvable.**.

Table 2.6. Calculated chemical composition of the MX-80 bentonite porewater at pH = 8 and at initial dry density of 1600 kg/m³ (Bradbury and Baeyens, 2003).

Species (mol/L)	MX-80 bentonite porewater
pH	6.46
Eh (V)	-0.078
Ca^{2+}	$1.01 \cdot 10^{-2}$
Mg^{2+}	$7.69 \cdot 10^{-3}$
Na^{+}	$2.61 \cdot 10^{-1}$
K^{+}	$1.32 \cdot 10^{-3}$
Cl^{-}	$1.08 \cdot 10^{-1}$
HCO_3^{-}	$7.80 \cdot 10^{-4}$
SO_4^{2-}	$9.45 \cdot 10^{-2}$

Table 2.7. Cation occupancies and selectivity coefficients for cation exchange reactions in the MX-80 bentonite (Bradbury and Baeyens, 2002; 2003).

Exchangeable cations	Cation occupancies (meq/kg)
Na^{+}	$K_{NA/K}668 \pm 40$
K^{+}	13 ± 2
Ca^{2+}	66 ± 3
Mg^{2+}	40 ± 3
Cation exchange reactions	**Selectivity coefficients**
Na-montmorillonite + $K^{+} \Leftrightarrow$ K-montmorillonite + Na^{+}	4.0 ± 1.6
2 Na-montmorillonite + $Mg^{+2} \Leftrightarrow$ Mg-montmorillonite + 2 Na^{+}	2.2 ± 1.1
2 Na-montmorillonite + $Ca^{+2} \Leftrightarrow$ Ca-montmorillonite + 2 Na^{+}	2.6 ± 1.2

The Sensitivity Case 4 will consider a highly-conductive fracture zone normal to the gallery and an excavation damaged zone (EDZ). The permeability and porosity of the facture zone will be taken from data published by Martínez-Landa *et al*. (2016) from the Mina Ratones site in Southwestern Spain. The thickness of the EDZ will be taken from 1 to 1.5 m based on the results of Kwon *et al*. (2009). The porosity will be assumed equal to twice the porosity of the intact rock. The permeability and the effective diffusion of the EDZ will be calculated from those of the intact rock by using the Kozeny-Karman equation for permeability and Archies law for the effective diffusion.

The Sensitivity Case 5 will consider a SRG porewater with a chloride concentration greater than the value used in the base case. A plausible range of chloride concentrations will be selected based on data from Gómez *et al*. (2006).

The Sensitivity Case 6 will consider the conditions of the Czech Reference Crystalline rock. The required parameters (rock porewater chemical composition, mineral composition, hydraulic conductivity and porosity) will be derived from Červinka *et al*. (2018). They presented the results of a study focused on the geochemical evolution of a DGR in the potential Kraví hora (Bukov Underground Research Facility, URF Bukov) site. The Czech Reference Crystalline rock has a porosity of 0.05 and a hydraulic conductivity of $5.0 \cdot 10^{-9}$ m/s. (Červinka *et al*., 2018). The chemical composition of two types of synthetic rock porewaters, SGW2 and SGW3, is listed in Table 2.8 (Červinka *et al*., 2018). The SGW2 chemical

composition was derived from the average physico-chemical parameters and average chemical composition of real groundwater at the URF Bukov about 600 m below the surface. Its composition corresponds to the groundwater in deeper circulation in the fracture environment of the crystalline rocks of the Bohemian Massif, type Ca-HCO_3. The SGW3 chemical composition was derived from the physico-chemical parameters and chemical analysis of groundwater at the Rožná mine from the 22-24 level about 1000 m below the surface. The groundwater composition represents a very slow circulation of deep groundwater in the fracture environment of the crystalline rocks of the Bohemian Massif, type Na-HCO_3.

Červinka *et al*. (2018) estimated the mineral composition in the following three rock types: 1) Compact fine-grained amphibolite with biotite; 2) Migratised amphibolic gneiss with biotite; and 3) Stromatitic biotite migmatite with amphibole. Amphibole, plagioclase, quartz and biotite are the main minerals. The accessory minerals include pyrite, pyrhotine, chalcopyrite, zircon, monazite, apatite and titanite and secondary minerals include apatite, titanite, sericite, chlorite, K-feldspar and calcite. Other parameters of the Czech Reference Crystalline rock will be derived from the EURAD Deliverable 2.4 (Neeft *et al*., 2019).

Table 2.8. Chemical composition of the SGW2 and SGW3 Czech *crystalline rock porewaters (Červinka et al., 2018).*

Species (mol/L)	SGW2	SGW3
pH	8.2	9.4
Eh (V)	0.237	0.237
T (ºC)	25	25
Ca^{2+}	$8.64 \cdot 10^{-4}$	$3.24 \cdot 10^{-5}$
Mg^{2+}	$3.42 \cdot 10^{-4}$	$4.12 \cdot 10^{-6}$
Na^{+}	$8.65 \cdot 10^{-4}$	$3.81 \cdot 10^{-3}$
K^{+}	$5.37 \cdot 10^{-5}$	$1.79 \cdot 10^{-5}$
Fe^{2+}	$1.79 \cdot 10^{-6}$	$1.79 \cdot 10^{-6}$
Al^{3+}	$3.71 \cdot 10^{-6}$	$3.71 \cdot 10^{-6}$
Cl^{-}	$9.31 \cdot 10^{-5}$	$5.28 \cdot 10^{-4}$
HCO_3^{-}	$2.77 \cdot 10^{-3}$	$2.68 \cdot 10^{-3}$
SO_4^{2-}	$2.19 \cdot 10^{-4}$	$1.09 \cdot 10^{-4}$
SiO_2 (aq)	$5.20 \cdot 10^{-4}$	$4.18 \cdot 10^{-4}$

2.5. Expected outcomes

The proposed outcomes of the reactive transport model of the HLW disposal cell in granite will be focused on the time evolution at selected locations and interfaces and the spatial distribution at selected times of:

1) The computed pH and redox.
2) The computed concentrations of the dissolved chemical species, including Na, K, Ca, Mg, Cl, HCO_3^{-}, SO_4^{-2}, Si, Fe and Al.
3) The computed concentrations of mineral phases such as Fe(s), ISG, calcite, gypsum, quartz, magnetite, siderite, goethite, greenalite, cronstedtite, montmorillonite, nontronite and saponite.
4) The computed volume fractions of the mineral phases such as Fe(s), ISG, calcite, gypsum, quartz, magnetite, siderite, goethite, greenalite, cronstedtite, montmorillonite, nontronite and saponite.

5) The computed concentrations of exchanged cations (Na, K, Ca, Mg, Fe) and and surface complexes.
6) The computed changes in porosity.
7) The lifetime or durability of the bentonite buffer and the carbon steel overpack (time at which the overpack will fail).

The list of expected outcomes provided in this deliverable for the HLW disposal cell in granite will be updated at later stages of the project.

The results of the detailed reactive transport models developed in Subtask 4.1 will be used for constructing abstracted models in Subtask 4.2

2.6. Computer codes

This section presents a short description of the two reactive transport codes to be used for modelling the HLW disposal cell in granite. These codes are: CORE^{2D} V5 (Fernández, 2017) and INVERSE-FADES-CORE V2 (Mon, 2017).

CORE^{2D} V5 (Fernández, 2017) is a code for transient saturated and unsaturated water flow, heat transport and multicomponent reactive solute transport under both local chemical equilibrium and kinetic conditions in heterogeneous and anisotropic media. The flow and transport equations are solved with Galerkin finite elements and an Euler scheme for time discretization. The solute transport equation accounts for advection, molecular diffusion and mechanical dispersion. The chemical formulation is based on the ion association theory and uses an extended version of the Debye-Hückel equation (B-dot) for the activity coefficients of aqueous species. The following chemical reactions are considered: aqueous complexation, acid-base, redox, mineral dissolution/precipitation, cation exchange, surface complexation and gas dissolution/ex-solution. CORE^{2D} V5 relies on the thermodynamic database ThermoChimie v10.a (Giffaut et al, 2014). The code also allows the use of other thermodynamic databases. CORE^{2D} V5 is based on the sequential iteration approach to solve for chemical reactive solute transport. Iterations are repeated until some prescribed convergence criteria are attained (Samper *et al*., 2009). The Gaines-Thomas convention is used for cation exchange. Surface complexation is modelled by using three types of protonation/deprotonation sites, S^{S}-OH, S^{W1}-OH and S^{W2}-OH, as proposed by Bradbury and Baeyens (1997). CORE^{2D} V5 takes into account the changes in porosity due to mineral dissolution/precipitation reactions and their feedback effect on the flow and transport parameters under isothermal and non-isothermal conditions (Fernández, 2017). This version also was updated to use available public-domain post-processing tools.

INVERSE-FADES-CORE V2 (Mon, 2017) is a finite element code for modelling non-isothermal multiphase flow, heat transport and multicomponent reactive solute transport under both chemical equilibrium and kinetic conditions in deformable media. The code takes into account the mass balance of water, air, solid and enthalpy; the transport of solids and the mechanical equilibrium. The solute transport equation accounts for advection, molecular diffusion and mechanical dispersion. INVERSE-FADES-CORE V2 solves both forward and inverse multiphase flow and multicomponent reactive transport problems in 1-, 2- and 3-D axisymmetric porous and fractured media. The state variables of the forward model include the liquid and the gas pressures and temperature, which are solved with a Newton-Raphson method. INVERSE-FADES-CORE V2 also relies on the thermodynamic database ThermoChimie v10.a (Giffaut et al, 2014). The inverse problem is solved by minimizing a generalized least-squares criterion with a Gauss-Newton-Levenberg-Marquardt method (Dai and Samper, 2004). The forward routines of INVERSE-FADES-CORE have been widely verified with analytical solutions and other reactive transport codes. Mon (2017) implemented reactive gas transport in INVERSE-FADES-CORE V2 by including additional mass balance equations for the reactive gaseous species in the gaseous phase. INVERSE-FADES-CORE V2 has been benchmarked with other codes for benchmarking problems such as: 1) The chemical interactions of the concrete liner with the compacted bentonite of the engineered barrier and the clay host rock; and 2) The carbonation of concrete in unsaturated conditions during the operational period of a repository.

2.7. Summary

The conceptual, mathematical and numerical models of the HLW disposal cell in granite have been presented. The reactive transport model of the geochemical evolution of a HLW disposal cell in granite involves the following interfaces: bentonite/granite host rock, bentonite/carbon-steel and carbon-steel canister/vitrified waste. A reference case and several sensitivity cases have been proposed. The reference case starts when the 75 cm thick FEBEX bentonite buffer is saturated. Partial desaturation is not considered to be a relevant scenario for the bentonite in the HLW disposal cell in granite. Hydrogen generation due to corrosion is not expected to produce a partial desaturation of the bentonite barrier. The model is non-isothermal and accounts for the thermal transient decrease of temperature until the thermal pulse will dissipate. The excavation damaged zone is disregarded in the base case. Its relevance will be evaluated in a sensitivity case by considering that the permeability, porosity and effective diffusion of the EDZ are larger than those of the intact Spanish Reference granitic rock. Anaerobic corrosion of the canister will be uniform and consume water and generate H_2. The main geochemical processes in the transient phase include: 1) The precipitation of iron corrosion products at the canister/bentonite interface, 2) The destabilization of montmorillonite, 3) The replacement of bentonite minerals by Fe-rich smectites and non-swelling Fe-rich phyllosilicates; and 4) The cementation of bentonite due to the precipitation of iron corrosion products and SiO_2 coming from montmorillonite transformation. Canister corrosion will lead to an increase in the concentration of dissolved Fe^{2+} and a decrease of Eh. The precipitation of the corrosion products at the canister will decrease the porosity of the bentonite and lead to pore clogging near the canister.

The model of the reference case (Base Case) and the sensitivity cases of the HLW disposal cell in granite will consider three successive periods. The first one (period I) will cover the oxic transient stage. Period II starts when the bentonite barrier is fully saturated and the anoxic conditions are prevailing. Canister corrosion, the interactions of corrosion products and the bentonite and the interactions of bentonite and granite will be considered in this period. Finally, period III will start after canister failure and will consider glass alteration and the interactions of glass with corrosion products and uncorroded iron. It is important to point out that only periods II and III will be considered in the model. This approach is consistent with that used for the HLW disposal cell in clay (*Figure* 3.4). A simple glass dissolution model derived from Task 3 will be used for the numerical model at the scale of the disposal cell and consider the French reference SON-68 vitrified waste. The interactions of the glass and the corrosion products will start in period III after canister failure. The following sensitivity cases are proposed: 1) The Belgian reference glass SM539; 2) An early breached canister with corrosion products and remaining uncorroded metallic iron; 3) A MX-80 bentonite buffer 35 cm thick; 4) EDZ and fracture zones in the granitic rock; 5) A change in the chloride concentration of the SGR porewater; and 6) The Czech Reference Crystalline rock. A more detailed explanation of the sensitivity cases is shown in Table 2.1. All the runs (base and sensitivity cases) are non-isothermal. The model disregards the partial desaturation of the bentonite barrier.

3. Conceptual, mathematical and numerical models, and numerical tools of the HLW disposal cell in clay

3.1. Description of the disposal cell concept

3.1.1. The generic configuration of the HLW cell

The disposal cells for vitrified high-level waste (HLW) treat the chemical evolution from the waste form until the host rock. The present contribution focuses on the characteristics of disposal cells embedded in an argillaceous sedimentary formation based on the Belgium, Dutch and French national programs as schematically shown in Figure 3.1 (Andra, 2016a; Weetjens *et al*., 2012; Neeft *et al*., 2019).

The first two programs share the same concept of the so-called supercontainer as well as rather poorly indurated clay formations (for more details on the HLW disposal cells in these programs, see chapters 4 and 9 in Neeft *et al.*, 2019). The supercontainer diameter is about 2 m, and consists of a carbon steel overpack containing the HLW, which is itself inserted in prefabricated cylindrical concrete buffer material. The concrete is made from ordinary Portland Cement (OPC or CEM I type) and limestone aggregates. The pH has to be kept at high values during the thermal phase, and much longer beyond, in order to keep the carbon steel overpack passivated, limit corrosion and ultimately radionuclide release. The French concept (Andra, 2016a, see also chapter 8 in Neeft *et al*., 2019) significantly differs from the supercontainer concept by considering a 25 mm thick liner (sleeve) made of low-carbon steel in an indurated clay formation. The annular gap between the liner and the host rock is filled with a bentonite/cement grout that imposes corrosion-limiting environmental condition during the thermal phase only. The injection of the cement-bentonite grout is considered to counter the acidic pH transient (pH ~ 4.5) resulting from the host rock oxidation which may lead to high corrosion rates. The grout also passivates metallic surfaces and prevent any possible diffusion of O_2 from the gallery to the steel during the operation phase. The alkalinity of the grout should have been neutralized readily afterwards to prevent the dissolution of the vitrified waste (also simply named nuclear glass) under high pH values. A common point between the two types of concepts is that the steel overpack encapsulates the waste canisters that contain the vitrified waste (Andra, 2016a; Deissmann *et al*., 2016).

The rather large discrepancies in the supercontainer and sleeve/liner concepts do not facilitate the development of a common definition of a representative HLW disposal cell in a clay host rock. Therefore, it has been decided to start from a generic configuration of the HLW disposal cell in a clay host rock as a base case and to perform variants that will fulfil more explicitly one feature of the Belgian/Dutch concept or one feature of the French concept but in an integrated manner.

Figure 3.1 shows the initial state of the generic configuration of the HLW disposal cell in a clay host rock:

- The vitrified waste/nuclear glass (40 cm in diameter) is explicitly considered in reactive transport modelling (not as boundary conditions) for coupling with the barriers and host-rock evolutions.
- The overpack (5 cm thick) consists of low alloy carbon-steel.
- The cement-base buffer (30 cm thick in *Figure* 3.1, and then from 5 cm to 100 cm thick, see Section 3.1.2) is composed of Portland cement and calcareous aggregate without any reinforcement by steel structures.
- The clay host rock (several meter thick in the calculations) is the French Callovo-Oxfordian claystone.

Several elements of the usual concepts for HLW are not taken into account:

- The stainless-steel envelope (0.5 cm thick) is not included due to the strong uncertainty on the (pitting) corrosion mechanism and its small thickness.
- The carbon steel liner in which the waste packages are inserted is not simulated, the focus being put on the steel overpack protecting the nuclear glass from dissolution.

- The technological gap is not simulated explicitly in Subtask 4.1 but as filled by corrosion products in the period II of alteration defined in Section 3.2.
- The configuration does not consider any explicit EDZ within the argillaceous host rock, i.e. a full self-healing of the fissures in the EDZ is assumed in the base case scenario.

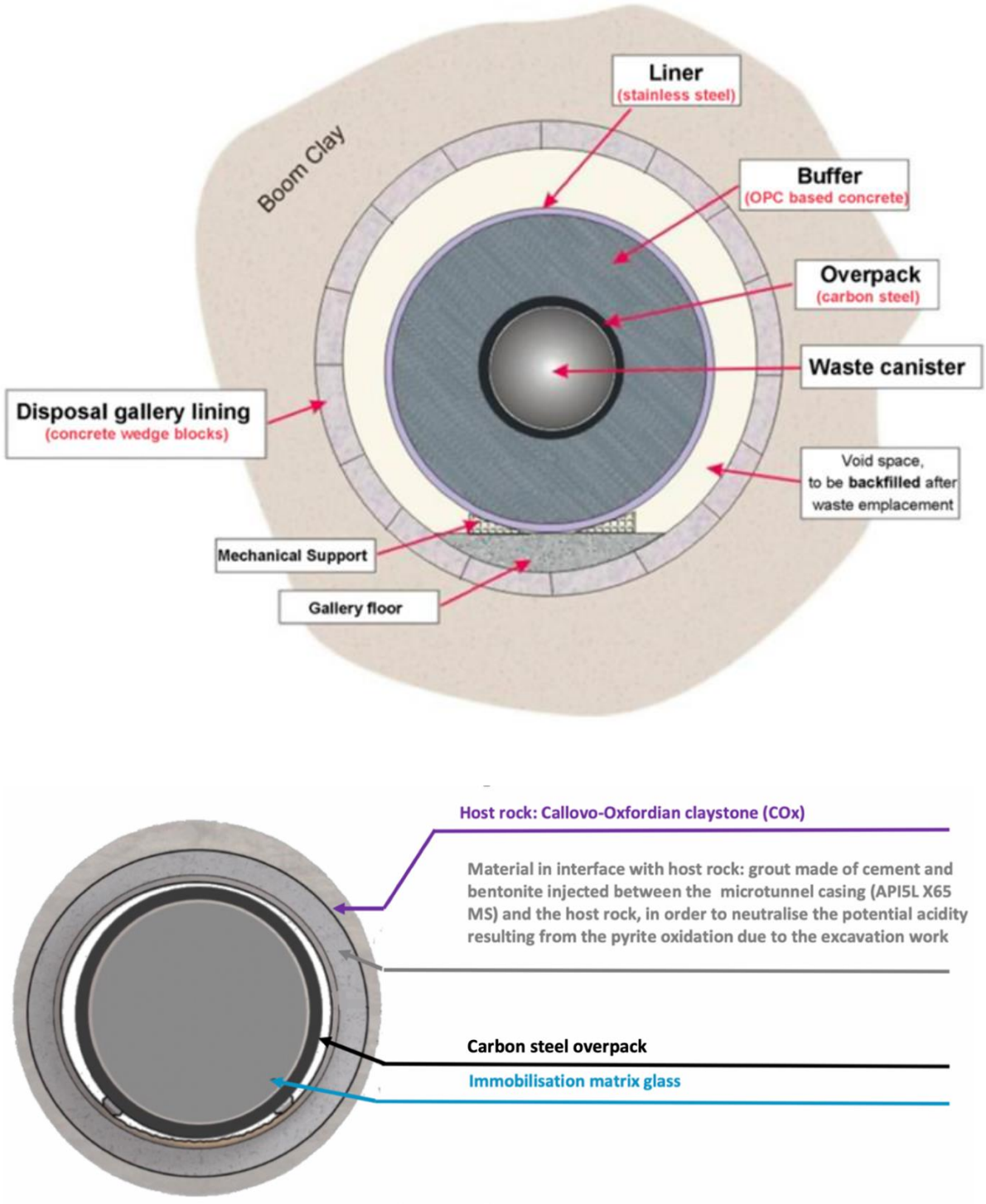

Figure 3.1. Cross-section of the HLW disposal cell in a clay host rock for the Belgian/Dutch supercontainer concept (top, Craeye et al. 2009; Neeft et al., 2019) and the French sleeve/liner concept (bottom, Andra, 2016a; Neeft et al., 2019).

3.1.2. Variation on the cement buffer size or composition

The generic concept of Figure 3.2 roughly corresponds to an intermediate state between the two European concepts developed for vitrified waste disposals in an argillaceous formation. As shown in Figure 3.3, a variant will extend the cement buffer thickness up to 75 cm (Belgian/Dutch concept based on the supercontainer design) and 100 cm (maximum of the sensitivity analysis). Inversely, reducing the buffer thickness to 5 cm leads to a configuration similar to the French concept with a liner protected against corrosion by the cementitious buffer. The objective is to provide Subtasks 4.2 and 4.3 with a set of reference cases to study questions such as the effect of the cement-buffer thickness on the duration of the steel overpack.

Two chemical compositions of the cement-base buffer are considered for the smallest thickness (Figure 3.3): either a bentonite/cement grout buffer (low-pH cement) more relevant for the French concept, or an ordinary Portland cement (OPC/CEM I) for the sake of comparison.

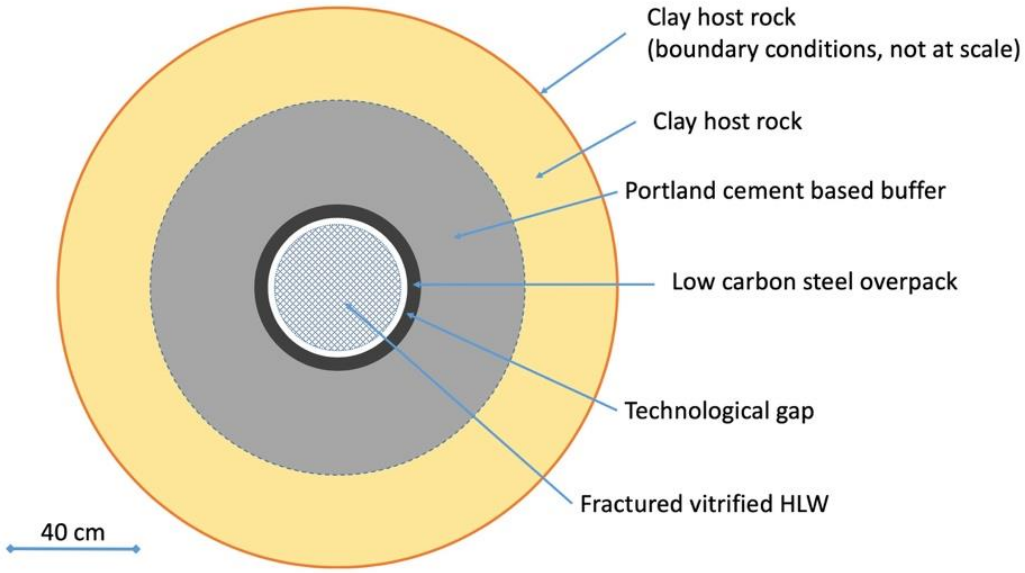

Figure 3.2. Initial geometry of the generic configuration of the HLW disposal cell in a clay host rock.

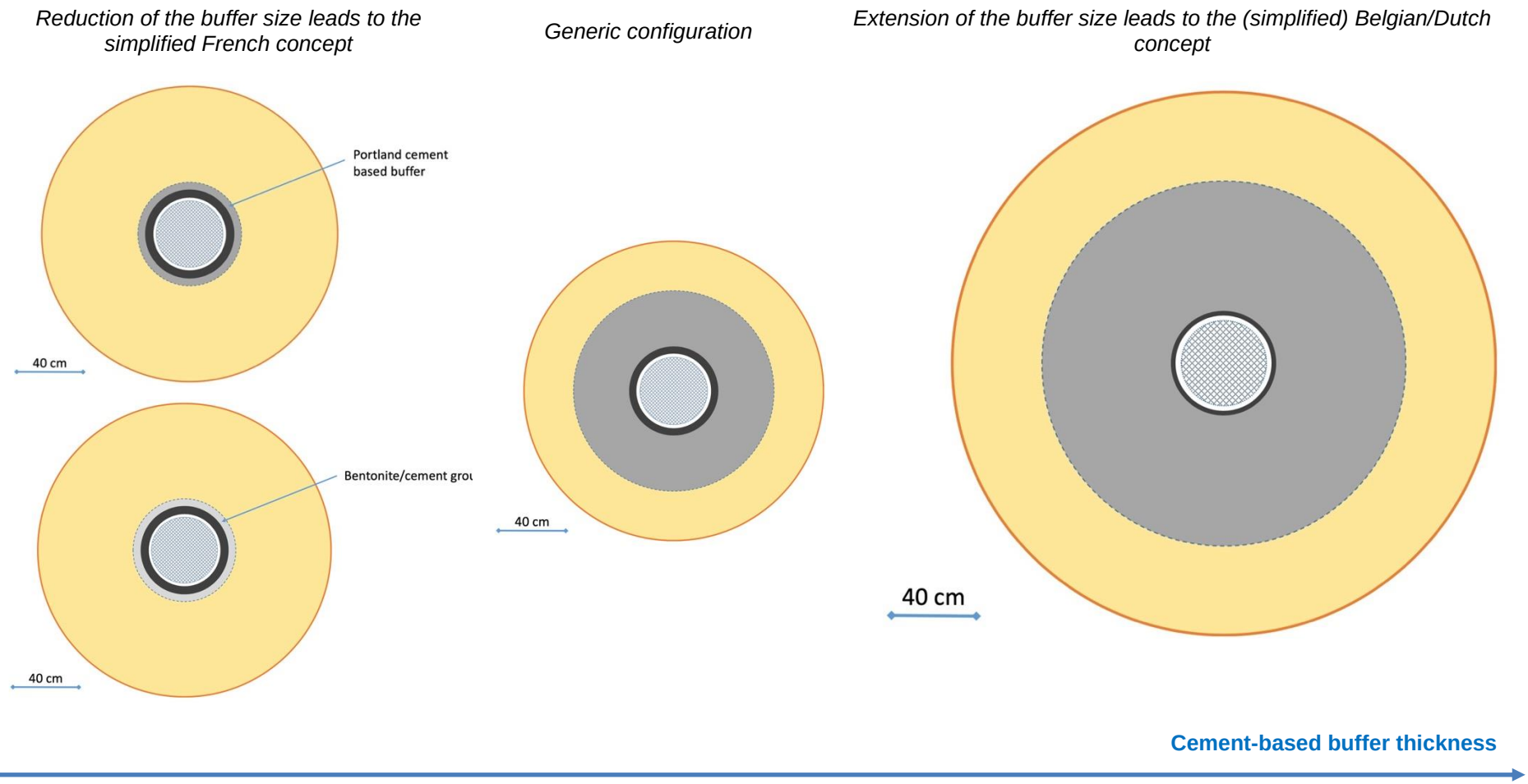

Figure 3.3. Variants in terms of buffer thickness of generic HLW disposal cell towards the French liner concept or the Belgian/Dutch super container concept; another variant of the liner concept considers a low-pH cement/bentonite grout instead of the CEM I based buffer.

3.2. Conceptual model and narrative evolution

3.2.1. Chemical alterations before the breaching of the steel overpack

Subtask 4.1 addresses a very long duration (up to 10^5 years). *Figure* 3.4 schematically represents the successive periods that occur during the lifetime of the repository (e.g. Weetjens *et al*., 2012; Andra, 2016b). Period II is the first reference case investigated in the present modelling. The initial state does not consider any effect of the oxic transient period I. That is to say the starting point considers pristine materials only. This preliminary step concerns the subsystem steel/cement/clay. The nuclear glass is not explicitly included yet since it is expected that no significant corrosion of steel and, therefore, of glass takes place as long as the high-pH buffer is there.

The decrease in temperature in the cell from 80°C to 25°C is relatively fast compared to the direct disposal of spent fuel. The thermal stage of a vitrified waste depends on the waste type and the cooling period before disposal. The temperature at the steel overpack decreases to 40 °C in less than 200 years for most nuclear glasses and in 1000 years for the warmest wastes (Neeft *et al*., 2019). Afterwards, the temperature continues to decrease to the natural background temperature but more slowly. A simplified thermal transient stage will be considered over 1000 years, to reach then a stationary temperature of 25 °C in period II. The transient stage will be based on the temperature decrease at the steel/cement interface from 65 °C to 25 °C calculated for the supercontainer concept after a storage period of 130 years for CSD-v (Figure 12.5 of Neeft et al., 2019). The temperature gradient across the cement liner and the COx clay will be calculated by HYTEC and iCP using the thermal parameters of the Table of 12-2 in consistency with the result of the Figure 12-5, both from Neeft et al. (2019). Temperature may affect the mineralogy of the concrete. For instance, ettringite will be destabilized around 55 °C and will reprecipitate once temperature will decrease possibly leading to an internal mechanical stress.

The objective of the modelling of the base case of the period II (case II – A, see Table 3.1*)* is to mainly assess the coupled lifetimes of the cement-based buffer and of the steel overpack, as a function of the cement buffer thickness or composition. That is to say that a main objective of the calculations for period II before the perforation of the overpack is to define the near field at the time of the overpack perforation, with regards to the mineralogy, geochemistry, porosity, diffusion coefficients, etc. of the different components.

Assuming fully water-saturated conditions, the chemical interactions between the clay environment and Portland cement will progressively alter the buffer (De Windt et al., 2004; Neeft et al., 2019; Deissmann et al., 2021): from a hyperalkaline fresh state (pH > 13), to a depletion in portlandite (pH ≈ 12), and the subsequent decalcification of the calcium silica hydrate phases C-S-H (10.5 < pH < 12), up to eventually to very low Ca/Si ratio or even alumino-silicagel. Carbonation is permanently active, especially at the interface due to the partial pressure of carbon dioxide higher in the clay rock formation. It may ultimately lead to pH $\leq$ 10. Additional amounts of ettringite may precipitate at the expense of monocarboaluminate, for instance, in case of diffusion of sulphates from the clay host rock. Magnesium silicate hydrates (M-S-H) will form at the interface between low-pH cement and clay rocks (e.g., Dauzères et al., 2016). The chemical interaction between the concrete and the clay rock will lead to the dissolution of the primary phases of cement and rock, and the subsequent precipitation of new mineral phases mainly close to the interface. Further, the mineral alteration will be weaker but the hydrochemistry and cation exchange properties of the rock will be impacted by the attenuated alkaline plume. For example, fast exchange of Ca^{2+} with K^+ from the cementitious material could lead to a decrease of swelling pressure into the clay materials (more relevant for bentonite than clayey rocks).

The degradation progresses as degradation fronts from the cement/clay interface towards the steel overpack. At high pH, the steel is passivated by the deposition of a thin layer of magnetite corresponding to very small corrosion rates. Such beneficial alkaline conditions have been calculated to last for several tens of thousands of years in the Belgian concept. It is generally assumed that the passivation of the steel becomes inactive when the alkaline pH decreases below 10.5. The modelling of steel corrosion will be a function of pH (but not of temperature as detailed below). Steel is modelled during this period

as a non-porous media. In most of the present modelled cases, the computed hydrogen generation by corrosion has no effect on the water saturation degree. The cement/iron interaction should not lead to any significant consumption of iron by CEM I but it may be different in the case of the bentonite/cement grout. Those two points will be further investigated in Task 2.

The ageing of cement, cement/clay interactions, or less likely expansive corrosion products of steel, may generate a few transversal cracks or a transversal network of interconnected cracks within the cement buffer (e.g. Craeye *et al*., 2009; Perko *et al*., 2015; Seetharam and Jacques, 2015), as schematically shown in *Figure* 3.6. In that case diffusive mass transfers are enhanced and may accelerate the degradation of the buffer (case II-B).

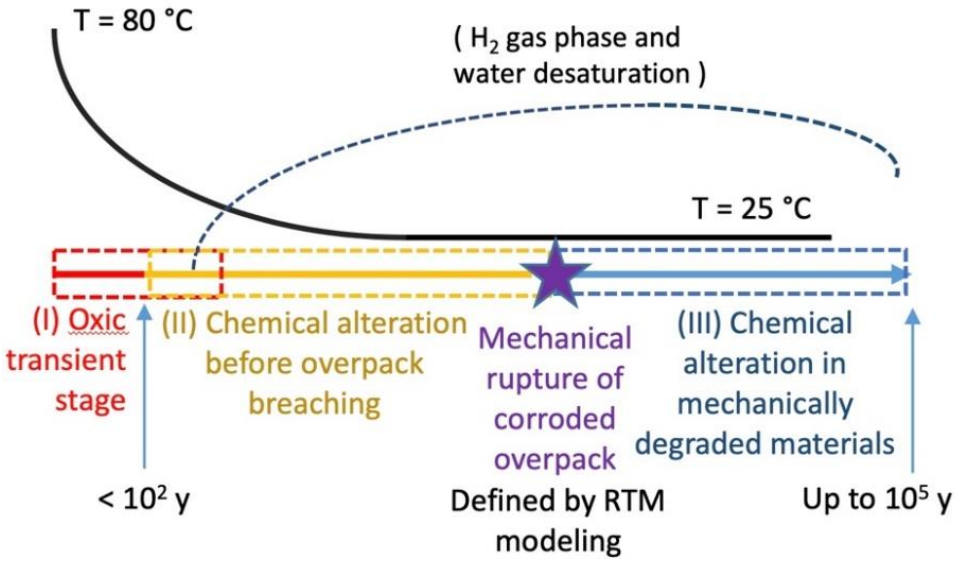

Figure 3.4. Successive periods considered in reactive transport modelling (RTM) and evolution of temperature in the disposal cell; the effect of hydrogen production on water saturation is not taken into account in most cases. Only, periods II and III are considered in the present reactive transport modelling. The safety function of the cement buffer with respect to the steel overpack breaching significantly differs between the Belgian/Dutch and the French disposal concepts (see Section 3.1.1).

Table 3.1. Base case and optional scenarios of the reactive transport modelling of the chemical evolution of the HLW cell.

Period (see *Figure* 3.4)	Buffer thickness	Temperature	Water saturation	Concrete type	Steel canister	Nuclear glass
Base cases						
II - A	5, 30, 75, 100 cm	Transient stage over 1000 y, then 25 °C	100 %	CEM I + calcareous aggregates, non damaged	Non porous	No
III - A	100 cm	25 °C	100 %	Chemically altered CEM I + calcareous aggregates, fractured	Porous, partly filled with corrosion products	Yes
Options						
II - B	30, 100 cm	Transient stage over 1000 y, from 65°C to 25°C	100 %	CEM I + calcareous aggregates, fractured	Non porous	No
II - C	5 cm	Transient stage over 1000 y, from 65°C to 25°C	100 %	Cement/bentonite grout	Non porous	No
II - D	100 cm	Transient stage over 1000 y, from 65°C to 25°C	Partially desaturated (70 – 80 %) for cement and a fraction of the rock	Chemically altered CEM I + calcareous aggregates, fractured	Non porous	No

The effect of the cement thickness cannot be separated from the evolution of the porosity and transport properties of the materials around the cement/clay interface. It is foreseen to start with a base case where the porosity will not be a critical parameter. Porosity evolution with time (period II) can be considered in the sensitivity analyses. The possible clogging of the pores in the clayey host rock (e.g. by calcite precipitation) close to the interface with cement has to be considered simultaneously to the evolution of cement buffer in Task 4 as an optional case. The decreasing porosity would slow down very much the further alteration of the cement and could keep the pH high for a long time, thus prolonging the overpack lifetime. On the contrary, porosity opening in the altered cement will speed up the chemical interactions and, eventually the corrosion of the carbon steel overpack.

In parallel to case II – B, the calculations in case II - C replace the CEM-I buffer by a bentonite/cement grout buffer (of lower pH). This configuration is the closest to the French concept in terms of thickness and material composition.

Glass alteration is only considered in the case III after the breaching of the canister. The cement buffer is then in advanced state of chemical degradation which composition and pH will have been modelled in the period II case. It is worth noting that an early breaching of the overpack (due to design defect or mechanical stress, not chemical corrosion) is not investigated in the present narrative scenario. An early breaching (e.g. < 5000 y) would allow the migration of a strong alkaline plume from the unaltered

concrete buffer. This would be a more penalizing case since glass leaching is enhanced under high pH conditions (Fournier *et al*., 2019). Eventually, it is worth noting that the fully water saturation assumption is conservative to some extent since the corrosion mechanisms of glass are slowed down under partially water saturated conditions.

In all cases, diffusion is the only transport processes. Advection is never considered.

3.2.2. Chemical alterations after the breaching of the steel overpack

The simulations of the periods II and III can be decoupled or joined into a single full reactive transport model depending of the numerical capabilities of the code.

The period III as depicted in Figure 3.4 considers a breached canister with corrosion products and remaining uncorroded metallic iron over the spatial extension originally covered by the technological gap and the non-corroded overpack (as shown in Figure 3.5). The corroded layers can be considered as equivalent porous media, under fully water-saturated conditions. The corrosion products will be chosen by the modellers (e.g. magnetite, Fe(II)-carbonate as chukanovite/siderite, Fe(II)-silicate as cronstedtite, greenalite…). The exact nature of the corrosion products will be up-dated thanks to the detailed calculations of Subtask 3.2.

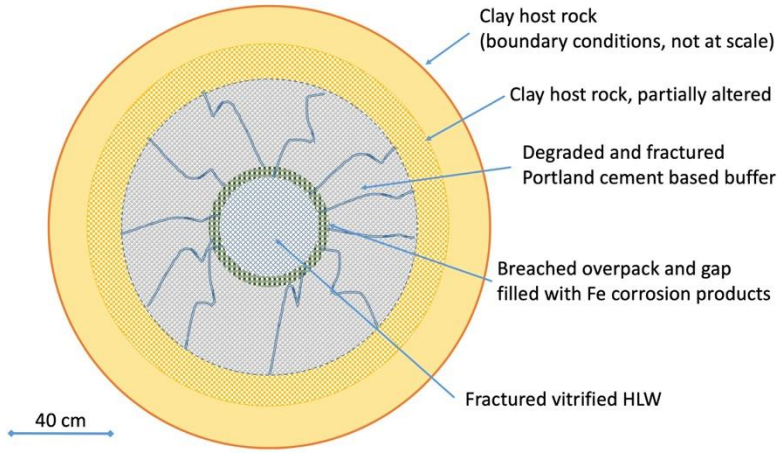

Figure 3.5. Altered evolution of the HLW disposal cell in a clay host rock due to the chemical interactions between the materials.

The beginning of period III will be defined by the present ACED results on the durability of the overpack calculated in period II by assuming a mechanical breaching when the non-corroded thickness is 1.5 cm (maybe 1 cm). The calculated duration will be compared to the durations defined independently from ACED in performance assessment scenarios of WMO or TSO depending on the thickness of the overpack and its corrosion rate (e.g. 4000 years for the French disposal concept and a general corrosion process). The arbitrary mechanical rupture of the overpack leading to a high-pH plume in contact with glass is not studied in Subtask 4.1 but in Subtask 3.2.

Temperature is fixed to 25°C in period III. The nature and spatial extension of the alteration of the cement and clay host rock at the time of the mechanical rupture come from the calculations of period II. The diffusive properties of the cement-based buffer correspond to a fractured/cracked state as in case II-B.

It is likely that the hydrogen gas generated by steel corrosion (*Figure 3.4*) will not be fully evacuated to the host rock in the French concept. The “drying” effect of hydrogen is not assessed in Subtask 4.1. However, a constant water saturation degree between 70 – 80 % in the materials is assumed in case III-B. It decreases the effective diffusion coefficient and the corrosion rates of steel but may alter the cement buffer by carbonation. The feasibility of a simplified multiphase reactive transport modelling will

be evaluated in this optional case with diffusion of CO_2 gas, and maybe H_2 gas, in the system (numerical feasibility, available resources). CO_2(g) diffusion accounts for cement carbonation (Seigneur *et al*., 2020) and its effect on the durability of the alkaline pH buffering capacity of the concrete buffer.

The fractured vitrified waste is modelled as an equivalent porous medium with a cracking factor to set the reactive surface. The dissolution of the virified waste (i.e. nuclear glass) in water can be modelled by a rate law with a simple activity term on the dissolved silica a_{Si} given in *Figure 3.6*. This rate law is developed in the dataset section. It is somehow an 'abstracted' model that can be calibrated (e.g. in a lookup table) with more complex models as the GRAAL model (Frugier *et al*., 2008) in Task 3. The dissolution of glass is then explicitly coupled with the barriers and host-rock influences through the control of the dissolved silica by the modelling of sorption onto the corrosion products on the one hand, and by the modelling of the precipitation of secondary silicate phases containing Fe^{2+} (e.g. greenalite), Mg^{2+} (e.g. Mg-phyllosilicate) or Ca^{2+} (e.g. C-S-H of low Ca/Si ratio) on the other hand. It is worth noting that silica sorption on magnetite has almost no effect on glass durability for duration relevant of HLW disposals (De Windt *et al*., 2006). The best selection of these phases could be results from Task 3. The remaining iron corrosion products and iron-rich phyllosilicates will probably be less reactive towards the glass than the uncorroded iron. One assumes that a small amount of uncorroded iron is still available to react with the glass after canister failure.

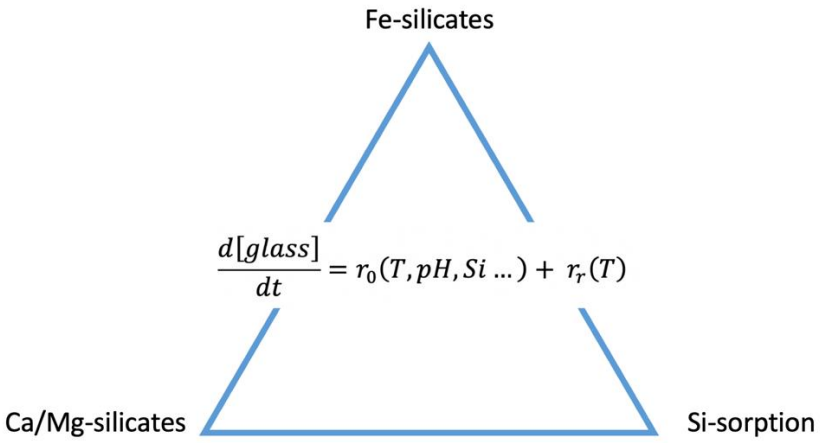

Figure 3.6. Simplified rate law taking into account the coupling of glass dissolution with the chemical evolution of silica concentration, pH and temperature used in the reactive transport modelling. The rate law will be adjusted with respect to the results of Task 3 and is detailed in the Section 3.3.2*.*

To conclude, the conceptual model described in this section is able to couple different types of chemical processes for the entire multibarrier systems of the HLW disposal cell in clay host rock. It goes a step further than the previous modelling of subsystems such as cement/clay interface within the CEBAMA project (Duro *et al*., 2020). Four key parameters are used for the sensitivity analysis of the chemical evolution of the HLW cell, in particular to assess the durability of the steel overpack, which is tightly linked to the lifetime of the cement buffer, and the dissolution rate of the nuclear glass. These parameters are the thickness of the cement-based buffer, the type of cement or grout, the breaching/fracturing of the materials, and the degree of water saturation (Figure 3.7).

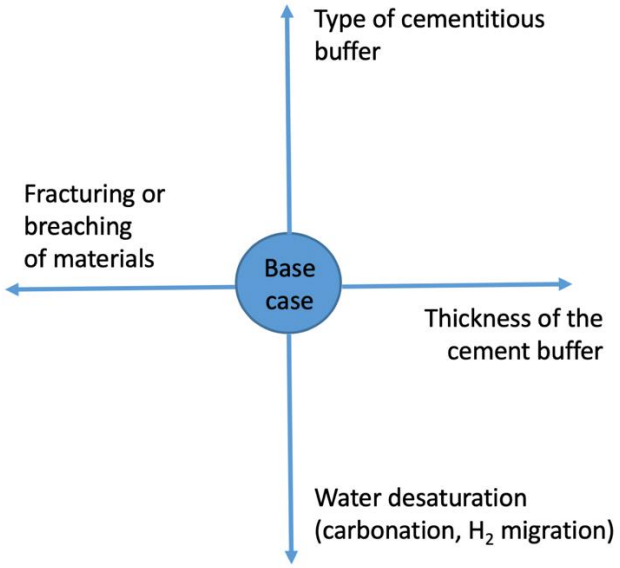

Figure 3.7. The four key parameters used for the sensitivity analysis of the reactive transport modelling of the HLW cell, in particular for the durability of steel overpack and dissolution of the nuclear glass.

3.3. Mathematical model

This section gives an overview of the mathematical laws for the chemical and physical processes required to simulate the evolution as described in the narrative conceptual model.

3.3.1. Equations

3.3.1.1. Chemical processes: thermodynamic equilibrium

The chemical equilibrium state of complex aqueous systems, including minerals, organics, colloids and gases for processes as aqueous speciation, precipitation/dissolution of solid phases, and sorption (surface complexation with electrostatic correction, ion exchange). The aqueous chemistry includes acid/base reactions, oxidation and reduction (redox) processes and aqueous complexation by inorganic ligands.

The thermodynamic equilibrium state of the chemical system is calculated according to the usual mass action equation:

$$n_A A + n_B B \leftrightarrow n_C C + n_D D \qquad [\ 3.1\ ]$$

$$K_i(T) = \frac{(C)^{n_C}(D)^{n_D}}{(A)^{n_A}(B)^{n_B}} = exp\left(\frac{-\Delta G^0}{RT}\right) \qquad [\ 3.2\ ]$$

where n_i is the stoichiometric coefficient, (A) is the activity of the species A, K is the thermodynamic equilibrium constant, ΔG_0 is the change in Gibbs free energy of the reaction, R is the gas constant and T is the absolute temperature [K].

The activity is calculated as the product of the concentration and the activity coefficient. Several mathematical relations have been developed for aqueous solutions of increasing ionic strengths I. At low to moderate ionic strength ($I \leq 0.5$ mol/kg), the empirical formula of the truncated Davies model derived from the Debye-Huckel model of activity corrections of dissolved ions is generally used. The B-dot model and specific ion theory (SIT) are used to calculate activity corrections at higher ionic strengths.

3.3.1.2. Chemical processes: kinetics

The explicit modelling of kinetic control is required in key reaction such as iron corrosion or the dissolution of clay minerals. The rate of dissolution or precipitation of a mineral M_i can be modelled by the following rate law:

$$\frac{d[M_i]}{dt} = k_i A_{v,i} \prod_i (E)^{p_i} \prod_i (E_i E)^{p_i} \left(\left(\frac{Q_i}{K_i^{-1}} \right)^m - 1 \right)^n \qquad [\ 3.3\ ]$$

The variation of the mineral concentration is proportional to the intrinsic kinetic constant of the reaction, k_i [mol m^{-2} s^{-1}] and to the mineral surface area per unit volume, A_v [m^2/L]. The term $\left(\left(\frac{Q_i}{K_i^{-1}} \right)^m - 1 \right)^n$ is dependent on the deviation from thermodynamic equilibrium and related to the concept of the saturation index (Q_i stands for the ion activity product, the HYTEC code considers K_i that is the thermodynamic formation constant that is the inverse of the solubility product K_s). Precipitation (supersaturation state) takes place if $Q > K_s$, otherwise dissolution (undersaturation state). The term m and n are empirical exponents. The product term Π_i describes the dependence of the reaction rate with respect to the chemistry of solution. The species act as catalysts if the exponent is positive, or as inhibitors if the exponent is negative. The term (E_i) is the activity (or concentration) of a dissolved species (e.g. the hydroxyl ion OH$^-$) and p_i is a power-constant, mechanistically-based or fitted to experimental data.

A summation of several kinetic laws analogous to Eq. 3-3 is frequent for the same mineral, typically to take into account specific pH-dependencies for acidic, neutral or alkaline conditions, as well as redox-dependency with specific laws under oxic and reducing conditions.

The accelerating effect of temperature on abiotic kinetics can be formulated as an Arrhenius law, according to the following equation:

$$log\ k_i(T_2) = log\ k_i(T_1) - \frac{E_A}{2.3R}\left(\frac{1}{T_2} - \frac{1}{T_1}\right) \qquad [\ 3.4\ ]$$

where E_a is the activation energy [kJ/mol] and T the temperature [K].

3.3.1.3. Chemical processes: ion exchange and surface complexation

Cation exchange by a solid exchanger (montmorillonite, zeolite, etc.) is a key process in clayey materials. Ions in the interlayer space or channels of the crystal structure can be exchanged for other ions from the solution keeping electroneutrality. For instance, Na^+ substitution by Ca^{2+} cations present in solution writes as

$$2\ \overline{Na} + Ca^{2+} \rightarrow \overline{Ca} + 2\ Na^+ \qquad [\ 3.5\ ]$$

where the upper bar stands for a cation bound to the solid. The distribution of the cations between the solution and the exchanger may be given by a relation derived from the law of mass action and the Gaines-Thomas (GT) formalism:

$$K_{GT}(\overline{Na}/\overline{Ca}) = \frac{f_{\overline{Ca}}\,(Na^+)^2}{f_{\overline{Na}}{}^2\,(Ca^{2+})} \qquad [\ 3.6\ ]$$

assuming that the activity of the exchangeable cations can be modelled by an equivalent fraction

$$f_{\overline{Ca}} = \frac{[\overline{Ca}]}{\sum_i [\overline{C_i}]} = \frac{[\overline{Ca}]}{CEC} \qquad [\ 3.7\ ]$$

where the bracket stands for the exchangeable cation concentration, usually given as meq/100g of exchanger, and CEC (cation exchange capacity) is the sum of all the exchangeable cation concentrations.

Surface complexation is a second type of sorption mechanisms. The (ad)sorption processes of elements from the solution occur at the surface of a given solid (magnetite, montmorillonite…). That is to say true complexation reaction at interface between the solution and hydroxyl sites S-OH present at the solid surface, such as for instance

$$S - OH + M^{2+} \rightarrow S - OM^{+} + H^{+} \qquad [\ 3.8\ ]$$

as well as acid–base reactions, for instance

$$S - OH \rightarrow S - O^{-} + H^{+} \qquad [\ 3.9\ ]$$

The latter, for example, can be modelled as a mass action law,

$$K = \frac{(S - OH)}{(S - O^{-})\,(H^{+})} \qquad [\ 3.10\ ]$$

considering an additional electrostatic term through the double layer model or not.

3.3.1.4. Reactive diffusion under water saturated conditions

The general formulation of the multicomponent reactive transport equation under water saturated conditions considering only diffusion is

$$\frac{\partial \omega \mathrm{C_i}}{\partial \mathrm{t}} = \nabla.(\mathrm{D_e} \nabla \mathrm{C_i}) - \frac{\partial \omega \overline{\mathrm{C_i}}}{\partial \mathrm{t}} \qquad [\ 3.11\ ]$$

where C_i and $\overline{C_i}$ are respectively the mobile and immobile concentrations of an element *i* per unit volume of solution [mol/L], ω is the porosity of the material. The term $-\frac{\partial \omega\, \overline{C_i}}{\partial t}$ is the source/sink term that is driven by chemical reactions, whereas the other terms represent transport processes. The term D_e [m²/s] is the effective diffusion coefficient ($D_e = \omega D_p$ where D_p is the pore diffusion coefficient).

The diffusion coefficient can evolve when mineral precipitation or dissolution changes the local porosity. Actually, the porosity is subjected to change in time and space due to geochemical processes such as dissolution or precipitation (opening and clogging of the pore space). The change in porosity can be calculated from the evolution of the mineral concentrations in the system, knowing their molal volume or density. The empirical Archie's Law is easy to implement in reactive transport models and applicable to a wide range of materials:

$$\mathrm{D_e} = \mathrm{D_e}(\omega_0) \left(\frac{\omega - \omega_c}{\omega_0 - \omega_c} \right)^{m} \qquad [\ 3.12\ ]$$

where ω_0 is the initial porosity, ω_c is a critical porosity threshold under which diffusion stops and *m* is an empirical Archie's coefficient.

3.3.1.5. Reactive diffusion of gases under partially water saturated conditions

A simplified two-phase dynamics of mass transfer under unsaturated water conditions can be simulated assuming a reactive transport model in the water phase linked to diffusion in the gas phase (De Windt *et al.*, 2014; Sin *et al.*, 2019).

The reactive transport equation for the aqueous phase writes as:

$$\frac{\partial(\theta^{w}C_{i})}{\partial t} = \nabla.(D_{e}^{w}(\theta^{w})\,\nabla C_{i}) - \frac{\partial\theta^{w}\overline{C_{i}}}{\partial t} \qquad [\ 3.13\ ]$$

where θ^w is the volumetric content of the water phase, the righthand side partial derivative is the source/sink term and the diffusion coefficient D_e^w is itself a function of the water content according to the relation

$$D_{e}^{w}(\theta^{w}) = \frac{\theta^{w}}{\theta_{T}}\,D_{e,sat}^{w} = S^{w}\,D_{e,sat}^{w} \qquad [\ 3.14\ ]$$

where θ_T is the total porosity of the porous media (identical to ω at water fully saturated conditions), S^w is the water saturation degree and $D_{e,sat}^w$ is the effective diffusion coefficients [m²/s] at water fully saturated conditions. Millington-Quirk relation can also be applied.

The reactive transport equation for the gaseous phase writes as

$$\frac{\partial(\theta^{g}C_{j})}{\partial t} = \nabla.(D_{e}^{g}(\theta^{g})\,\nabla C_{j}) + Q_{j}^{g} \qquad [\ 3.15\ ]$$

where θ^g is the volumetric content of the gas phase, C_j is the concentration of a gas species *j* regarding the gas phase volume [mol/L], D_e^g is the effective diffusion coefficient in the gas phase common to all gas molecules [m²/s] and Q_j^g is linked to the variation of the partial pressure of the gas species *j* [mol/L/s] driven by the dissolution of the gas in the aqueous phase according to the Henry's Law.

3.3.1.1. Heat conductivity

Heat conduction will dominate over the convective transfer of heat in the disposal cell of HLW in clay due to the very low permeability of the near-field materials. The transient thermal stage can then be calculated as

$$\rho C_{p}\left(\frac{\partial T}{\partial t}\right) = \nabla\cdot(\lambda\nabla T) \qquad [\ 3.16\ ]$$

where ρ is the specific mass of the media, C_p is the specific heat capacity of the media, λ is the thermal conductivity of the media and T is the temperature in K.

3.3.2. List of parameters

A set of hydrodynamic and geochemical parameters is required for the vitrified waste, the carbon steel overpack, the concrete buffer (or cement/bentonite grout) and the clay host rock.

The hydrodynamic and transport parameters include porosity and effective diffusion coefficients (for the water and gas phase).

The reactive transport model requires the following geochemical parameters:

1) The thermodynamic database that contains acid/base reaction, complexation, redox, formation constants of minerals, solubility of gases (Henry's Law), etc. for different temperatures.
2) The cation exchange reactions, CEC, cation selectivity coefficients (clay rock only).
3) The types and concentrations of sorption sites and their surface complexation constants (in the present study for clay rock only).
4) The kinetic parameters (rate constants, specific surfaces, catalytic terms, etc.) of the kinetically controlled mineral dissolution/precipitation reactions.
5) The carbon steel corrosion rate and its dependence on pH, as well as the glass dissolution rate and its dependence on pH and temperature.

3.3.3. Initial and boundary conditions

Fully water saturated conditions (i.e. 100 %, excepted in case III-B with 70 – 80 %) and isothermal conditions are considered as initial physical conditions.

The reactive transport model requires the following geochemical parameters as initial conditions:

1) The initial mineralogy of the concrete and clay rock, the chemical composition for the steel and nuclear glass.
2) The initial pore water chemistry of the concrete and clay rock.
3) The initial contents of exchangeable cations of the clay minerals.

The entire set of physical and geochemical initial parameters are provided in the following section by type of material.

The only boundary condition is the constant concentration type imposed at the outer boundary of the modelled host rock section. The boundary conditions will be fixed sufficiently far away from the interface with the concrete buffer in order to not produce any artefacts.

3.4. Parameter values

3.4.1. Clay host rock

The clay host rock in the representative disposal cell is the French host rock, i.e. the Callovo-Oxfordian (COx) claystone. However, a sensitivity analysis could be done on both bicarbonate concentration (effect on cement carbonation) and chloride concentration (effect on steel corrosion) in comparison with other clay host rocks such as the Boom Clay. All properties given in this section will be used in the reactive transport model (RTM). For the sake of consistency with the literature, the properties are taken from the RTM benchmark (Marty *et al*., 2015) and the RTM of in situ experiments (Debure *et al*., 2019) related to the COx claystone. These two RTM studies selected the Thermoddem database.

The claystone mineralogy is summarized in Table 3.2. Calcite is the predominant carbonate minerals and quartz the predominant silicate. The clayey part is abundant. It is composed of illite and interstratified illite/smectite, but also chlorite. The divalent Ca^{2+} and Mg^{2+} are the main cations of the exchangeable cation population of the host rock. Table 3.3 gives the intrinsic sorption parameters of the clay host rock, i.e. the selectivity constants of cation exchange and the surface complexation properties.

Table 3.2. *Mineralogy, specific surface area and cation exchange population for the initial state of reference of the clay host rock (Marty et al., 2015).*

	Volume fraction(1) [%]	Molar volume(1) [cm³/mol]	As [m²/g]		Exchangeable cation
Carbonate				*% equivalent*	
Calcite	23	37	0.7	Na	19
Dolomite	4	64	0.1	K	4
Siderite(2)	1	29	3	Mg	31
Clay-like phase				Ca	46
Chlorite(Cca-2)	2	222	0.003	CEC	
Illite(IMt-2)	33	139	30	in meq/100g	17.4
Montmorillonite(HcCa)	8	133	8.5	of rock	
Others					
Pyrite(2)	1	24	0.05		
Quartz(alpha)	25	23	0.01 – 0.05		

(1) Thermoddem database. (2) Only for subset RTM where redox modelling is required.

Table 3.3. *Selectivity constants of cationic exchange (Gaines-Thomas formalism, Marty et al., 2015) and surface complexation constants (non-electrostatic model, Marques et al., 2012) of the clay host rock.*

Reaction	Log K_{ex} (25°C)
Cation exchange (whole exchanger)	
$\overline{Na} + K^+ \rightarrow \overline{K} + Na^+$	1.2
$2\,\overline{Na} + Ca^{2+} \rightarrow \overline{Ca} + 2\,Na^+$	0.7
$2\,\overline{Na} + Mg^{2+} \rightarrow \overline{Mg} + 2\,Na^+$	0.7
$2\,\overline{Na} + Fe^{2+} \rightarrow \overline{Fe} + 2\,Na^+$	0.8(1)
Surface complexation (2)	
$S_1\text{-}OH + H^+ \rightarrow S_1\text{-}OH_2^+$	4.5
$S_1\text{-}OH \rightarrow S_1\text{-}O^- + H^+$	-7.9
$S_2\text{-}OH + H^+ \rightarrow S_2\text{-}OH_2^+$	4.5
$S_2\text{-}OH \rightarrow S_2\text{-}O^- + H^+$	-7.9
Site density S_1-OH	1 μmol/m²
S_2-OH	0.05 μmol/m²

(1) LogK (Fe) = logK (Ca) + 0.1 (Idiart & lavina, 2019); (2) Optional for pH buffering, for illite and montmorillonite only.

The hydrochemistry of the pristine COx claystone is detailed in Table 3.4. The water is moderately mineralized. Sodium is the dominant cation, chloride and sulfate are the dominant anions. The partial pressure of CO_2 is about 10^{-2} atm. It can be an important factor when estimating the carbonation of cement. By comparison, the Boom Clay pore water (De Craen *et al*., 2004; Wang *et al*., 2010) is less

concentrated, with a chloride concentration 60 times lower than in COx. The partial pressure of CO_2 is also lower in the Boom clay, about $10^{-2.6}$ atm.

Table 3.4. Porewater chemistry of the clay host rock at 25°C (Marty et al., 2015).

Aqueous species	Total concentration (mol/L)
pH	7.0
K^+	$5 \cdot 10^{-4}$
Na^+	$4.0 \cdot 10^{-2}$
Mg^{2+}	$5.1 \cdot 10^{-3}$
Ca^{2+}	$7.6 \cdot 10^{-3}$
Fe^{2+}	$7 \cdot 10^{-5}$
H_4SiO_4	$2 \cdot 10^{-4}$
HCO_3^-	$3.8 \cdot 10^{-3}$
Cl^-	$4.1 \cdot 10^{-2}$
SO_4^{2-}	$1.1 \cdot 10^{-2}$

The dissolution and precipitation of the minerals constitutive of the clay host rock have to be modelled under kinetics controlled (De Windt *et al*., 2008; Marty *et al*., 2015), according to Equation [3.3], for instance with the parameter sets given in Supplementary Information. As mentioned above, constant concentration boundary conditions (hydrochemistry and mineralogy) are imposed at the limit of the COx host rock.

The porosity ω of the clay host rock is 18 %. A single effective diffusion coefficient D_e of 3×10^{-11} m^2/s will be considered for the initial state of the host rock ($D_e = \omega D_p$ where D_p is the pore diffusion coefficient). For the cases with (constant) partial desaturation, the van Genuchten parameters are provided in Supplementary Information.

3.4.2. CEM I-based concrete (buffer)

The supercontainer concept serves as a reference for the reactive transport modelling of the cementitious buffer. The concrete consists of a fully hydrated CEM I/42.5N HSR LA and limestone aggregates (70 % in volume). The cement content is of 350 g per dm^3 with a water on cement weight ratio (w/c) of 0.47 (Liu *et al*., 2014). Calcareous aggregates are used instead of the usual siliceous aggregates to prevent any long-term alkali reaction between the alkaline pore water and the siliceous aggregates.

The thermodynamic modelling of the CEM I cement is based on the normative phase composition of Lothenbach *et al*. (2008), detailed in Table 3.5. Table 3.6 gives the reference composition calculated for the concrete (GEMS calculation by Kosakowski, 2020). The calculations will be performed with the CEMDATA18.1 database (Lothenbach *et al*., 2019) using the CSHQ solid solution model for the C-S-H (Kulik, 2011). The composition of the hydrated cement is typical of a CEM I cement, with Calcium Silica Hydrate C-S-H of 1.6 Ca/Si ratio, portlandite and ettringite as the main phases. The results are similar to model simulations of Liu *et al*. (2014) using an older CEMDATA database.

Table 3.7 indicates that the initial pore water of the concrete is a K-Na-OH fluid with a pH of 13.35. The actual composition of the mineralogy and hydrochemistry will be slightly different if the modelling is based on the Thermoddem database.

Table 3.5. Normative phase composition of the CEM I (Lothenbach et al., 2008).

Phases	g/100g
Alite	58
Belite	10
Aluminate	7.6
Ferrite	7.5
CaO (free)	0.6
$CaCO_3$	4.8
$CaSO_4$	3.6
K_2SO_4	1.6
Na_2SO_4	0.1
K_2O	0.1
Na_2O	0.05
MgO	1.4
SO_3	0.16
Inert(1)	4.49

(1) Because the normative phase composition does not add up to 100%, some unknown inert material is added with a density equal to quartz.

Table 3.6. Porosity and mineralogical composition of the reference for the CEM I-based concrete at 25°C as calculated with CEMDATA18.1 (Lothenbach et al., 2019) and the CSHQ solid solution model for the C-S-H phases (Kulik, 2011).

	Volume fraction [%]
Aggregates	
Calcite	70
Hydrated cement	
Calcite	0.33
CSHQ	9.45
Ettringite	3.16
Hydrotalcite	0.67
Monocarboaluminate	2.03
C3FS0.84H4.32 (hydrogarnet)	0.80
Portlandite	4.57
Inert material	0.59
Porosity	
Capillary porosity	8.37
Gel porosity	3.17
Total porosity	11.54

Table 3.7. Porewater chemistry of reference for the CEM I-based concrete at 25°C as calculated with CEMDATA18.1 (Lothenbach et al., 2019) and the CSHQ solid solution model for the C-S-H phases (Kulik, 2011).

Aqueous species	Total concentration (molality, mol/kg_{H2O})
pH	13.43
K	3.9×10^{-1}
Na	7.6×10^{-3}
Mg	1.4×10^{-9}
Ca	9.9×10^{-4}
Fe	1.2×10^{-7}
Al	7.8×10^{-5}
Si	7.2×10^{-5}
CO_3^{2-}	1.9×10^{-4}
Cl^-	5.0×10^{-7}
SO_4^{2-}	4.6×10^{-3}

The total porosity of the concrete is 11.54 % with a capillary porosity of 8.37 % and a gel porosity of 3.17 %, as shown in Table 3.6. Low effective diffusion coefficients D_e ($\leq 10^{-12}$ m^2/s) are usually assigned to undamaged cement-based concretes and mortars (e.g. McCarter *et al*., 2000). The ageing of the material under disposal conditions will probably induce networks of cracks and will enhance diffusive transfer (e.g. Craeye *et al*., 2009; Seetharam and Jacques, 2015). The D_e value for the initial state of concrete is about 10^{-11} m^2/s (as Govaerts and Weetjens, 2010), whereas the D_e values will be set in the order of 10^{-10} m^2/s for the fissured state of the concrete.

The dissolution/precipitation of the concrete phases will be modelled at thermodynamic equilibrium, as commonly assumed due to the high reactive surface of the cement phases (e.g. Marty et al., 2015). However, in the scenario of carbonation by CO_2 gas under partially water desaturated conditions (Case III-B), chemical kinetics on portlandite (and C-S-H) dissolution should be introduced in the modelling, or alternatively a diffusion-controlled model with precipitation of a calcite layer around portlandite particles (Liu *et al*., 2014).

3.4.3. Bentonite/cement grout

The actual composition of the bentonite/cement grout that referes to the French disposal concept is not fixed yet, but the nature of the components has been fixed (Michau and Bourbon, 2016). Table 3.8 summarizes the recipe of the bentonite/cement grout before hydration, which is used in Subtask 2.2 of ACED in the BACUCE experiment. The water on cement ratio is much higher than for classical cements, w/c = 2 instead of w/c around 0.5. This bulk composition includes an OPC clinker, blast-furnace slag and gypsum additive (i.e. CEM III cement) on the one hand and addition of silica fume and bentonite on the other hand. They will become partly hydrated once in contact with water. Depending on the experimental results that will be obtained in Subtask 2.2, the bentonite will be considered in the model as a pozzolan during hydration or be directly introduced as a mineral with the cation exchange properties like montmorillonite as presented in Table 3.9 (Bradbury and Baeyens, 2002).

Table 3.8. Recipe of the bentonite/cement grout in Subtask 2.2 of ACED (BACUCE experiment).

Mineral	Composition [kg]
CEM III Rombas (35% clinker + 65% blast-furnace slag)	0.600
Silica fume	0.600
Bentonite	0.160
Hydrotalcite	0.04
Water	2.400

Table 3.9. Cation exchange selectivity constants (Gaines-Thomas formalism, Bradbury and Baeyens, 2002) for the montmorillonite phase in the bentonite/cement grout.

Reaction	$LogK_{ex}$ (25°C)
Cation exchange (whole exchanger)	
$\overline{Na} + K^+ \rightarrow \overline{K} + Na^+$	0.6
$2\,\overline{Na} + Ca^{2+} \rightarrow \overline{Ca} + 2\,Na^+$	0.4
$2\,\overline{Na} + Mg^{2+} \rightarrow \overline{Mg} + 2\,Na^+$	0.3
$2\,\overline{Na} + Fe^{2+} \rightarrow \overline{Fe} + 2\,Na^+$	0.5(1)

(1) LogK (Fe) = logK (Ca) + 0.1 (Idiart & lavina, 2019).

The acquisition of the chemical composition of the grout porewater and the modelling are still in progress in Subtask 2.2. The literature indicates that the hydration of slag and silica fume is relatively slow at 20°C (Lothenbach et al., 2012 & 2014). However, a simple thermodynamic equilibrium modelling with HYTEC assuming a complete hydration has been done in a first approximation to have a first estimate of the mineralogy (Table 3.10). At 20°C the porewater has a pH about 11 and a moderate ionic strength (5×10^{-2} mol/kg). This will be improved while starting the reactive transport calculations of Subtask4.1. The modelling of the evolution of the mineralogy and the porewater chemistry with temperature up to 80°C is also in progress in Subtask 2.2.

Table 3.10. First estimate of the mineralogy for the bentonite/cement grout at 20°C obtained by modelling (Subtask 2.2).

Mineral	Content [wt.%]
C-S-H & C-A-S-H 0.8	60
Ettringite	5
Hydrotalcite	4
Quartz	22
(Montmorillonite	*9)*

The porosity and effective diffusion properties of the grout used in Subtask 2.2 have not be measured yet. One can estimate a porosity about 70 – 80 % and an effective diffusion coefficient D_e in the range of 10^{-10} m^2/s in a first step.

3.4.4. Low carbon steel

The carbon-steel overpack is chemically considered as Fe(0). Metallic iron is never in equilibrium with water and its reactivity is controlled by kinetics. Only the generalized uniform corrosion is considered in this study. Under the present anoxic condition, the kinetic law of Eq. 3-3 can be strongly simplified by only considering the reactive surface area of the overpack and the intrinsic rate constant:

$$\frac{d[Fe(s)]}{dt} = -k_{anox}\ A_v \qquad [\ 3.17\ ]$$

The corrosion rate constant *k* in Equation [3.17] is usually expressed in $mol/m^2/s$ units in geochemical codes but in µm/y in the experimental literature on corrosion. The corrosion rates of low carbon steel under high pH found in the CEM I chemical and anoxic environment are very low (about 0.1 µm/y) due to passivation by the formation of compact magnetite layers at the surface of iron (Yu *et al*., 2012; Kursten *et al*., 2015; Swanton *et al*., 2015; Smart *et al*., 2017). The passivation of the steel may become inactive when the alkaline pH decreases below 10 and the corrosion rate increase by a factor 50 (about 5 µm/y). However, the corrosion rates under moderately alkaline pH (10.5 – 11.5) are not well characterized yet. Only a few studies are available in the literature: first, Bodén and Pettersson (2011); García Calvo *et al*. (2013) on low-pH cements, and more recently Agullo et al. (2015, 2017) on cement/bentonite grouts. In the case of the low pH mortar, García Calvo *et al*. (2013) measured an increase in corrosion rate by one order of magnitude when the pore fluid pH dropped from 13 to below 11.8. According to Deissmann *et al*. (2020), the threshold value is within a wider pH range, i.e. 9 < pH < 11.5. The effect of pH on corrosion can also be assessed by modelling the stability of magnetite versus the change in the local chemical environment around the carbon steel. In the case of the cement/bentonite grout, Agullo and coauthors used Electrochemical Impedance Spectroscopy (EIS) to monitor at the same time the curing process of cement – bentonite mixture and the iron corrosion rate in this mixture. The corrosion rate increased to a few µm/y before gradually dropping to much lower values (Agullo et al., 2017). Eventually, the passivation of iron seemed to occur since the corrosion rate has decreased continuously below to 0.1 µm/y (Agullo et al., 2017), and even to about 1 nm/y under anaerobic conditions (Agullo et al., 2015).

The corrosion rates of

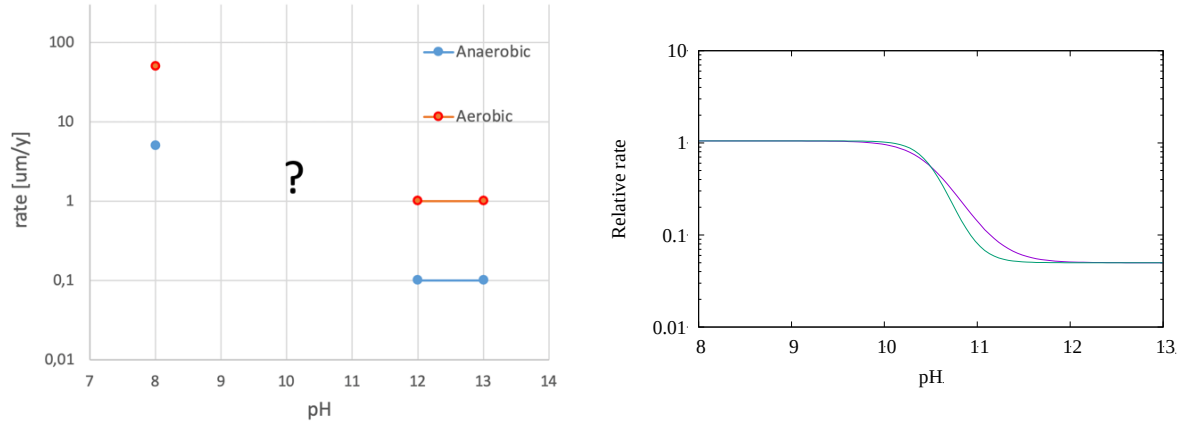

*Figure 3.8*a at pH neutral and high pH correspond to the upper limit of the data range found in the literature for aerobic and anaerobic (Deissmann *et al*., 2020). The anaerobic corrosion rates under moderately alkaline pH (10.5 – 11.5) will be updated by the results of Subtask 2.2 on corrosion in contact

with the chemical of environment of low-pH cement. Meanwhile, it is proposed to use a sigmoidal relationship between the anaerobic corrosion rate and the pH with an inflection point at the threshold pH 10.5 (or pH 11 optionally), as depicted in

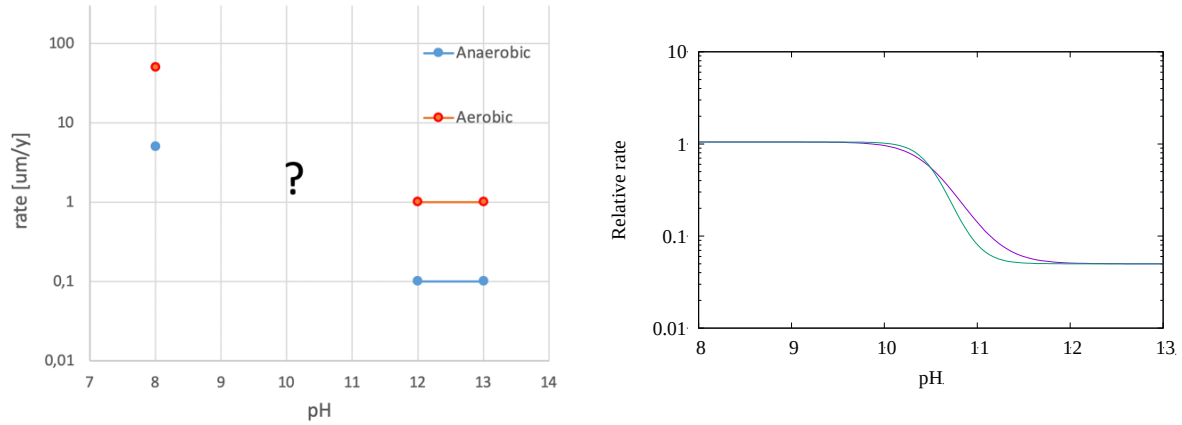

*Figure 3.8*b.

(a) *(b)*

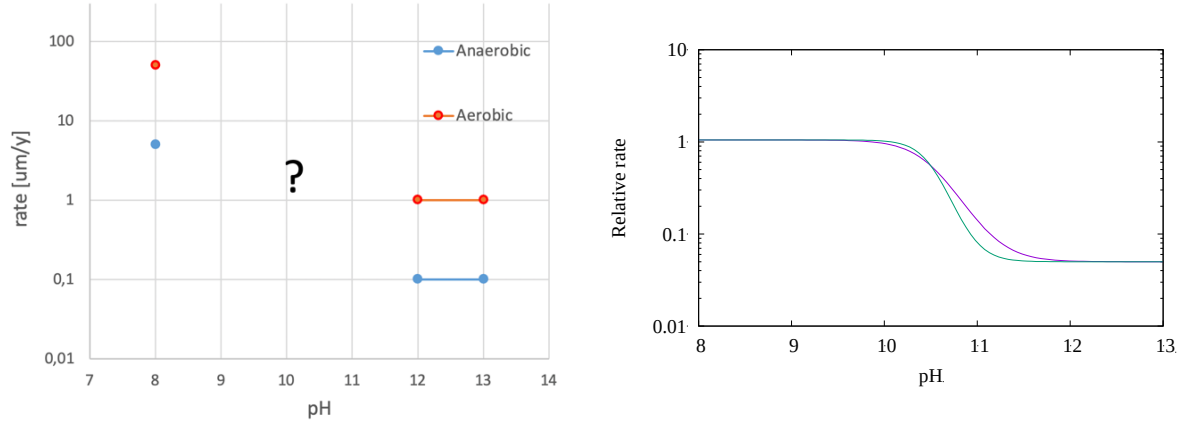

Figure 3.8.(a) *Long-term generalized corrosion rates of carbon steel under anaerobic conditions selected for the reactive transport modelling at 25°C at neutral and high pH values (aerobic rates given for comparison). (b) Relationships that could be used to simulate the evolution from hyper alkaline pH values to more neutral values during the alteration of the cement-based buffer (relative rate = 1 corresponds to the anaerobic corrosion rate at neural pH).*

Under the anoxic/anaerobic conditions assumed in the present modelling *HLW disposal cell in clay host rock*, the most stable corrosion product of metallic iron is magnetite (Fe_3O_4) at high alkaline pH, but iron carbonates such as siderite ($FeCO_3$) or chukanovite ($Fe_2(OH)_2CO_3$) are also likely at slightly alkaline pH values (Odorowski et al., 2017; Saheb et al., 2014). The reactive transport model takes into account magnetite and carbonate iron phases in the base case. Fe(II)-silicates (e.g. greenalite $Fe_3(Si_2O_5)(OH)_4$ or cronstedtite) are also considered in a sensitivity analysis, in particular in the presence of a silica source such as dissolution of nuclear glass. Iron sulphides (e.g. mackinawite) form when corrosion is driven by bacteria activity, but this microbial process is not considered in the present study. The occurrence of these corrosion products will be assessed in more details in Task 3 of ACED.

For the sake of simplicity, the precipitation of the corrosion products will be modelled under thermodynamic equilibrium in a first approach due to the significant uncertainties in the parameters such as surface area and kinetic rate constants (Bildstein *et al*., 2019). But a kinetic control will also be taken into account if it helps to better simulate the corrosion products found in the experimental literature and Tasks 2 and 3 of ACED.

The sorption of silica onto magnetite (Marmier and Fromage, 2000) will be also modelled according to the surface complexation data provided in Table 3.11.

Table 3.11. Constants of surface complexation of silica on magnetite (non-electrostatic model, Marmier and Fromage, 2000).

Reaction	Log K_{ex} (25°C)
$S\text{-}OH + H^+ \rightarrow S\text{-}OH_2^+$	3.5
$S\text{-}OH \rightarrow S\text{-}O^- + H^+$	-9.6
$S\text{-}OH + H_4SiO_4 \rightarrow S\text{-}H_3SiO_4 + H_2O$	4.1
Site density S-OH	3.2 μmol/m^2

It is not obvious to attribute an effective diffusion coefficient D_e to the corroded and breached overpack. A D_e value of 10^{-10} m^2/s is considered in the present calculations, though a less conservative value of 10^{-11} m^2/s (closer to the diffusion within the corrosion product layer) may also be selected for sensitivity analysis. The porosity can be arbitrarily set to 30 %.

3.4.5. Vitrified waste

Modelling the dissolution of the nuclear glass constituting the vitrified waste is probably the most critical aspect for modelling the chemical evolution in a HLW disposal cell in a clay host rock. The GRAAL model (Frugier *et al*., 2008 and 2018) coupled the primary glass alteration rate, controlled by a protective layer's thickness, and the dissolution rate of protective layer in interaction with the environment. The GRAAL model has been implemented under a format compatible with reactive transport models (specifically in HYTEC) and has been applied for modelling glass dissolution in various chemical environments (e.g. Debure *et al*., 2013). Nevertheless, this model seems rather complex for an analysis at the disposal cell scale on the one hand, and the effect of dissolved Fe(II) (from the corrosion products) and kinetic dissolution parameters for temperatures around 40 – 50°C have not been published yet, on the other hand.

Therefore, for the sake of simplicity, the modelling relies on a previous operational HYTEC modelling calibrated for the dissolution of the R7T7 glass (De Windt *et al*., 2006). The implementation of the GRAAL model can still be investigated as an alternative in Task 4 if the simplified approach introduced below does not work. Importantly, Task 3 and/or Subtask 4.2 may also provide for the recalibration of

the kinetic dissolution model or for a look-up table dependent upon parameters such as pH, dissolved silica, dissolved Fe(II) and/or temperature, using the GRALL mode or other mechanistic models.

The SON68 is the reference glass in the HLW disposal cells. However, the simpler synthetic glasses consisting of 3 oxides (CJ1) and 6 oxides (CJ4 = ISG, for international simple glass) will probably be used instead in Subtask 4.1 for the sake of simplicity like in Debure *et al*. (2012). The stoichiometry of these synthetic glasses is based on the French SON68 inactive reference glass composition (Table 3.12).

Table 3.12. Chemical composition of simple synthetic glasses (CJ1 and ISF) and the French reference glass SON68 (Debure et al., 2012).

[wt.%]	SiO_2	Na_2O	B_2O_3	Al_2O_3	CaO	ZrO_2	Others
CJ1	65.6	14.2	20.2				
ISG	56.2	12.2	17.3	6.0	5.0	3.3	
SON68	45.5	9.9	14.0	4.9	4.0	2.7	19.0

The dissolution this simplified glass is controlled by two kinetic processes according to the conceptual model of Gin *et al*. (2013) as represented in Figure 3.9. The global rate is the combination of an initial forward dissolution rate r_0 and long-term residual dissolution rate r_r

$$\frac{d[glass]}{dt} = r_0(T, pH, Si \dots) + r_r(T) \qquad [\ 3.18\ ]$$

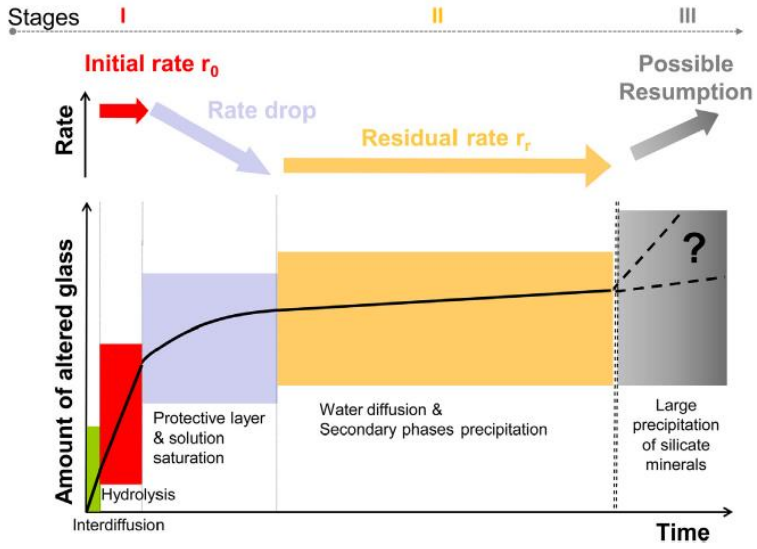

Figure 3.9. Stages of nuclear glass dissolution and related potential rate-limiting mechanisms (Gin et al., 2013).

Assuming congruent dissolution of the glass matrix, the kinetic process can be further described by the combination of a first-order initial dissolution rate $k_{0,pH}$, combined to a dependency with the bulk solution chemistry (pH, dissolved silica activity), and long-term residual dissolution rate k_r which is chemistry independent:

$$\frac{d[glass]}{dt} = -k_{0,pH}\,(H^+)^{-0.4}\,A_v\left(1-\frac{C_{Si}}{C_{Si}^*}\right) - k_r\,A_v \qquad [\ 3.19\ ]$$

This first-order rate law has already been used by De Windt *et al*. (2006) for modelling the dissolution of the R7T7 glass in a HLW disposal cell in clay host rock. Originally, it only gives a rough estimation of the rate in a narrow range of pH (7.0 – 9.5) and a temperature of 90°C but can now be up-dated for parameters at 50°C.

The activity term $(H^+)^{-0.4}$ of Equation [3.19] stands for the effect of pH, and C_{Si}^* is a saturation threshold for which the first-order dissolution stops. The reactive surface A_v depends on the degree of cracking of the vitrified waste. The rate drops when the silica concentrations approach saturation, following the well-known formalism proposed by Aagaard and Helgeson. Silica diffusion and sorption within the gel layer are not explicitly taken into account in the model and, consequently, there is no incongruent leaching of silica and boron/alkalis from the glass.

The dissolution rate terms are both temperature-dependent. Table 3.13 gives a set of parameters for Eq. 3-19 that are assumed to be operational in a crude approximation for a temperature at 50 °C and a pH range of 7 – 9.5(10). These parameters at 50°C can be used even if the temperature is lower in period III. This assumption will overestimate the degradation of the glass since the kinetics of glass dissolution decrease with temperature. The forward rate constant and residual dissolution rate of Table 3.14 were obtained for the SON68 glass in pure water and COx water. The most critical parameter is the silica threshold at saturation C_{Si}^*. It will require a sensitivity analysis or specific inputs from Task 3.

Water intrusion and glass dissolution are allowed within the whole glass zone, due to the initial cracking of the glass block before disposal, and not at the glass/canister boundaries only. The effective diffusion coefficient D_e assumed for silica and any other dissolved elements inside the (fractured) glass zone is about 10^{-10} m^2/s. The porosity is arbitrarily set to 30%.

Equation [3.19] is only applicable up to pH 9.5 (if not 10). It still remains to extend this type of equation to pH up to 11 that may correspond to the calculated altered state of the corroded steel and cement buffer. Ferrand et al. (2015) measured the short-term and long-term dissolution rate of the ISG glass (not the SON68 glass) in Old Cement Water (OCW, with pH ~11.7 controlled by the solubility of C-S-H phases). Their data are reported in *Table* 3.15 for comparison.

Table *3.13. Kinetic parameters related to the simplified HYTEC modelling of the dissolution of the glass at 50 °C and pH from 7.0 to 9.5 (– 10); see De Windt et al., 2006 and references therein; the parameters have been slightly adapted to be consistent with the parameters of Table 3.14.*

$k_{0,pH}$ [g m^{-2} d^{-1}]	3×10^{-5}	e.g. $k_{0,pH}$ $(H^+)^{-0.4}$ = 2×10^{-2} g m^{-2} d^{-1}at pH = 7
k_r [g m^{-2} d^{-1}]	10^{-4}	
C_{Si}^* [mol L^{-1}]	*(2.5×10^{-3})* (3)	
Total surface S (glass block of 400 kg)		S = 20 m^2 for a cracking ratio(1) of 10 ==> A_s = 5×10^{-5} m^2 g^{-1} (2)

(1) Ratio of the total surface on the surface of the unfractured glass block. (2) The specific surface can become a sensitivity analysis parameter if required. (3) Value from 90 °C, to be adapted as Task 3 and Subtask 4.1 will progress.

Table 3.14. Experimental data on the kinetics of SON68 glass dissolution in deionized and synthetic COx water: forward dissolution rate r_0 and residual dissolution rate r_r.

	Deionized water		COx water	
T [°C]	30 °C	50 °C	30 °C	50 °C
r_0 [g m^{-2} d^{-1}]	2×10^{-3} (1)	2×10^{-2} (1)	1×10^{-2} (1)	9×10^{-2} (1)
r_r [g m^{-2} d^{-1}]	-	1×10^{-4} (2)	(3×10^{-4}) (3)	(2×10^{-4}) (4)

(1) *Jollivet et al. (2012); (2) Fleury et al., (2014); (3) Debure et al. (2019), in situ value; (4) De Echave et al. (2018), value at 70°C, not 50°C.*

Table 3.15. Experimental data on the kinetics of ISG glass dissolution in Old Cement Water (pH 11.7) at 30 °C: short-term and long-term dissolution rates.

	OCW
T [°C]	30 °C
Short-term rate [g m^{-2} d^{-1}]	2×10^{-3} (1)
Long-term rate, similar to r_r [g m^{-2} d^{-1}]	1×10^{-5} (1)

(1) *Ferrand et al. (2015).*

3.5. Expected outcomes

Regarding the key parameters, the proposed outcomes of the reactive transport model of the HLW disposal cell in a clay formation are similar to the ones considered for the granite formation. They will be focused on the time evolution of computed key parameters at selected locations and the spatial distribution at the different materials and interfaces of computed key parameters such as:

1) pH, redox potential Eh, and concentrations of the dissolved chemical species.

2) Exchangeable cations and surface complexes.
3) Concentrations and volume fractions of the primary and precipitated mineral phases.
4) Changes in porosity and diffusion coefficients.

Those detailed results will also be interpreted in terms of lifetime or durability of the concrete buffer and steel overpack (e.g. the time at which the overpack will be breached), etc.

The list of expected outcomes provided in this deliverable could be updated at later stages of the ACED project.

The results of the present reactive transport model developed in Subtask 4.1 will be used for building abstracted models and look-up tables for Subtask 4.2 according to the approaches followed by Jacques *et al*. (2011) and Huang *et al*. (2018) for the long-term performance of cement-based materials.

3.6. Computer codes

3.6.1. The reactive transport code HYTEC

The modelling of the HLW disposal cell in clay host rock of Subtask 4.1 is performed with the reactive transport modelling code HYTEC (van der Lee *et al*., 2003).

The code forms part of a module-oriented structure which facilitates maintenance and improves coding flexibility in object-oriented C++ and parallel computing with MPI. The full set of non-linear equations of thermodynamic equilibrium is numerically solved according to the basis component approach and its matrix-algebra, using an improved Newton-Raphson scheme. The transport module is based on the representative elementary volume (REV) approach with finite volume calculation. All boundary conditions normally used by hydrogeologists are available, such as constant head or pressure, constant flow, constant concentration. They can be modified during the course of the modelling, allowing for the temporal application of different scenarios for instance.

HYTEC searches for an accurate solution to the multicomponent transport problem using an iterative, sequential, so-called strong coupling scheme. Strong coupling permits variable hydrodynamic parameters as a function of the local chemistry (Figure 3.10). For example, the porosity of a porous medium decreases after massive precipitation of newly formed mineral phases, which modifies the water flow paths and transport parameters, e.g., diffusion coefficients.

HYTEC handles 1D – 3D grids in Cartesian coordinates as well as 1D in radial and 2D in cylindrical (axis symmetric) coordinates. Heat-transfer by conduction and convection can also be modelled with HYTEC.

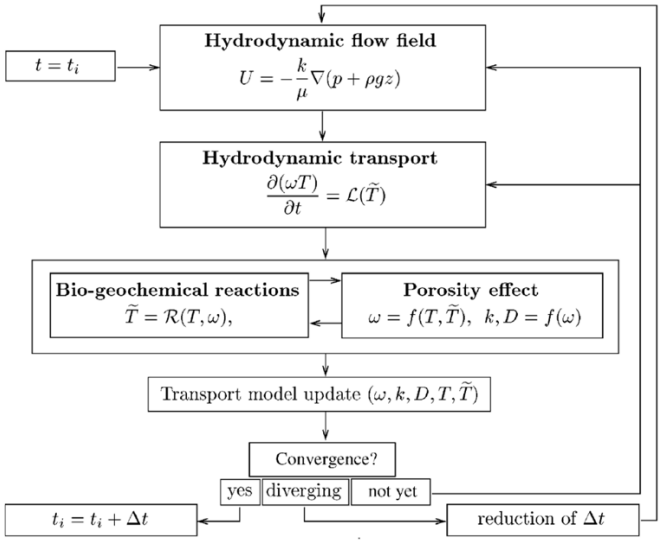

Figure 3.10. Diagram of consecutive actions within one timestep as implemented by HYTEC. T denotes total concentrations, T̃ mobile concentrations, L transport operator (hydrology) and R reaction operator (chemistry).

3.6.2. The reactive transport code iCP

iCP (interface COMSOL-PHREEQC) couples two standalone codes, the general-purpose software COMSOL Multiphysics® and the geochemical simulator PHREEQC (Parkhurst and Appelo, 2013). The interface provides a numerical platform to simulate a wide range of multiphysics problems coupled with geochemistry (Nardi et al., 2014). It is written in Java and uses the IPhreeqc C++ dynamic library and the Comsol Java API. The coupling approach is based on the operator-splitting (OS) technique. Furthermore, it takes advantage of the multicore computer architecture by balancing the computational load over different threads.

Conservative solute transport equations coupled with other physical processes are solved by COMSOL, while equilibrium and kinetic chemical reactions are solved by PHREEQC. iCP has been extensively used in geosciences and for long-term performance of engineered barriers for nuclear waste (e.g. Idiart et al., 2019).

From a geoscientific point of view, these capabilities can be summarized as:

- Hydrodynamics: saturated, unsaturated, density driven, multiphase or free laminar flow, both in porous and fracture media;
- Thermal: energy conservation, heat transfer in porous media (conduction, convection, radiation), thermal stress;
- Solid mechanics: plasticity, poroelasticity, damage mechanics;
- Chemistry: aqueous speciation, acid-base, redox, cation exchange, surface complexation, mineral dissolution and precipitation, solid solutions, etc.

Couplings between chemical and physical processes can also be considered, such as chemically-induced porosity changes and their impact on permeability or degradation of swelling properties of bentonite-based materials induced by chemical alteration processes (Idiart et al. 2020).

3.6.3. Thermodynamic database

The thermodynamic database of reference will be ThermoChimie v10.a. This is the thermodynamic database developed by ANDRA, ONDRAF and RWM for the performance assessment of the geologic disposal of radioactive waste (Giffaut *et al*., 2014, https://www.thermochimie-tdb.com). ThermoChimie provides formation constants (at temperatures ≤ 80 °C) for a wide range of radionuclides and the mineral

component of multi-barrier systems, including host-rock solid phases, bentonites, cements, steel, and their evolving secondary phases. The database is formatted for several reactive transport models including HYTEC and iCP.

Complementary data shall be taken from the Thermoddem database. This database is developed by the French geological survey (https://thermoddem.brgm.fr). The last qualified version of Thermoddem (V1.10, 2017) is formatted for several reactive transport models including HYTEC. An update version (V1.10, 2019) is under progress. Thermoddem is applicable to the full pH range, including the high-pH alkaline domain, from 0 to 100°C. The database includes a large set of zeolites and cementitious phases with a broad composition range with respect to concrete formulae such as CEM I and low-pH cements. The C-A-S-H, C-S-H and M-S-H phases are introduced as discrete elements.

Eventually, data from the PSI original development on the thermodynamic data of Fe-cement phases in the Subtask 2.2 of the ACED work package will be integrated as discrete sequences.

3.7. Summary

The description of the disposal cell in a clay sedimentary formation is based on the Belgium, Dutch and French national concepts. The first two programs rely upon the supercontainer concept. The pH has to be kept at high values in the supercontainer to limit corrosion. The French concept rely on a carbon steel liner filled with a bentonite/cement grout. The alkalinity of the grout is moderate (pH ~ 11) and should have been neutralized readily afterwards to prevent the dissolution of the nuclear glass under alkaline pH and radionuclide release. The base case includes the nuclear glass, the low alloy steel overpack, the OPC-based concrete buffer, the Callovo-Oxfordian claystone. A bentonite/cement grout (i.e. a low pH cement) is an alternative composition for the buffer. The first period for the narrative evolution and conceptual model deals with the chemical alterations before the breaching of the steel overpack (considering a thermal transient stage over 1000 y, then 25°C). The objective is to assess of the lifetime of the cement-based buffer as a function of the cement buffer thickness and composition. Enhanced diffusion properties are also investigated due to a transversal network of interconnected cracks within the degraded cement buffer. Glass alteration is only considered in the second period after the breaching of the canister with corrosion products and remaining uncorroded metallic iron. Different types of corrosion products will be tested. Eventually, a partly water desaturated degree can be modelled as an optional case with diffusion of gas (H_2, CO_2) in the system leading to cement carbonation.

The main mathematical features of the reactive transport model are presented with an emphasis on chemical feedback on porosity and diffusion. The geochemical, mineralogical and diffusion parameters of all the materials (CEM I concrete, grout, argillite) have been compiled. Kinetic rates for carbon steel corrosion have been selected from alkaline to neutral pH values. The vitrified waste is represented by the ISG (international simple glass) with a kinetic dissolution resulting from the combination of an initial forward dissolution rate and long-term residual dissolution rate.

The modelling of Subtask 4.1 will be performed with the reactive transport codes HYTEC and iCP. Those codes are interfaced with the ThermoChimie database, relevant for clayey and cement phases as well as iron corrosion products, and a dataset for modelling the sorption processes of the host rock and corrosion products. The cement/clay interactions will have an effect on the integrity of the buffer and also on the corrosion of steel overpack, e.g. by implementing a kinetic rate constant of corrosion which is pH-dependent. The cement durability cannot be separated from the evolution of the porosity and transport properties of the materials around the cement/clay interface. Carbonation may be enhanced due to the diffusion of gaseous CO_2. On the other side of the HLW cell, the dissolution of glass is explicitly coupled with the barriers and host-rock influences through the reactive transport of dissolved silica and by the precipitation of iron silicate phases. At the end, the results of the reactive transport model developed in Subtask 4.1 will be used for building abstracted models and look-up tables destined for Subtask 4.2.

4. Conceptual, mathematical and numerical models, and numerical tools of the ILW disposal cell in clay

4.1. Description of the disposal cell concept

The disposal concept studied here is based on a generic multi-barrier system including the waste matrix, the disposal container, the mortar backfill in the emplacement tunnel (where the disposal containers are located) and the clay host rock. It is assumed that the disposal cell (~ 200 m long) is part of a repository at a depth between 200 and 800 m below the surface in Clay. The schematic cross-section layout for the representative ILW disposal cell is shown in

Figure 4.1. The operation and transfer tunnels of the repository are not part of this study. Note that the presented disposal cell and the described evolution of the repository is for a generic repository, which is not related to a specific safety case.

The general shape and geometry of the emplacement tunnel mainly depends on the mechanical properties of the clay host rock and mechanical loading, the overburden at the specific site and the excavation method. Tunnels walls are supported with reinforced shotcrete for primary rock support. In this sense, the description of the proposed generic disposal cell (see

Figure 4.1) has similarities to some of the disposal cells throughout Europe. The detailed description inside the waste zone" (see

Figure 4.1) is assumed to contain 9 waste containers (with organic or metallic waste) with a backfilling material between them. Shapes of the waste containers are typically cylindrical or box-shaped; the latter being more representative in the different designs throughout Europe and for this reason selected in this work. The box-shaped waste containers are piled up in a number of stacks depending on the dimension of both, the waste package and the disposal cell. The box-shaped waste container consists of a (reinforced) concrete. Organic waste is disposed in primary metallic waste drums (i.e. 6 in this specific work) inside a disposal container which is also backfilled with cement. Metallic waste is directly disposed into the waste containers. For the modelling study, an EDZ is considered around the ILW emplacement caverns. Based on modelling results (Leupin et al. 2016), it is known that the extent of the EDZ around the L/ILW emplacement caverns will not exceed a thickness of one cavern diameter.

Organic materials such as cellulose, halogenated (e.g. PVC) and non-halogenated plastics (e.g. polypropylene, polyethylene, thermoplastics), ion-exchange resins and rubber will be present in the case of the organic wastes. Due to the different organic composition, the organic waste may consist of a single type of organic or a mixture of e.g. slow and fast degradable materials.

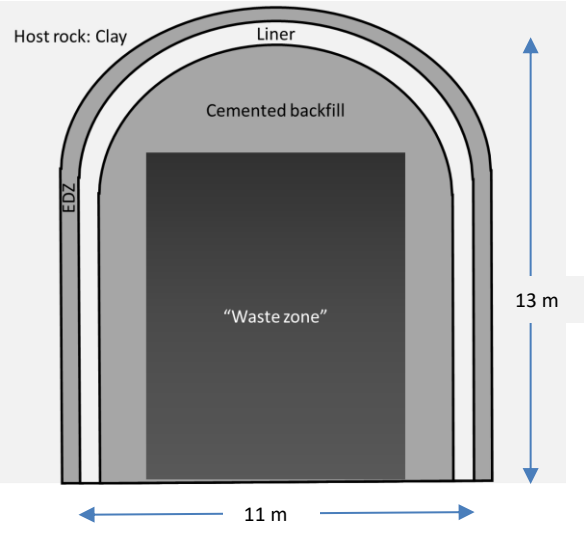

Figure 4.1. Layout of the representative ILW disposal cell in clay host rock.

Figure 4.2 shows, in more detail, the configuration and the dimensions of the generic disposal cell considered for modelling in the scope ACED. The waste inside the waste containers is not discretized in the model domain (i.e., they are treated as boundary fluxes considering the inputs from Task 3- waste package scale). This means that the different materials included in the disposal cell is as follows:

1) Functional concrete for the waste container walls (also used as filling concrete for the bottom of the disposal cell)
2) Mortar to backfill the empty spaces between waste containers
3) Mortar to backfill the empty space of the vault
4) Low-pH shotcrete liner
5) Excavation damage zone
6) Clay host-rock

Finally, the layout of the waste containers is as follows: *i)* top row: waste packages including organic waste, *ii)* middle row: waste packages with metallic waste and *iii)* bottom row: another three waste packages with organic waste.

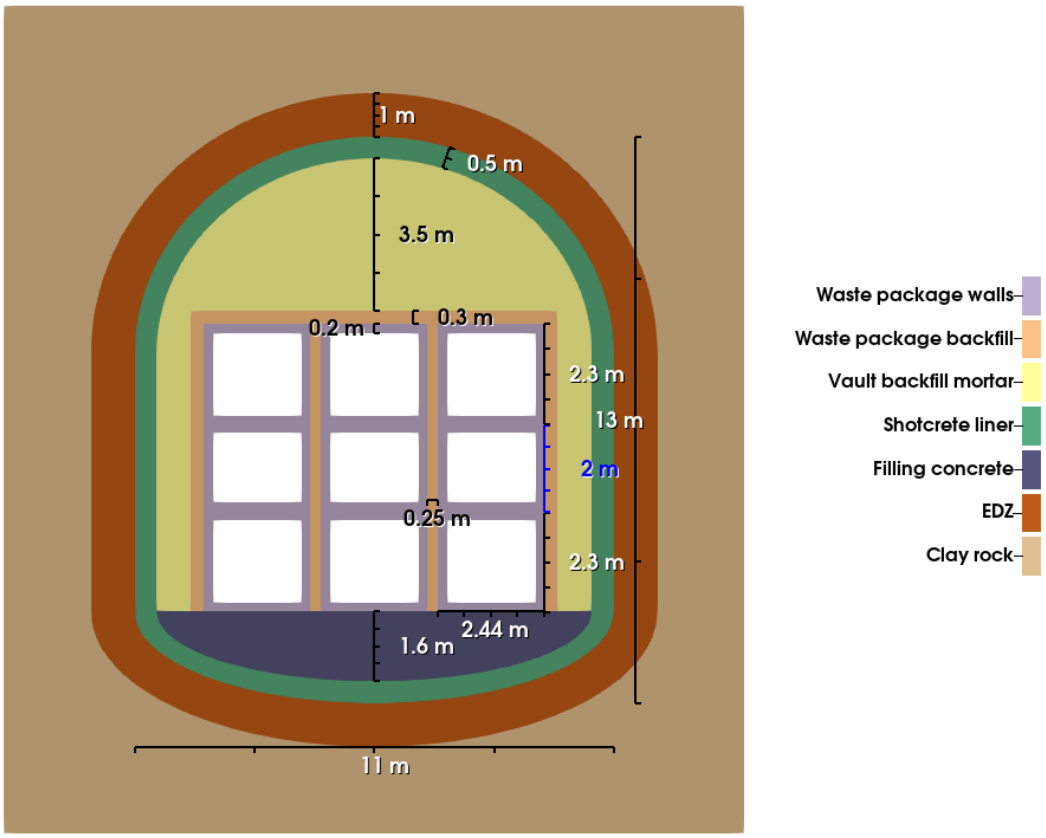

Figure 4.2. Dimensions and layout configuration of the ILW disposal cell concept in clay.

As explained above, the spatial domain considers the full scale of the disposal emplacement, whereas the temporal scale spans from the time of emplacement to up to 100,000 years (i.e., the time scale for safety assessment, where it needs to be indicated that the dose release to the surface is < 0.01 mSv/a).

4.2. Conceptual model

In terms of mass transport, water flow, diffusion of solutes (mass) and saturation of the porous media across the various material interfaces will strongly influence the extent and timescale over which chemical processes occur. Understanding the coupling of re-saturation and gas pressure development are the key factors of this system, however in our first approach only diffusion in fully saturated system will be considered which will be a worse scale scenario were the availability of water is high and consequently more chemical degradation reactions of the waste and the barriers will occur.

4.2.1. Narrative evolution

A schematic overview of the ILW repository qualitative evolution as a function of time is shown in Figure 4.3, including the possible sequence of the repository-induced effects according to Leupin et al. (2016). Similar evolution has also been described in Andra (2016a, 2016b). During the first years of disposal, the most important processes affecting the near-field chemical evolution are:

- The saturation of the concrete and cementitious grouts with porewater migrating inwards from the host rock (Nagra, 2008). Although initially the cementitious material are saturated when the waste is emplaced, due to ventilation during the construction phase, the host rock close to the tunnels will be initially desaturated.
- The significant quantities of gases (mainly hydrogen, carbon dioxide and methane) that will be generated during long periods of time by i) anaerobic corrosion of metals and ii) degradation of organic compounds by microbial and chemical processes (Poller et al., 2014 and Figure 4.4).

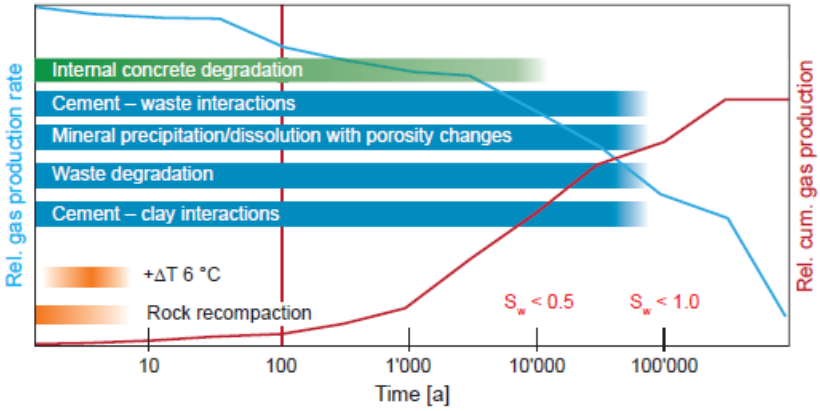

Figure 4.3. *Expected duration and intensity of the different repository-induced effects in a qualitative manner. The vertical red line indicates repository closure after approximately 100 years and Sw stands for the expected degree of saturation in the emplacement cavern*. Figure from Leupin et al. (2016).

The majority of the degradation reactions mentioned above, specially corrosion of metals, are water-mediated. A limited water influx thus limits both the rate of barrier and waste degradation and, thus, the gas generation.

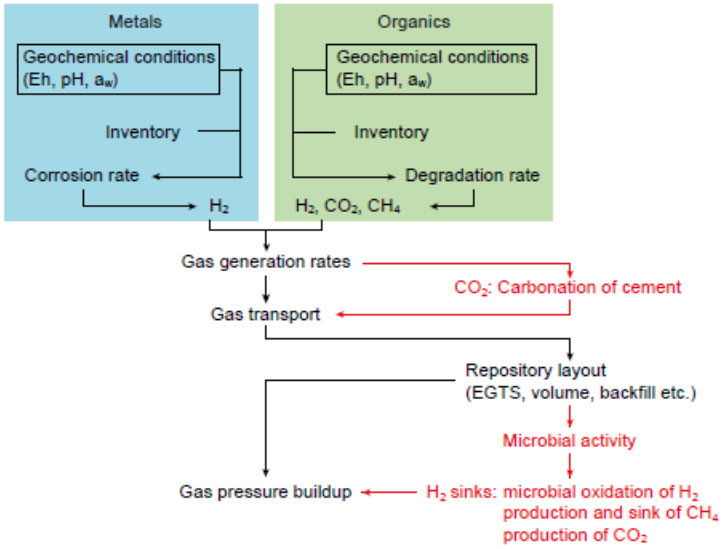

Figure 4.4. *Schematic illustration of processes leading to gas pressure build-up caused by corrosion and degradation of waste materials and processes that reduce pressure build-up.* Figure from Leupin et al. (2016).

4.2.1.1. Organic waste degradation and gas formation (CO_2, CH_4)

Organic materials within the waste packages will begin to degrade by chemical, microbiological and radiolytic processes before the repository is closed and sealed. Degradation is expected to continue at a slow rate, independently if the waste contain fast or slow degradable organics, and will lead to the production of i) gases like carbon dioxide or methane, ii) radionuclide-complexing agents such as isosaccharinic acid, EDTA, NTA or cyanide. For example, cellulose contained in the waste will degrade to a range of water-soluble organics, the most important being the isosaccharinic acid (ISA). The concentrations of organic complexants in the waste will be reduced by chemical, radiolytical or microbial degradation or sorbed on $Ca(OH)_2$ (Glaus and Van Loon, 2004). Carbon dioxide generated within organic waste degradation is expected to either react with the cementitious material. On the other hand, methane is going to accumulate in the near-field. The reactions that reduce gas pressure (i.e. carbonation of cement) build-up are called sinks and should be considered when modelling the total pressure build-up and gas transport in a repository. In addition, microorganisms may be capable of reducing CO_2 or CH_4 pressures by using these gases in their metabolic reactions.

Superplasticizers in the concrete and cementitious grouts would be an additional source of organics. Microbial degradation of superplasticizers could, in principle, result in the formation of gases such as CO_2 and perhaps CH_4, but is expected to be limited as a result of the high pH imposed by cementitious materials (Stroes-Gascoyne & Hamon 2013).

4.2.1.2. Saturation of the disposal cell and cement degradation

At the time of closure of the emplacement caverns, the backfill materials and the EDZ are not fully water-saturated. The emplacement caverns will begin to saturate only after the gas pressure decreases and approaches the hydrostatic pressure. Due to gravity and buoyancy effects, it can be assumed that any water will accumulate in the lower part of the emplacement caverns, whereas the remaining gas will move upwards. The saturation distribution in the emplacement cavern backfill will be determined basically by the capillarity of the different cementitious materials. This means that the construction concrete in the emplacement cavern, which has small pores, will be saturated rather than the mortar in the emplacement cavern roof and the emplacement cavern sides, which has large pores. Given that fully water-saturated conditions in some areas of the emplacement cavern are reached, self-sealing

processes could occur on the EDZ The self-sealing processes will be controlled by the porewater flow from the host rock into the emplacement caverns and diffusive transport, such that changes in porosity can occur both in the water-saturated cement matrix and in the host rock. During 1000 – 10 000 years, the near-field is expected to be characterized by a high pH porewater (pH = 12.5) due to dissolution of portlandite and C-S-H from cement.Throughout this period, the near-field porewater is expected to be highly alkaline (pH > 12) due to the release of alkali-ions from the cement into the water in the near-field. Cracking of cement grouts and mortars is expected to occur as well during the early post-closure period, predominantly as a result of mechanical stresses and mineral transformations. However, cracking is not expected to have a significant impact on the overall performance of the cementitious barriers (Kosakowski et al., 2014

At >10 000 years of evolution, the pH will slowly decrease from 12.5 to 10 through incongruent (non-stoichiometric) dissolution of C-S-H within the cement-based materials. According to Kosakowski et al. (2014), reactions occurring are: i) Carbonation through reaction with dissolved bicarbonate ions in porewater and through the generation of carbon dioxide gas arising from the microbial degradation of organic wastes to form calcite ($CaCO_3$). ii) Reaction of aqueous magnesium with calcium-rich minerals to form magnesium hydroxide (brucite, $Mg(OH)_2$). iii) Reaction of aluminium with calcium and sulphate in porewater to form sulphate minerals such as ettringite. These reactions (the interaction of pozzolanic material with the alkaline pore solution and the interaction between siliceous aggregates and alkaline cement pore solution) may influence both the evolution of the mineralogical composition of the cements and the composition of the cement-equilibrated porewater. The potential significance of such reactions depends on the composition of the porewater, the concentrations of the solutes and volume changes associated with mineralogical changes. The spatial distribution of such precipitates also may influence the evolution of the heterogeneity of the near-field.

4.2.1.3. Steel corrosion, H_2 generation and redox processes

Redox processes in the repository will be initially dominated by the consumption of oxygen (present as entrapped air) through the corrosion of steel waste packages, the metallic waste, the host rock and the engineered structures such as rock bolts. Microbial consumption of O_2 is not expected to be significant, due to the interaction with the clay host rock very high pH of the cementitious environment. Goethite is a likely product of aerobic steel corrosion, which can only be formed during the first few hundred years, when residual amounts of oxygen are probably available (Leygraf and Graedel, 2000). The production of goethite from steel will be based on the Pilling-Bedworth ratio (*elementary cell volume of metal oxide to the elementary cell volume of the equivalent metal where the oxide has been created*) increasing by 300 % the molar volume (Leupin et al. 2016), leading to cracking of grout around the waste packages and shotcrete. With time, all oxygen will be consumed and steel will corrode anaerobically, leading to the production of hydrogen through the dissociation of water. Because, after a few decades, gas pressure in the emplacement caverns will exceed the hydrostatic pressure, permanent porewater outflow from the emplacement caverns into the host rock will develop (Leupin et al. 2016). The water needed for maintaining anaerobic corrosion is provided predominantly through vapour diffusion from the host rock (Nagra, 2008). Additionally, other near-field materials may take part in redox-buffering reactions (e.g. blast furnace slag in cementitious grouts; degradation of organic materials in waste packages; degradation of superplasticizers in cementitious materials) to lower the porewater redox potentials. Microbially mediated reactions may also influence redox conditions (although the high pH may reduce the rate of microbial activity) and, these reactions tend to drive the system towards chemically reducing conditions. During 1000 – 100 000 years, the near-field is expected to have chemically reducing conditions due to the continuing anaerobic corrosion of the steel waste packages and engineered structures (Nagra, 2014). Magnetite will form directly from steel corrosion and $H_2(aq)$ is expected to be generated and will accumulate in the aqueous solution until it reaches its solubility limit. Once reached this limit, $H_2(g)$ escapes from the system and redox conditions stabilize. Based on the Pilling-Bedworth ratio, there is a 110 % increase in solid molar volume for the conversion of steel (Fe) to magnetite, which means that a continued expansion of corrosion products will further decrease porosity, potentially inducing cracking of grouts and mortars. Gas migration through the host rock via

diffusion is relatively slow (D_{app} ~ 10^{-10} m^2/s determined for He Jacobs et al. 2013), so it is expected that some pressurization in the near-field will occur as a free gas phase develops, but the high porosity backfill is designed to mitigate the localised build-up of excessive gas pressures and seals will allow passage of gas while restricting flow of water.

Anaerobic corrosion processes will change the saturation conditions in the backfill and the surrounding host rock. Water saturation in the backfill will be reduced due to the low rock permeability (hydraulic conductivity (K) of clays ≤ 10^{-12} m/s), because the water consumption by the corrosion process may not be fully compensated by the influx of porewater through the host rock. Furthermore, gas pressures build-up in and around the emplacement caverns will limit the influx of porewater from the host rock for a very long time period. Therefore, it is expected that the unsaturated zone in the host rock will increase and that the degree of saturation in the emplacement cavern backfill will stabilise for a long time, close to the level of the residual saturation (Nagra, 2008). A closer analysis of the two-phase flow processes in the unsaturated zone shows that, with an increasing gas pressure, the gas-filled pore space in the host rock remains unchanged (macropores > 25 nm), whereas the influx of porewater is restricted to pores with smaller pore radii (Papafotiou & Senger, 2014). Possible hydro-chemical interactions are consequently restricted predominantly to diffusion processes in the continuously water-filled meso and micropore space of the host rock.

The gas transport will take place predominantly along the engineered gas transport system (not considered in this work) and, to a lesser extent, through the host rock. As a result of gas overpressures in the emplacement caverns, the gas migration pathway through the engineered system and the host rock will be kept open over a period of more than 10 000 years (Diomidis et al., 2016). Thus, the unsaturated zone in the rock around the emplacement caverns will also provide an important contribution to gas migration, because possible hydro-chemical sealing processes will be restricted principally to the water-saturated pore space within the micro- and meso-pores, whereas the effective gas transport capacity of the unsaturated zone will be determined by the gas-filled macropores. In addition, there may be small increases in the volume of cement grouts and concretes, with a more substantial expansion of steel due to the corrosion, potentially leading to cracking of grouts/mortars.

At > 10 000 years, the reducing capacity of the L/ILW disposal system is very large because of the presence of large amounts of steel (e.g. in structural supports, metallic waste and waste containers). It is assumed that, on the long term, steel corrosion will continue to lead to the formation of magnetite, which is the thermodynamically stable iron phase under the expected near-field conditions. Gas is continuously produced from the corrosion of metals, but the production rate is expected to have significantly declined by this time. The corrosion gas generated could still circulate freely in the unsaturated areas of the emplacement caverns, for example in the roof or in the highly porous mortar in the emplacement cavern side walls, such that transport through the host rock and along the engineering system is still possible. On the basis of the model calculations (Nagra, 2008), it is expected that saturation of the emplacement caverns will begin eventually after more than 100 000 years, in the late gas generation phase. At that point in time, an unsaturated zone of several meters will have formed in the host rock around the emplacement caverns, in which the mobility of gas is increased significantly. This is valid also for the emplacement cavern plugs and the backfilled access and operational tunnels. In this gas-filled pore space, occurrence of self-sealing processes due to hydro-chemical interactions can largely be excluded, such that the gas transport capacity of the engineering barriers and the host rock will not be reduced significantly. Considering the reduced gas generation rate during this late phase, a renewed gas pressure build-up through hydro-chemical self-sealing processes can be excluded. Model runs of the two-phase flow conditions in the emplacement cavern near-field indicate that the emplacement caverns as well as the EDZ in the host rock exhibit relatively high gas saturations over time periods of 100 000 years (Diomidis et al., 2016). Over this very long timescale, the EBS is not expected to provide complete containment. However, the degraded EBS barriers are expected to continue to retard the release of radionuclides by chemical interactions, although by this time the vast majority of the radionuclide inventory will have decayed. At the end of the gas generation phase, the unsaturated zone in the host rock and the emplacement cavern backfill will decrease and the gas

pressure in the emplacement caverns will equilibrate with the hydrostatic pressure. Some isolated zones with a free gas phase will remain (i.e. trapped gas, most likely at the top of the emplacement caverns), which will disappear eventually through dissolution processes. Hydro-chemical interactions as a result of advective and diffusive mass fluxes could lead to a self-sealing process at the host rock/concrete matrix contact in the saturated space and thus reduce the porewater flux.

4.2.1.4. Interface processes between clay host rock/cement and steel/cement

Chemical interactions between repository barriers (engineered and natural) are driven by chemical, thermal, and hydraulic gradients, which evolve in space and time in the repository system. The use of contrasting materials, such as clay, cement/concrete, and steel leads to sharp chemical gradients at interfaces. The interactions of the materials are influenced by various chemical reactions and transport processes coupled in a non-linear fashion. Dissolution and precipitation processes, as well as ion exchange reactions, might alter the pore space with accompanying changes in material characteristics (transport, flow, and mechanical properties).

4.2.2. Hydrodynamic processes and gas transport

In terms of mass transport, water flow, diffusion of solutes (mass) and saturation of the porous media across the various material interfaces will strongly influence the extent and timescale over which chemical processes occur. Understanding the coupling of re-saturation and gas pressure development are the key factors of this system, however in our first approach only diffusion in fully saturated system will be considered which will be a worse scale scenario were the availability of water is high and consequently more chemical degradation reactions of the waste and the barriers will occur. It is worth mentioning that, although it is well established that gas generation in the ILW disposal cell may not allow full saturation to occur even for the considered timeframe of 100,000 years (Nagra, 2008), the governing equations of multiphase flow pose a tremendously challenging problem when there is a need for a coupling with chemical reactions. Therefore, the choice of a model assuming full saturation is a compromise that has been selected to be able to incorporate mechanistic-based chemical processes in the disposal cell and to perform simulations in a manageable time to obtain results within the time frame of the Task. The gas transport mechanisms and relevant hydro-mechanical and hydro-chemical couplings were analysed and evaluated by Nagra (2008) and Kosakowski et al. (2014).

4.2.3. Thermal processes

The temperature increase originated mainly from the hydration of cementitious materials and in less extend by the radioactive decay of the waste can accelerate chemical reactions, change the stability of minerals and accelerate diffusive transport. However, these effects will be minor for the likely increase of temperature in the host rock of 5 – 10° C above ambient temperatures in the first decade after closure of the repository and will not be considered in the present work.

4.2.4. Chemical processes

Detailed descriptions of the chemical evolution of the near field of a L/ILW repository in Opalinus Clay have been previously described in the literature (Nagra, 2002; Kosakowski et al., 2014). Similar, process are also expected in a L/ILW repository in Callovo Oxfordian (ANDRA, 2006), which is the clayrock selected in this study. The influence of individual classes of waste, such as metals or organic compounds, on the long-term performance of the near-field can be assessed based on expected chemical transformation processes (i.e precipitation and dissolution processes, cation exchange, surface complexation in thermodynamic equilibrium) and on the evaluation of possible interactions between the waste, their degradation products and cement hydrated phases and aggregates.

4.2.5. Coupling effects

Cracking of cement grouts and mortars is expected to occur as well during the early post-closure period of an ILW repository, predominantly through the hydration of cements and also as a result of mechanical

stresses from the thermal expansion of engineering barrier system and mineral transformations. However, this process will not be considered in this work. Instead porosity changes due to reactions and feedback in transport will be considered.

4.3. Mathematical model

In this section, the considered mathematical relationships arising from the conceptual model of the ILW disposal cell are presented. In general, the physical and chemical evolution of the ILW disposal cell has been conceptualized in a framework that integrates multicomponent transport in porous media coupled with chemical reactions. Initially, the transport of solutes is assumed to take place under isothermal fully water-saturated media throughout the emplacement cavern, the EDZ and the host rock. Moreover, concentration gradients drive solute transport (diffusion-controlled), neglecting the impact of hydraulic gradients (i.e., low permeability of the clay rock and cementitious materials). A strong non-linearity is induced when coupling the constitutive relationships of the transport of solutes to a non-linear source/sink term due to chemical reactions. The coupling of the solute transport to chemical reactions is done through the so-called operator-splitting approach, which shows significant computational advantages over a global implicit approach (Lu et al., 2022).

4.3.1. Reactive transport equation

Considering the above conditions, the reactive mass transport equation can be simplified into

$$\frac{\partial(\phi c_i)}{\partial t} - \nabla \cdot (\phi \boldsymbol{D} \nabla c_i) + R_i(c_1, \dots, c_n) = 0, \quad i = 1, \dots, n, \qquad [\ 4.1\ ]$$

where ϕ is the porosity, c_i [mol m^{-3}] is the concentration of component i and R_i [mol m^{-3} s^{-1}] is the reactive source and sink term of component i computed by the operator-splitting approach considering n components. The hydrodynamic dispersion tensor $\boldsymbol{D}$ is reduced, in the case of no advection and isotropic diffusion-controlled transport, to the effective diffusion coefficient with the form

$$D_e = \phi D_p, \qquad [\ 4.2\ ]$$

where D_p [m^2 s^{-1}] is the pore diffusion coefficient accounting for tortuosity and connectivity effects. The previous system of partial differential equations is the chosen set of governing relationships that fully describe the physical and chemical evolution of the disposal cell.

Even under fully saturated media, only a handful of extremely simplified reactive transport models can be solved analytically. Typically, to be able to solve the resulting system of equations, practitioners employ numerical methods. In the present work, the Galerkin Finite Element Method along an implicit Euler method for the temporal discretization are used. The resulting discretized mathematical model has been implemented in the open-source software OpenGeoSys-6 (Kolditz *et al.*, 2012a). In the operator-splitting approach a two-step process is carried out. First, the transport equations are solved. This is followed by a reaction step, where the term R_i is computed (usually by calling an external algorithm). In the present work, the external algorithm used is the geochemical solver PHREEQC (Parkhurst and Appelo, 2013).

4.3.2. Chemical processes

Several chemical processes play an important role in the dynamic interaction between each cementitious material and the clay rock. At the disposal cell scale, all chemical processes being considered are assumed to evolve under thermodynamic equilibrium. However, kinetically-controlled processes occurring in the waste package domain (i.e., steel corrosion and organic waste degradation) are incorporated into the disposal cell model as simplified source terms calculated according to the numerical results of Task 3 (“package scale”). Two main approaches are commonly used to compute

the equilibrium states of the chemical system: *i)* the Gibbs energy minimization method or *ii)* the solution of the law of mass action system of equations. For the coupling of the reactive transport model calculations, the latter approach used by PHREEQC is selected, but they lead to exact same geochemical equilibrium state. In what follows, the processes that drive the chemical and physical evolution of the disposal cell are briefly described.

4.3.2.1. Aqueous complexation

4.3.2.2. Aqueous complexation reactions are assumed to happen instantaneously. Therefore, they can be modelled as equilibrium reactions, where information about the stoichiometry, thermodynamic activity coefficients and equilibrium constants of each reaction is needed. Details of this process have been described in Section **Erreur ! Source du renvoi introuvable.** of this report. Mineral dissolution/precipitation

All mineral dissolution/precipitation reactions are also assumed to happen under thermodynamic equilibrium conditions. In this context, the reason is two-fold. First, in a previous study, it has been found that the kinetically-controlled dissolution/precipitation of minerals when considering the interaction of Callovo-Oxfordian and cementitious materials does not have a major effect in the overall evolution of the system (Idiart *et al.*, 2020). And second, the computational expense of adding kinetic reactions to the reactive transport model can be an issue when considering long-term simulations and large spatial domains.

However, the characterization of the mineralogical evolution due to dissolution/precipitation is one of the most important processes in this work. This is because it will have a major impact over both the aqueous chemistry evolution and the physical alterations due to changes in the volumetric proportions in the cementitious and clay domains, resulting in temporal changes of the media porosity, and, in turn, the effective diffusion of each material. Mathematical and chemical details of this process can be found in Section **Erreur ! Source du renvoi introuvable.** of this report.

4.3.2.3. Cation exchange and surface complexation

Cation exchange reactions can also be modelled as equilibrium processes. As described in Section **Erreur ! Source du renvoi introuvable.**, these processes are based on the Gaines-Thomas convention. Cation exchange can be considered for both the cementitious materials and the clay rock. On the one hand, the characterization of cation exchange reactions in the cementitious system is important for alkali uptake (Na and K) in the C-S-H phases. On the other hand, both cation exchange and surface complexation reactions may be considered for the clay rock. It is worth noting that the latter process may be important for buffering the pH of the clay porewater.

4.3.2.4. Redox reactions

Generalities about redox reactions have been described in Section **Erreur ! Source du renvoi introuvable.** of this report. In the ILW disposal cell, redox processes are mainly considered due to the presence of dissolved iron in both the cementitious materials and, in the clay rock. This concentration gradient and other potential process (e.g., the generation of $H_{2(aq)}$ in the inner domains of the cell by iron corrosion) will lead to the formation of Fe(II)-bearing minerals at the interfaces of the disposal cell (e.g., formation of magnetite at the cement-clay interface). Therefore, redox reactions constitute an important chemical process in the evolution of the cell.

4.3.2.5. Chemically induced porosity evolution

The porosity change due to chemical reactions completes the description of the chemical and physical evolution of the disposal cell in this work. This process ties the mineralogical changes due to dissolution and precipitation to the porosity and effective diffusion coefficient. Because, ultimately, all interfacial interactions among the cementitious materials and the clay rock depend on the diffusion properties of each material, this process is considered as an important factor in the long-term evolution. The porosity change is computed in each time step and spatial position by adding or subtracting the change in volume

fraction of each mineral that dissolves or precipitates obtained in the chemical calculation step. This change in porosity is then passed as feedback to the transport equations in the operator-splitting approach. As mentioned, the porosity-diffusion feedback is modelled as a linear relationship between the effective diffusion and pore diffusion coefficients (see Eq. [*4.2*]).

4.3.3. Initial and boundary conditions

Initial conditions of fully equilibrated systems for all cementitious materials and the clay rock are used in the reactive transport simulations. First, calculations of cement hydration are carried out to obtain the mineralogical composition and equilibrated porewater concentrations of each cementitious material. It is worth noting that, in cement hydration calculations, aggregates are considered inert materials with a density equal to quartz. In order to maintain consistency, cement aggregates are also considered chemically inert in the reactive transport model.

The mineralogical composition and porewater of the clay rock have been reported previously (Marty *et al.*, 2014). However, it is important to ensure that all considered cement minerals do not disturb the initial equilibrium state of the clay rock. This could be the case of some zeolite minerals, which are important in cement-clay interactions (Ma and Lothenbach, 2020), but due to the lack of maturity in the data when this report was written, may be suppressed from the calculations. If during the project, some more data is published, may it will be considered. The overall challenge is to set up a consistent initial chemical state for the reactive transport model considering all cementitious materials and the clay rock, as well as the considered secondary phases. Furthermore, cement hydration calculations (which are not part of the reactive transport processes) are carried out using the Gibbs energy minimization approach (with the GEM-Selektor software (Kulik *et al.*, 2013)), whereas, as mentioned, the reactive transport simulations are done by coupling OpenGeoSys to PHREEQC. Thus, special care should be taken when transferring information from one software to another, since the different approaches for geochemical calculations should not lead to significant differences when using the same thermodynamic database.

Boundary conditions can be incorporated as constant (Dirichlet) or no-flux (Neumann). When considering the degradation of the cementitious materials induced by the contact among them and the clay rock, no-flux boundary conditions can be applied around the complete domain. However, it should be noted that a sufficiently sized sub-domain for the clay rock may be required to neglect the effect of the outer boundary onto the chemical profiles. On the other hand, constant boundary conditions can be imposed onto the inner walls of the waste packages as a simplified source term to consider gas diffusion in the disposal cell.

4.4. Sensitivity cases

In terms of mass transport, water flow, diffusion of solutes (mass) and saturation of the porous media across the various material interfaces will strongly influence the extent and timescale over which chemical processes occur. Understanding the coupling of re-saturation and gas pressure development are the key factors of this system, however in our first approach only diffusion in fully saturated system will be considered which will be a worse scale scenario were the availability of water is high and consequently more chemical degradation reactions of the waste and the barriers will occurs.

In order to compare the coupling of different chemical processes and gain confidence in the ILW disposal cell concept, several sensitivity cases are proposed with increasing complexity:

1) Aqueous complexation + mineral dissolution/precipitation
2) Aqueous complexation + cation exchange + mineral dissolution/precipitation
3) Aqueous complexation + cation exchange + mineral dissolution/precipitation + redox processes
4) Aqueous complexation + cation exchange + mineral dissolution/precipitation + redox processes + porosity diffusion feedback

All proposed sensitivity cases are simulated under fully saturated isothermal media. To reduce the computational burden of the sensitivity simulations, the above four cases can be solved considering a simplified 1-D geometry (see Figure 4.5) including all the cementitious materials of the disposal cell and the clay rock. Smaller temporal scales (e.g., 10,000 years) may also be used for this purpose.

Figure 4.5. Model setup for 1-D cases in the ILW disposal cell in clay.

After the simulation of the above cases, a full reference case considering the upscaling to a 2-D geometry and the full temporal scale (100,000 years) shall be simulated. This 2-D domain may be composed of complex geometries using an unstructured computational mesh to accommodate to a particular configuration design in the disposal cell (e.g., the layout of waste packages in the waste matrix). Because of the required number of mesh elements for the 2-D case resulting in large computational times only one case accounting for all chemical processes and couplings can be considered. An optional case for multiphase reactive transport can also be simulated; however, this is subject of further coupling developments in the numerical algorithms currently available in OpenGeoSys-6.

4.5. Parameter values

This subsection provides the physical and chemical properties of each entity in the disposal cell concept. As mentioned, all cementitious materials, the EDZ and the intact host rock have been conceptualized as homogeneous porous media. On the one hand, the governing transport equations considering diffusion as the main transport mechanism require information about the pore diffusion and porosity of the media. It is assumed that all solutes have the same diffusion coefficient in each material. This means that anion exclusion effects are neglected from the calculations.

The diffusion coefficients and porosities have a principal role in the degree of cement degradation and cement-clay interactions. On the other hand, the intrinsic permeabilities of the media do not have an effect on diffusion-controlled interactions. However, in the present work, they are reported for each material to enable the possibility of a scenario in which there is advective flow in the disposal cell (e.g., increase of porosity in the EDZ). In this case, the permeability-porosity coupling can be computed with a Kozeny-Carman type relationship (Kozeny, 1927; Carman, 1937). Note, however, that if such scenario is considered, the evolution of cracks in the clay rock would not be modelled.

The chemical parameters consist of equilibrium constants (i.e., *log K* values) for each equilibrium reaction under standard conditions. These include aqueous complexation reactions, mineral dissolution/precipitation reactions, cation exchange and surface complexation reactions. When considering changes of porosity due to precipitation/dissolution of minerals, standard molar volumes [m^3/mol] for each mineral are required. All this information is contained in the same chemical thermodynamic database. For cementitious materials, the database CEMDATA v18.1 (Lothenbach *et al.*, 2019) shall be used for all cement hydration calculations.

For reactive transport calculations, additional thermodynamic data about some clay minerals not found in CEMDATA is retrieved and adapted to match the same master species of CEMDATA from the latest version of the ThermoChimie database (Duro *et al.*, 2012). Finally, in the case of surface complexation

in the clay rock, the diffusive-double layer model (Dzombak and Morel, 1990) is selected, where additional information about number of binding sites, site density and specific area are required. For clay minerals illite and montmorillonite, surface complexation constants are available in several previous studies (Bradbury and Baeyens, 2005a; Bradbury and Baeyens, 2005b; Marques *et al.*, 2012).

4.5.1. Physical parameters

As mentioned, intrinsic permeabilities do not have a significant effect for the modelled scenarios in this work. Their parameters, however, have been taken for cementitious materials based on typical data described in the literature. For the functional concrete walls, a value of 1×10^{-19} m^2 is commonly used in calculations (Bamforth *et al.*, 2012). The waste package and vault backfill mortars are highly porous materials. Typical values of intrinsic permeability due to the higher interconnection of the pore structure are selected in the range of 5×10^{-13} and 3.1×10^{-10} m^2 for the waste package and vault backfill mortars, respectively (Crossland, 2007; Nagra, 2008). A typical intrinsic permeability of a low-pH shotcrete liner is in the order of 1.02×10^{-17} m^2 (Bamforth *et al.*, 2012) and is selected for this work.

The permeability of the intact Callovo-Oxfordian clay rock has been characterized previously (Enssle *et al.*, 2011). Horizontal and vertical hydraulic conductivities of 7×10^{-13} and 4×10^{-13} m/s have been reported. Assuming standard conditions, the resulting intrinsic permeabilities are about 7×10^{-20} and 4×10^{-20} m^2. In the case of 1-dimensional transport, the vertical permeability for the COx is used. The permeability of the EDZ is estimated assuming a maximum hydraulic conductance of 1×10^{-7} m^3/s following a methodology reported elsewhere (Leupin *et al.*, 2016).

The porosities of all cementitious materials are calculated via thermodynamic modelling of cement hydration. The calculated porosity corresponds to water accessible porosity only, where interlayer water found in some solid phases (e.g., C-S-H phases) is not considered as void space in the reactive transport model. Further details of the cement hydration calculations can be found in section 4.5.2 of this work. A summary of the physical parameters is shown in Table 4.1.

4.5.1.1. Functional concrete walls

Low effective diffusion coefficients (D_e~10^{-12} m^2/s) are typical values for concrete (McCarter *et al*., 2000). In Idiart *et al.* (2020), a $D_e = 10^{-12}$ m^2/s was used for a concrete with a 4% porosity. Other typical values are in the range of ~10^{-11} m^2/s (Govaerts and Weetjens, 2010). Based on the previous data and because it is well-known that a higher porosity will yield higher diffusivity in the concrete (Ait Mouheb et aI., 2022), it is estimated that the concrete with a calculated porosity of 8.5% (see section 4.5.2) corresponds to a small change in diffusivity resulting in a $D_e = 2.12 \times 10^{-12}$ m^2/s (i.e., a simple linear relationship between porosity-diffusion).

4.5.1.2. Waste package backfill mortar

Same properties than the ones selected for the vault backfill mortar. See section 4.5.1.3

4.5.1.3. Vault backfill mortar

The calculated porosity of the mortar is 29% (almost double of the functional concrete) obtained in the cement hydration calculations. This cementitious material can be categorized as highly porous. Therefore, an estimated value approximately one order of magnitude larger than that of the functional concrete ($D_e = 2.87 \times 10^{-10}$ m^2/s) is selected in this work which corresponds to a pore diffusion coefficient of 1.0×10^{-9} m^2/s. This high pore diffusion coefficient consider the effect of the higher interconnection of the pore structure in the mortar and a corresponding higher impact on diffusivity

4.5.1.4. Shotcrete liner

To keep consistency with the previous assumptions about the diffusivity of the cementitious materials, a D_e in the order of 5×10^{-11} m^2/s is the estimated effective diffusion coefficient of the shotcrete (porosity = 24%) and is selected for the reactive transport model.

4.5.1.5. Excavation damage zone and Callovo-Oxfordian host rock

It is assumed that the EDZ extends for 1 m through the tunnel at the time of emplacement. As a modelling simplification, the permeability, porosity and pore diffusion of the EDZ is homogenized. Data for porosities and effective diffusion coefficients of both the EDZ and the intact host rock are taken from previous cement-clay interactions studies (Marty *et al.*, 2014). The pore diffusion coefficients selected for this work are 2.60×10^{-10} and 1.44×10^{-10} m^2 s^{-1} for the EDZ and the intact clay rock, respectively.

4.5.1.6. Summary of transport parameters

In Table 4.1. , a summary of the physical parameters corresponding to each cementitious material and the clay rock is presented. Note that porosities for the cement-based materials are calculated based on the hydration models (section 4.5.2). Intrinsic permeability of the same materials are based on Bamforth et al. (2012). However, should be kept in mind that due to the low permeability of these materials, high uncertanties of these values are expected. It is worth noting that, for the case when there is porosity change induced by chemical reactions, these parameters represent initial values that change over time depending on the previously mentioned linear relationship between the porosity and the effective diffusion coefficient. If the case of advective flow is considered, as mentioned, a Kozeny-Carman type relationship between porosity and permeability can be used.

Table 4.1. Input physical data of materials used in the reactive transport model of the ILW disposal cell in clay.

Material	Pore diffusion coefficient [m^2/s]	Intrinsic permeability [m^2]	Porosity [-]	Effective diffusion coefficient [m^2/s]
Functional concrete (waste container walls)	2.49E-11	1.00E-19	0.085**	2.12E-12
Waste package backfill mortar	1.09E-09	3.10E-14	0.29**	2.87E-10
Vault backfill mortar	1.09E-09	3.10E-14	0.29**	2.87E-10
Low-pH shotcrete liner	2.08E-10	1.02E-17	0.24**	5.00E-11
Excavation damage zone (EDZ)	2.60E-10	1.20E-16*	0.20	5.20E-11
Callovo-Oxfordian (COx) host rock	1.44E-10	4.00E-20	0.18	2.60E-11

*Calculated assuming a maximum hydraulic conductance of 1e-7 m^3/s (Leupin *et al.*, 2016) where $\mathrm{K}\left[\frac{m}{s}\right] = \frac{1e-7\ m3/s}{A_{EDZ}}$ and $A_{EDZ} = (r_{EDZ}{}^2 - r_0{}^2)$ with $r_{EDZ} = 14$ m and $r_0 = 13$ m (top of emplacement cavern).

**Estimated by thermodynamic modelling of cement hydration (see section 4.5.2).

4.5.2. Recipes of cementitious materials

All cementitious materials use CEM I 42.5 N cement with a normative composition described previously (Liu *et al.*, 2014) and shown in Table 4.2. Note that the cemented waste inside the waste containers is not part of the model (i.e., they are treated as boundary fluxes considering the inputs from Task 3- waste package scale) and for this reason the cement used inside of the container is not specific in this report.

Aggregates, which make up about 70% of the hydrated concrete and mortars, are considered chemically inert with a density equal to quartz. The superplasticizer added to the shotcrete is also chemically inert, whereas the set accelerator is based on the one described in Lothenbach *et al.* (2014). In addition, an amount of 10^{-6} g / 100 g of NaCl was added in order to have charge balanced solutions during the hydration model.

Further details concerning cement hydration modelling can be found in Lothenbach *et al.* (2008). The recipes for each material are summarized in Table 4.3. Note that in the materials where silica fume is added, it has been simplified to 100% SiO_2. The resulting cement hydration mineral and porewater compositions are detailed in the following subsections. As mentioned, one of the outcomes of this modeling stage is the calculation of an initial porosity for each material. This was done by subtracting the volume of water to the total volume of the concrete for the fully equilibrated system. Moreover, it is assumed that a void space filled with gas of about 5% is present in the final equilibrated materials which is already considered in the porosities given in Table 4.1.

Cement hydration modelling is done in the software GEM-Selektor using the CEMDATA v18.1 thermodynamic database. In all calculations, the CSHQ model (Kulik, 2011) for the calcium silica hydrate phases is selected. Further, M-S-H (magnesium silica hydrate) phases (Bernard *et al.*, 2019), which have been made available in the current version of CEMDATA, are enabled. The fully hydrated cementitious materials correspond to the initial state of the reactive transport calculations and their compositions are shown in following subsections.

Table 4.2. Normative phase composition of CEM I 42.5 N used in the cement hydration calculations.

Phase	**g/100 g**
Alite	58
Belite	10
Aluminate	7.6
Ferrite	7.5
CaO (free)	0.6
$CaCO_3$	4.8
K_2SO_4	1.6
$CaSO_4$	3.6
Na_2SO_4	0.1
K_2O	0.1
Na_2O	0.05
MgO	1.4
SO_3	0.16
Inert	4.49

Table 4.3. Input recipes of cementitious materials in the ILW disposal cell in clay.

Component [g]	**Functional concrete**	**Waste package backfill mortar[d]**	**Vault backfill mortar[e]**	**Shotcrete liner[f]**
Water/binder	0.45	1.25	1.25	0.90

Water	45	125	125	90
CEM I 42.5 N[a]	100	100	100	60
SiO_2	0	0	0	40
Aggregate[b]	400	533	533	532
Calcite	45	0	0	0
Set accelerator[c]	0	0	0	6
Superplasticizer	0	0	0	2

[a](Liu *et al.*, 2014). [b]Inert quartz. [c]As reported in (Lothenbach, Rentsch and Wieland, 2014[). d)] Same composition than vault backill mortar. [e]Based on Mortar M1 (Nagra, 2008) and NRVB (Bamforth *et al.*, 2012). [f]Recipe as reported in (García Calvo *et al.*, 2010) with simplified silica fume as SiO_2.

4.5.3. Chemical parameters

All primary and secondary minerals for both the cementitious system and the host rock have been enabled in cement hydration calculations for each material. It is important to note that this is a crucial step in preparing the initial chemical state for the reactive transport simulations. The reason is, as it has been mentioned, to attain a chemically consistent initial state for the subsequent interactions in the system. On the other hand, some minerals that are known to form have been suppressed from cement hydration calculations. This is the case of thaumasite, which becomes an intermediate phase during cement degradation and has been suppressed for all cementitious materials. Furthermore, although zeolites are important during cement-clay interactions (Lothenbach *et al.*, 2019; Ma and Lothenbach, 2020), they have been suppressed because of current lack of sufficiently accurate data. If considered, they form in the initial equilibrium state in the clay rock, which disturbs the mineralogical composition of the clay. This should not be the case when there is no interaction with the alkaline porewater of the cementitious materials of the disposal cell.

GEM-Selektor handles C-S-H (using the CSHQ model (Kulik, 2011, Kulik et al. 2022) and M-S-H phases as ideal solid solutions. During cement hydration, this has been enabled, since these mineral phases are important components of the cementitious system. The CSHQ solid solution model has been selected for all cementitious materials. On the other hand, some additional solid solutions, which is the case of ettringite and straetlingite, have been modelled as single equilibrium phases. In the PHREEQC version of CEMDATA (which is used in the reactive transport model), solid solutions are also handled as ideal, where information about its end members is available in the database. This may be enabled during reactive transport calculations; however, some simplifications of the C-S-H and M-S-H solid solutions may be necessary (e.g., selecting a single end member to represent the solid solution) for simplicity.

Cation exchange reactions are commonly used to model surface phenomena in the cementitious materials. However, there is a large data gap in this regard, where only a few studies have published mechanistic models for these types of chemical processes. In general, the cation exchange reactions are simplified to simulate the uptake of K and Na in the C-S-H phases, neglecting the uptake of Al and Mg. A model based on the work of Missana *et al.* (2017), considering a cation exchange capacity (CEC) that depends on the Ca/Si ratio of the C-S-H phases can be used. For instance, a model for cation exchange for a low-pH concrete (Idiart *et al.*, 2020) can be represented as

$$\begin{aligned} 2EX^- + Ca^{+2} &\leftrightarrow EX_2Ca, \\ 2EX^- + 2K^+ &\leftrightarrow EX_2K_2, \\ 2EX^- + 2Na^{+2} &\leftrightarrow EX_2Na_2, \end{aligned} \qquad [\ 4.3\ ]$$

with parameters given in Table 4.4. This type of cation exchange data can be directly incorporated into the chemical thermodynamic database to be used for the reactive transport simulations. However, these data have been only used for the shotcrete liner and cation exchange processes have not been considered for the other cement-based materials. It is worth mentioning that, if the CSHQ solid solution model is incorporated in the calculations, an extension of the ideal solid solution model (available in CEMDATA v18.1) that includes Na and K uptake shall be used instead of cation exchange reactions.

Table 4.4. Cation exchanger compositions of cementitious materials (adapted from Idiart et al.*, 2020).*

Exchanger species	**Log K**	**mol/kg water**
EX_2Ca	0	4.444×10^{-01}
EX_2K_2	0.37	5.524×10^{-01}
EX_2Na_2	0.37	1.689×10^{-01}
Total (CEC)		2.331

In addition to the mineral constitution of each material, secondary phases not initially present in the system but likely to form need to be incorporated into the model. These include different minerals such as, for instance, brucite ($Mg(OH)_2$), which is likely to form from the reaction between Mg and Ca-rich minerals. Other Fe-bearing minerals, such as magnetite, are allowed to form as well. Also, M-S-H phases, which do not form during cement hydration in any of the cementitious materials, are included as secondary minerals. All considered secondary phases are enlisted in Table 4.7.

4.5.3.1. Functional concrete walls

The equilibrated concrete porewater results in a highly alkaline pH (13.45) due to the significant concentrations of Na and K, with a pe of -7.2 and an ionic strength of 0.3904 m. On the other hand, the low concentrations of dissolved Mg and Fe create a steep concentration gradient due to the corresponding concentrations coming from the clay rock porewater. Dissolved Sr is only present in the clay porewater due to the presence of celestite; however, a low concentration of Sr in all cementitious materials is set (1×10^{-10} mol/L) to facilitate the convergence of the numerical algorithm. Calcite and portlandite are the main minerals in the fully hydrated concrete. In minor amounts, the formation of ettringite, monocarbonate and hydrotalcite are observed. The C-S-H solid solution assemblage shows more significant amounts of the JenD (Ca/Si = 2.25) and TobD (Ca/Si = 1.25) end members. The resulting porosity of the cementitious material is estimated by the change of volume fractions in the fully equilibrated concrete and is equal to 0.085.

4.5.3.2. Waste package backfill mortar

See section 4.5.3.3

4.5.3.3. Vault backfill mortar

The vault backfill mortar porewater is more similar to the concrete walls in terms of pH (13.09), pe (-6.8) and ionic strength (0.16 m). One significant difference, however, is caused by the significantly higher water/binder ratio (1.25) than that of the functional concrete (see Table 4.3). The reason for this high w/b ratio is to obtain a highly porous material (porosity = 0.29). The mineralogical composition is also similar to the functional concrete; the mortar has high proportions of portlandite and the C-S-H phases assemblage shows higher amounts of the JenD and TobD end members.

4.5.3.4. Shotcrete liner

The low-pH shotcrete is a fundamental part of the geochemical evolution of the disposal cell because it is in direct contact with the porewater of the clay rock. Early chemical interactions will be driven by the shotcrete-clay interface mainly because of the diffusion of an alkaline plume from the shotcrete to the clay. The hydration of the shotcrete liner results in a pH = 10.51. The main difference of the shotcrete with respect to the other cementitious materials is the addition of a high ratio of silica fume as binder (simplified as SiO_2, see Table 4.3). In contrast to the waste package backfill mortar, the water/binder ratio is much higher, which produces a higher porosity (0.24). The C-S-H assemblage is also quite different from the previous materials, favouring the formation of the TobH (Ca/Si = 0.67), which significantly smaller amounts of JenD, JenH and TobD end members. Furthermore, due to the suppression of some zeolites and thaumasite (which form if allowed), quartz does not react completely after full equilibration. In the reactive transport model, the remaining amount of quartz can be treated with an irreversible dissolution reaction, avoiding the need to incorporate dissolution kinetics into the model. Other minerals, such as hydrotalcite, straetlingite and FeOOH(mic), also form during hydration.

4.5.3.5. Clay host rock and EDZ

The equilibrated porewater and mineralogical composition of the Callovo-Oxfordian clay rock is taken from previously reported data (Marty *et al.*, 2014). Mineralogical proportions are different for the EDZ and the host rock because of the increased porosity in the EDZ. The pH of the clay rock is almost neutral (7.06), causing a strong interaction with the cementitious materials in the disposal cell. It has been reported that some clay minerals dissolve kinetically (i.e., “Illite_Imt-2”, “Montmorillonite-BCCa”, “Microcline” and “Ripidolite_Cca-2”). However, as previously mentioned, this is suppressed from the reactive transport model in favour of thermodynamically controlled reactions. In addition, these reactions are restricted to irreversible dissolution in the geochemical algorithm. Quartz is also known to precipitate kinetically, but this reaction may be modelled as reversible to avoid numerical problems (i.e., the majority of quartz precipitates at the cement-clay interface with small amounts of dissolution) as long as the overall evolution favours the precipitation of quartz at the cement-clay interface.

Surface chemical processes are modelled as cation exchange reactions in the clay rock (**Erreur ! Source du renvoi introuvable.**). It is assumed that the composition of the exchangers is in equilibrium with the initial porewater solutions. In the EDZ and clay rock, the cation exchange reactions consider Ca, Fe, K, Mg, Na and Sr (Marty *et al.*, 2014).

Surface complexation reactions are incorporated for pH buffering in the clay subdomain. For instance, surface complexation considering the clay mineral illite can be modelled as follows (Bradbury and Baeyens, 2005a):

$$\begin{aligned} &\equiv Ill^w\text{-}OH + H^+ \leftrightarrow \equiv Ill^w\text{-}OH_2^+, && log\,K = 4.59, \\ &\equiv Ill^w\text{-}OH \leftrightarrow \equiv Ill^w\text{-}O^- + H^+, && log\,K = -7.11, \\ &\equiv Ill^s\text{-}OH + H^+ \leftrightarrow \equiv Ill^s\text{-}OH_2^+, && log\,K = 4.90, \\ &\equiv Ill^s\text{-}OH \leftrightarrow \equiv Ill^w\text{-}O^- + H^+, && log\,K = -6.80, \end{aligned} \qquad [\ 4.4\ ]$$

where $\equiv Ill^w$ and $\equiv Ill^s$ are weak and strong sites, respectively. The surface specific area is 100 m^2/g with a surface site density of 2.31 sites/nm^2. Additional data for illite, as well as montmorillonite, is available from previous studies (Bradbury and Baeyens, 2005b; Marques *et al.*, 2012).

Table 4.5. Cation exchange reactions of the EDZ and clay rock in the ILW disposal cell (adapted from Marty et al.*, 2014).*

Exchanger	Log K	mol/kg water

COx_2Ca	0.7	4.744×10^{-01}
COx_2Mg	0.7	3.282×10^{-01}
COxNa	0	3.867×10^{-01}
COxK	1.2	7.850×10^{-02}
COx_2Sr	0.6	1.188×10^{-02}
COx_2Fe	0.8	2.860×10^{-03}
Total (CEC)		2.1

4.5.4. Chemical thermodynamic database

Due to the large amount of cementitious materials present in the ILW cell studied here, the latest version of CEMDATA which refers to CEMDATA18 (Lothenbach et al., 2019) (https://www.empa.ch/cemdata) will be used. This database contains updated thermodynamic data for common cement hydrates on ordinary Portland cement and alkali-activated materials such as C-S-H, AFm and AFt phases, hydrogarnet, hydrotalcite, zeolites, and M-S-H phases. The database contains updated data for several ferric iron bearing AFm and AFt phases, hydrogarnet, and hydrotalcite phase. The database is available for GEM-Selektor (Kulik et al., 2013) and PHREEQC (Parkhurst and Appelo, 2013) formats and is thus compatible with the format needed for OpenGeoSys, the code used for modelling the ILW cell evolution.

The stability constants for the cement phases were obtained by recalculating the experimental data using the PSI/Nagra 12/07 (Hummel et al., 2002; Thoenen et al., 2014) as a source for the aqueous species, gas and other solid components participating in the reactions. This makes CEMDATA18 fully compatible with the PSI/Nagra 12/07 chemical thermodynamic database. For the GEM-Selektor geochemical modeling software, which uses the Gibbs energy of all species in phases to calculate equilibrium, the Gibbs energy of formation for all CEMDATA18 components were calculated based on their reported logK's (Lothenbach et al., 2019) and reactants from the PSI/Nagra 12/07. Some additional data for solid phases (e.g. carbonates, Al hydroxides, Fe oxides, hydroxides, sulfides, etc.) relevant for cementitious systems, distributed with CEMDATA18, are also from the PSI/Nagra 12/07. Solid solution models (a solid solution is a solid phase that can be described as a mixture of two or more solid species (constituents, endmembers).) for AFm, AFt, C-S-H, and M-S-H are also included in the CEMDATA18 database GEM-Selektor version (Kulik et al. 2013). For C-S-H, several alternative solid solution models are available. Non-ideal binary Redlich-Kister (Guggenheim) (Glynn, 2019) solid solution models are used for: (Al, Fe)-ettringite, (Al, Fe)-monosulfate, (SO_4, OH)-monosulfate, and (SO_4, OH)-ettringite. (Al, Fe)-siliceous hydrogarnet, C-S-H, M-S-H, hydrotalcite-pyroaurite, (Mg, Al)-hydrotalcite, straetlingite and ettringite (for different water content) are treated as ideal solid solutions.

CEMDATA18 is also available in LMA (Law of Mass Action) setup that requires thermodynamic data in the form of log K values for both aqueous complexes and solids. The database has been written into PHREEQC "dat" format (Miron et al., 2018). The PHREEQC version of the database contains all the reactions for the cementitious components and the related subset of general thermodynamic data (mainly aqueous species) from the PSI-Nagra TDB needed for the reactions. The PHREEQC version of the CEMDATA18 can also be used at elevated temperatures, 0 - 100 ℃. The coefficients for the logK = f(T) were calculated from the available data on the entropy and heat capacity effect of the reactions. To use solid solutions in PHREEQC, these must be defined by the user in the input script calculation file using the endmember names from the database.

When using the CEMDATA18 database for equilibrium calculations, based on their thermodynamic data alone, some phases are more stable than others, but they might not form during the timescale of the modelled process. For example, the Fe-containing AFm and AFt hydrates have a limited stability field due to the high stability of goethite (FeOOH) and hematite (Fe_2O_3). The latter should to be suppressed

when doing calculations at ambient conditions in favour of microcrystalline FeOOH (or microcrystalline or amorphous $Fe(OH)_3$), but should be allowed to form at elevated temperatures (> 50°C) or when considering very long time scales. Similarly, the formation of gibbsite ($Al(OH)_3$) and quartz (SiO_2) should be suppressed in favour of microcrystalline or amorphous $Al(OH)_3$, and amorphous SiO_2.

4.5.4.1. PSI/Nagra database

The PSI/Nagra thermodynamic database contains data to support modelling geochemical processes related to low- and intermediate-level and to high-level radioactive waste (conditions in Switzerland). The initial database was issued in 1992 (Pearson et al., 1992; Pearson and Berner, 1991) and was later followed by two major updates, Nagra/PSI Chemical Thermodynamic Data Base 01/01 (TDB 01/01) (Hummel et al., 2002) and PSI/Nagra Chemical Thermodynamic Data Base 12/07 (TDB 12/07) (Thoenen et al., 2014). The data selection is based on detailed in-house reviews and on the OECD NEA's book series on "Chemical Thermodynamics". The current version of the PSI/Nagra Chemical Thermodynamic Data Base is 12/07 (TDB 12/07) (Thoenen et al., 2014). A new version of the database (PSI Chemical Thermodynamic Database 2020) with updated thermodynamic data is under development. The critically selected data is classified into core data, based on the CODATA key values (Cox et al., 1989), recommended application data, with well-characterized aqueous species, minerals, and gases, and supplemental data, with less well-characterized uncertain data suitable for scoping and qualitative calculations (for cases where omission of data even if uncertain would lead to unacceptable results).

The PSI/Nagra database is available both in GEM-Selektor (Kulik et al., 2013) and in PHREEQC (Parkhurst and Appelo, 2013) format. The PHREEQC version of the database contains data for reference temperature (25°C) and pressure (1 bar). In the GEM-Selektor version the data for aqueous species was augmented with parameters for the HKF (Helgeson-Kirkham-Flowers) equation of state (Tanger and Helgeson, 1988) taken from the SUPCRT slop98 database (Johnson et al., 1992). These allow the extrapolation of their properties at different temperatures and pressures. For solid phases additional data on the heat capacity temperature function is provided with coefficients collected from Robie and Hemingway (1995) and Helgeson et al. (1978). Some of the components are defined using reaction data, as reaction dependent components. In this case, depending on the available data on the entropy and heat capacity effects of reaction, the three-term, two-term or constant logK, extrapolation methods are used for calculating the logK values as a function of temperature.

The thermodynamic data for iron in the PSI/Nagra Chemical Thermodynamic Data Base 12/07 (TDB 12/07) were accepted from the section of Hummel et al. (2002), Nagra/PSI Chemical Thermodynamic Data Base 01/01 (TDB 01/01). Most of the iron data come from the original selection by Pearson, in the Nagra Thermochemical Data Base 05/92 (TDB 05/92). Pearson selected data from Wagman (1982) (properties of formation of the master species Fe^{2+}) and from Nordstrom et al. (1990) and Baes and Mesmer (1977) (inorganic complexes of iron and iron solids). The database was further enhanced with the addition of data for hematite, magnetite, pyrite, and troilite by Hummel et al. (2002).

A major revision on the data for iron is in progress (PSI Chemical Thermodynamic Database 2020). This revision concerns most of the iron aqueous species and iron bearing solid phases in the PSI/Nagra database. The new data selection is based mainly on the recent OECD NEA's volume on the thermodynamics of iron by Lemire et al. (Lemire et al., 2013).

4.5.4.2. Other databases (Thermoddem and ThermoChimie)

Thermoddem is a database for the thermodynamic properties of interest for hazardous and radioactive wastes, as well as the geochemistry of natural environments (Blanc et al., 2012). The database is developed by the French geological survey (https://thermoddem.brgm.fr). The last qualified version of Thermoddem (V1.10, 2017) is formatted for several reactive transport models including CRUNCH, HYTEC, PHREEQC or THOUGHREACT. An update version (V1.10, 2019) is under progress.

Thermoddem is applicable to the full pH range, including the high-pH alkaline domain, from 0 to 100°C. The database includes a large set of zeolites and cementitious phases with a broad composition range with respect to concrete formulae such as CEM I and low-pH cements. The C-A-S-H, C-S-H and M-S-H phases are introduced as discrete elements. A few iron-bearing cement phases are present such Fe-AFm and Fe-AFt. Thermoddem is also suitable for modelling iron corrosion products such as iron carbonates, oxyhydroxides, silicates and sulfides.

Additional data for iron corrosion products or clay phases can be selected from ThermoChimie, which is the thermodynamic database developed by ANDRA, ONDRAF and RWM for the performance assessment of the geologic disposal of radioactive waste (Giffaut et al., 2014, https://www.thermochimie-tdb.com). ThermoChimie provides formation constants (at temperatures ≤ 80°C) for a wide range of radionuclides and the mineral component of multi-barrier systems, including host-rock solid phases, bentonites, cements, steel, and their evolving secondary phases. The database is formatted for several reactive transport models including HYTEC.

4.5.5. Microbiological parameters

Based on the broad range of environments in which microorganisms can survive, including extreme conditions as high pH, radiation, low substrate concentrations or even low porosities, the presence of microorganisms in the waste and the near field of a L/ILW repositories could not be discard. In fact, numerous studies in natural and engineered systems have demonstrated that microbial life is possible under extreme natural conditions, although it is difficult, with current techniques, to determine whether microbial cells are merely surviving or are in fact active and multiplying at very low rates.

With all these constraints and lack of information, microbial parameters will not be considered in the disposal cell models of ACED. However, qualitative assessment will be considered if relevant information is obtained within the EURAD-MAGIC project to be started in June 2021.

4.5.6. Summary of initial porewater compositions and solution properties

Table 4.6 shows the equilibrated porewater compositions of each material in the disposal cell concept. A pre-equilibration step to validate the transfer of information between codes (GEMS-Phreeqc) from cement hydration and databases (CEMDATA v18.1 and ThermoChimie) has been carried out. Concentrations equal to zero are set to 1×10^{-10} mol/L to avoid numerical problems during the simulation. The redox of the cement-based materials were obtained in the hydration model by initially fixing a partial pressure of -12.6 for hydrogen in order to have reducing conditions in the limit range of water stability, pe + pH = 0 (Neck et al. 2007)

Table 4.6. Porewater initial concentrations of different materials in the ILW disposal cell.

Component [mol/L]	Functional concrete	Waste package mortar	Vault backfill mortar	Shotcrete liner	Clay rock
Al	8.20E-05	3.30E-05	3.30E-05	3.71E-04	8.50E-08
C(4)	2.06E-04	3.33E-05	3.33E-05	2.05E-05	3.83E-03
Ca	9.59E-04	2.65E-03	2.65E-03	5.61E-03	7.60E-03
Cl	5.51E-07	1.95E-07	1.95E-07	8.44E-08	4.12E-02
Fe	1.23E-07	4.98E-08	4.98E-08	1.08E-09	4.35E-05
K	4.11E-01	1.53E-01	1.53E-01	9.67E-02	5.11E-04
Mg	1.33E-09	2.94E-09	2.94E-09	7.43E-07	5.19E-03
Na	7.53E-03	9.13E-03	9.13E-03	3.96E-03	4.01E-02
S(6)	5.08E-03	5.54E-04	5.54E-04	5.49E-02	1.11E-02
Si	7.56E-05	3.79E-05	3.79E-05	1.41E-03	1.80E-04
Sr	1.00E-10	1.00E-10	1.00E-10	1.00E-10	2.43E-04
pH	13.45	13.09	13.09	10.508	7.06
pe	-7.2	-6.8	-6.8	-4.5	-2.84

4.5.7. Summary of initial solid composition and secondary phases

A summary of all the primary minerals in the cementitious materials and the clay rock, as well as secondary phases are shown in Table 4.7. Solid phases are divided in initial and secondary ones. Initial phases are present at least in one material, whereas secondary phases are not present initially in any of the materials, but are allowed to precipitate if the solution becomes supersaturated. Note that the notation of CEMDATA v18.1 is used (except for clay minerals).

Thermodynamic data for primary clay minerals denoted as “Illite_Imt-2”, “Montmorillonite-BCCa”, “Microcline” and “Ripidolite_Cca-2” is taken from ThermoChimie v10a (the latest version). In addition, secondary minerals not found in CEMDATA are also added from ThermoChimie (Pyrrhotite, Fe(OH)2(cr) and Saponite-FeCa). The thermodynamic data for the remaining minerals is taken from CEMDATA v18.1.

Table 4.7. Initial solid composition of the ILW disposal cell materials.

Mineral [mol/kg water]	Functional concrete	Waste package mortar	Vault backfill mortar	Shotcrete liner	EDZ	Intact clay rock
CSHQ-JenD	7.7366	1.5092	1.5092	0.0006	0	0
CSHQ-JenH	4.9492	0.9835	0.9835	0.1140	0	0
CSHQ-TobD	5.8155	1.1345	1.1345	0.6910	0	0
CSHQ-TobH	0.2448	0.0486	0.0486	9.1747	0	0
KSiOH	1.6913	0.1340	0.1340	0.1456	0	0
NaSiOH	0.2897	0.0420	0.0420	0.0389	0	0

ettringite	0.6240	0.1207	0.1207	0.0842	0	0
monocarbonate	1.0813	0.2092	0.2092	0	0	0
Cal (Calcite)	23.2464	0.2445	0.2445	0.3489	25.1900	27.9900
C3FS0.84H4.32	0.7546	0.1460	0.1460	0	0	0
Portlandite	19.4340	3.6971	3.6971	0	0	0
hydrotalcite	0.4246	0.0822	0.0822	0.0636	0	0
straetlingite	0	0	0	0.1842	0	0
FeOOHmic	0	0	0	0.2246	0	0
Qtz (Quartz)	0	0	0	0.3724	45.7740	50.8600
Cls (Celestite)	0	0	0	0	0.6210	0.6900
Ord-Dol (Dolomite)	0	0	0	0	2.4840	2.7600
Py (Pyrite)	0	0	0	0	0.9540	1.0600
Sd (Siderite)	0	0	0	0	0.9900	1.1000
Illite_Imt-2*	0	0	0	0	9.6930	10.7700
Montmorillonite-BCCa*	0	0	0	0	2.4750	2.7500
Microcline*	0	0	0	0	1.2330	1.3700
Ripidolite_Cca-2*	0	0	0	0	0.3690	0.4100
Amor-Sl	0	0	0	0	0	0
Brc (Brucite)	0	0	0	0	0	0
C3AH6	0	0	0	0	0	0
C3FH6	0	0	0	0	0	0
C4AH13	0	0	0	0	0	0
C4FH13	0	0	0	0	0	0
Gp (Gypsum)	0	0	0	0	0	0
hemicarbonate	0	0	0	0	0	0
Mag (Magnetite)	0	0	0	0	0	0
Fe-monosulphate	0	0	0	0	0	0
monosulphate12	0	0	0	0	0	0
M075SH	0	0	0	0	0	0
M15SH	0	0	0	0	0	0
Fe-ettringite	0	0	0	0	0	0
syngenite	0	0	0	0	0	0
Pyrrhotite*	0	0	0	0	0	0
Fe(OH)2(cr)*	0	0	0	0	0	0
Saponite-FeCa*	0	0	0	0	0	0

*Phase names are as given in the ThermoChimie thermodynamic database for Callovo-Oxfordian. Clay minerals Illite_Imt-2, Montmorillonite-BCCa, Microcline and Ripidolite_Cca-2 are restricted to irreversible dissolution in the reactive transport simulations.

It is worth noting that inert quartz is considered as an aggregate in all cementitious materials. Therefore, the solid constitution of the cementitious materials only accounts for reactive solids, where aggregates are considered for the calculation of physical properties only (e.g., porosity).

4.6. Expected outcomes

The expected outcomes of the presented conceptual and numerical model of the ILW disposal cell in clay will focus on the time evolution of selected parameters at specific locations and the spatial distribution at different times of:

1) The computed pH and redox at the different materials and interfaces.
2) The computed concentrations of the dissolved chemical species at the different materials and interfaces.
3) The computed concentrations of precipitated mineral phases at the different materials and interfaces.
4) The computed volume fractions of the mineral phases at the different materials and interfaces.
5) The computed changes in porosity at the different materials and interfaces.
6) The computed gas generation (H_2, CH_4, CO_2) and consumption at the different materials and interfaces.
7) The computed saturation of the systems.

In addition, it is expected that the results obtained with the simulations will lead to an improved understanding of the chemical evolution of the cementitious materials in the disposal cell and their interaction with the clay rock. Analysis of the outcomes will include the description of the main processes that influence cement degradation and the interplay occurring among each material, as well as the impact over the clay rock. It is also worth mentioning that additional outcomes can be included at later stages of the project.

The resulting complexity of this model of the ACED Subtask 4.1 and the associated numerical limitations can serve as triggers for new developments in the WP Modelling or for abstraction methodologies in ACED Subtask 4.2. The complex model will subsequently be redefined (if needed) based on the current capabilities of the numerical tool used in this case (OpenGeoSys). Then, the implementation in OpenGeoSys, using the highest level of complexity as possible and interpretation of the results follows. In a second step, an update of the model is foreseen based on the knowledge gained in Tasks 2 and 3 of ACED and other EURAD WPs and the numerical methods/tools in the DONUT WP or the knowledge generated in CORI WP (Cement-Organics-Radionuclide-Interactions). This two-step approach guarantees an early start of Tasks 4.2 and 4.3.

4.7. Computer code

OpenGeoSys (OGS) is a scientific open-source initiative for the numerical simulation of thermo-hydro-mechanical/chemical (THMC) processes in porous and fractured media which will be used to model both ILW disposal cells. The basic concept of OGS consist on providing a flexible numerical framework, using primarily the Finite Element Method (FEM) for solving multi-field coupled processes with application in different scientific and technical disciplines. For example, OGS has been successfully applied in the fields of regional, contaminant and coastal hydrology (Nixdorf et al., 2017, Walther et al., 2017, Jing et al., 2018, 2019), fundamental and geothermal energy systems (Chen et al., 2019, Parisio et al., 2019a, 2019b, Meng et al., 2018, 2019; Hein et al., 2016), geotechnical engineering (Zhu et al., 2020), energy storage (Miao et al., 2019, Lehmann et al., 2019, Böttcher et al., 2017; Nagel et al., 2017; Pfeiffer et al., 2016), CO_2 sequestration/storage(Grunwald et al., 2020, Liu et al., 2019, Li et al., 2014, Beyer et al., 2012) and nuclear waste management and disposal (Shao et al., 2019a, 2019b).

Since the mid-eighties (Kolditz, 1990, Wollrath, 1990, Kroehn, 1991 and Helmig, 1993) OpenGeoSys is in continuous development evolving through Fortran, C, and C^{++} implementation with the current released version being OpenGeoSys 6.3. (Naumov et al., 2020). OpenGeoSys-6 (Naumov et al., 2018, Bilke et al., 2019) is a complete re-implementation of OpenGeoSys 5 (Kolditz et al., 2004; Wang and Kolditz, 2006; Kolditz et al., 2012) which uses advanced methods in software engineering and architecture with focus on code quality, modularity, performance and comprehensive documentation. Till the present moment, particular emphasis has been placed on the implementation of advanced

numerical methods for simulating propagation of discontinuities, such as enriched finite element function spaces (Watanabe et al., 2012), non-local formulations (Parisio et al., 2018) and phase-field models (Lepillier et al., 2020, Yoshioka et al., 2019, 2020). As in the previous version, OGS-6 is taking advantage of High Performance Computing (HPC) platforms on both MPI and OpenMP concepts to analyse realistic complex geosystems (Fischer et al., 2019, Wang et al., 2015, 2017).

Regarding reactive transport processes which is the coupled processes which will be studied in this work, different approximations have been implemented in OGS along its development in order to consider multicomponent mass transport and bio/geochemical reactions (Chen et al., 2020, Boog et al., 2020, 2019, Yapparova et al., 2019). For example, Ballarini et al. (2014) used an internal OGS library to simulate kinetically controlled biogeochemical reactions. In other cases, OGS has been coupled in a sequential non-iterative approach with well-known external geochemical solvers (i.e. PHREEQC, GEMS, BRNS and ChemApp). The coupling of these codes are referred as OGS-PHREEQC (Xie et al., 2006, He et al., 2015), OGS-GEM (Kosakowski and Watanabe, 2014), OGS-BRNS (Centler et al., 2010) and OGS-ChemApp (Beyer et al., 2012, Li et al. 2014). Very recently, an alternative coupling solution of reactive transport has been developed and implemented by approximating the complex chemical reactions into a quickly calculating look-up table (Aguila et al., 2021, Huang et al., 2018). The novel implementation provides fast and efficient simulations, a feature especially relevant for long-term simulations. Reactive transport calculations referred above have been mainly performed with OGS-5, although OGS-6-iPHREEQC version is already released (Naumov et al., 2020). This new version includes a new implementation with direct memory access which allows efficient computational simulations. Application of OGS on reactive transport modelling in the framework of nuclear waste disposal includes long term cementitious materials/clay interactions (Idiart et al., 2020, Kosakowski et al., 2014, Kosakowski and Berner, 2013, Berner et al., 2013, Shao et al., 2013), laboratory scale precipitation/dissolution processes in combination with density driven flow and clogging effects (Poonoosamy et al., 2020, 2018, 2015) and with mechanical processes (Lu et al., 2018), concrete degradation due to reactive aggregates in combination with multi-phase transport of CO_2 (Huang et al., 2018) and radionuclide migration in clays (Aguila et al., 2021). Recently the look up table approach has also been applied to model gas and humidity transport in combination with concrete/ organic matter degradation and corrosion of metals in a waste package during 100 years of intermediate storage (Kosakowski and Huang, 2019, Huang et al., 2021)).

Finally, OpenGeoSys is participating in several international model development, validation and benchmarking initiatives, e.g., DEVOVALEX (with applications mainly in the assessment of nuclear waste repositories (Birkholzer et al., 2018), CO_2BENCH (Kolditz et al., 2012b), SeS Bench (Steefel et al., 2015) and HM-Intercomp (Maxwell et al., 2015) providing ongoing series of benchmark books (Lehmann et al., 2018) and tutorials (Jang et al., 2017). For more information please refer to the OpenGeoSys webpage (www.opengeosys.org).

4.8. Summary

The contribution of Subtask 4.1 to the ILW disposal cell in a clay sedimentary formation is based on a generic concepts and design defined for building up a repository in indurated clay rocks like Opalinus Clay and Callovo Oxfordian. However, the defined multibarrier system (i.e waste matrix, containers, backfill material) is also common for other concepts where plastic clays are considered (i.e. Boom Clay). Specifically, the studied disposal concept is based on a multi-barrier system including the waste matrix (in the primary coli or drum), the disposal container, the mortar backfill in the emplacement tunnel and the clay host rock (Callovo Oxfordian). Reinforced of the tunnels walls with a shotcrete is also part of the concept. It is assumed that the disposal cell contains a number of stacked waste containers (with organic or metallic waste). In addition, a backfilling material between the waste containers is considered and in the case of the organic waste, 6 different waste packages are also inside the containers. The dimensions of the multibarrier system are 11 x 13 m without including the host rock and the EDZ. Hydration models for the four different CEM I cementitious materials (i.e. functional concrete walls of

the containers, backfill mortar between the waste containers, vault backill mortar and shotcrete liner) have been performed to determine the initial hydrated cement phases in the reactive transport model. All the materials have been conceptualized as homogeneous porous media. Diffusion is the main transport mechanism and no temperature effects has been considered. Aqueous complexation reactions, mineral dissolution/precipitation reactions, cation exchange and surface complexation reactions are part of the model. When considering changes of porosity due to precipitation/dissolution of minerals, standard molar volumes are used. All this information is contained in the same chemical thermodynamic database, CEMDATA v18.1. Additional thermodynamic data for some clay minerals not found in CEMDATA is retrieved and adapted to match the same master species of CEMDATA from the latest version of the ThermoChimie database. Simulations will be for 100 000 years and will be performed with the T-H-M-C code OpenGeoSys v.6.

5. Conceptual, mathematical and numerical models, and numerical tools of the ILW disposal cell in granite

5.1. Description of the disposal cell concept

The generic configuration of the ILW disposal cell concept in granitic host rock is presented in Figure 5.1. The domain under consideration includes:

1) Waste zone with two types of waste packages
    a. Metallic waste;
    b. Organic waste.
2) Cementitious backfill.
3) Granitic host rock.

The tunnel width is 11 m and the height is 13 m. In addition, several meters of the host rock should be considered in the model.

Multibarrier system (11 x 13 m) + host rock:

- Host-rock (Spanish Granitic rock)
- ~~EDZ (excavation damage zone)~~
- ~~Liner (shotcrete)~~
- Backfill material (mortar)
- Waste region (metallic / organic waste)

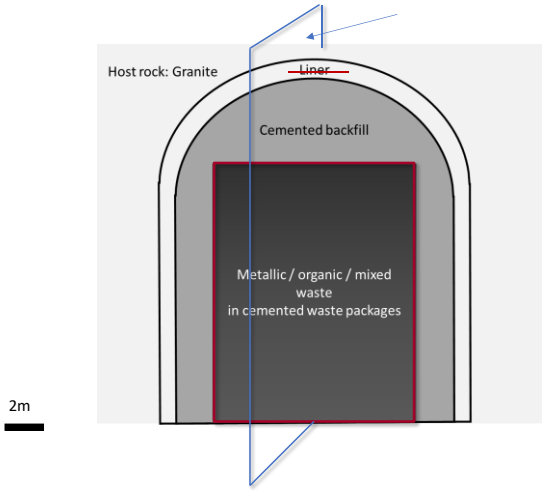

Figure 5.1. Layout of the representative ILW disposal cell concept in a granitic host rock. Note: The EDZ and the liner considered in the ILW clay disposal cell are not part of the disposal ILW cell in crystalline rock.

A more detailed representation of the waste zone is provided in Figure 5.3. It is assumed that the waste zone contains three rows of containers: two rows with organic waste packages and a row of metallic waste packages in between.

It was mentioned in the discussions during ACED WP meeting that one of the options could be Nirex Reference Vault Backfill (NRVB) considered in the UK concept. However, the first option will be to use the same backfill material described in Chapter 4 and the NRVB will be consider only as sensitive case.

As regards granitic host rock, Spanish granite was proposed and its characteristics were provided in Chapter 2 (Samper et al., 2008).

According to the disposal cell in granitic rock layout (Figure 2.1), the dimensions of the multibarrier system are 11 x 13 m plus host rock. In order to keep up with similar model dimensions between the different host rock concepts for ILW (i.e. clay and crystalline rock), the disposal cell in the clay rock, presented during ACED meeting (January 2021, see Figure 2.2), is taken as an example without considering the EDZ and the liner.

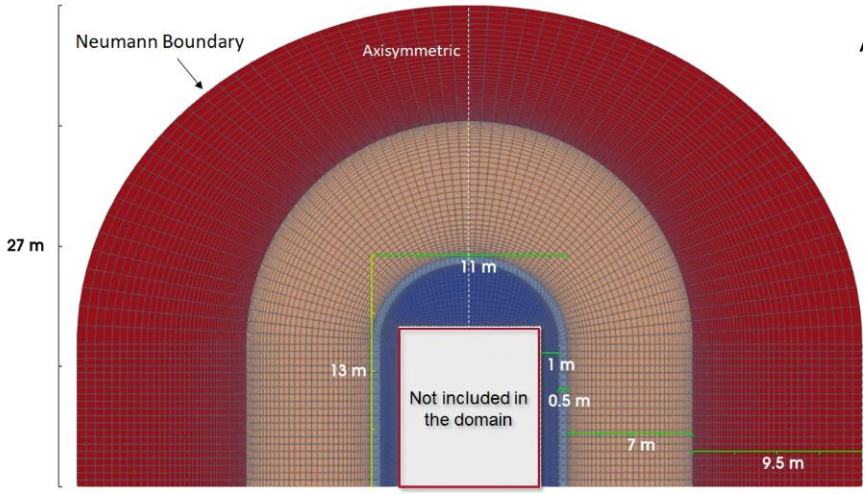

Figure 5.2. *Layout of the representative ILW disposal cell concept in a clay host rock. In dark blue: backfill material, light blue: liner, brown: EDZ, red: host rock*

According to the layout of the ILW disposal cell concept in a clay host rock (see Chapter 4 for more details), the waste zone is surrounded by backfill of 1 m thickness from both sides and somewhat higher thickness on the top. In addition, about 10 m of the host rock around the tunnel is considered. Based on this information, it is assumed that the thickness of the backfill at both sides of the waste zone is 1 m and the thickness of the backfill on the top is 2 m. Taking into account that emplacement dimensions are 11 x 13 m (L x H), the dimensions of the waste zone are assumed to be 9 x 11 m (L x H). 10 m of the granitic host rock around the backfill is also included.

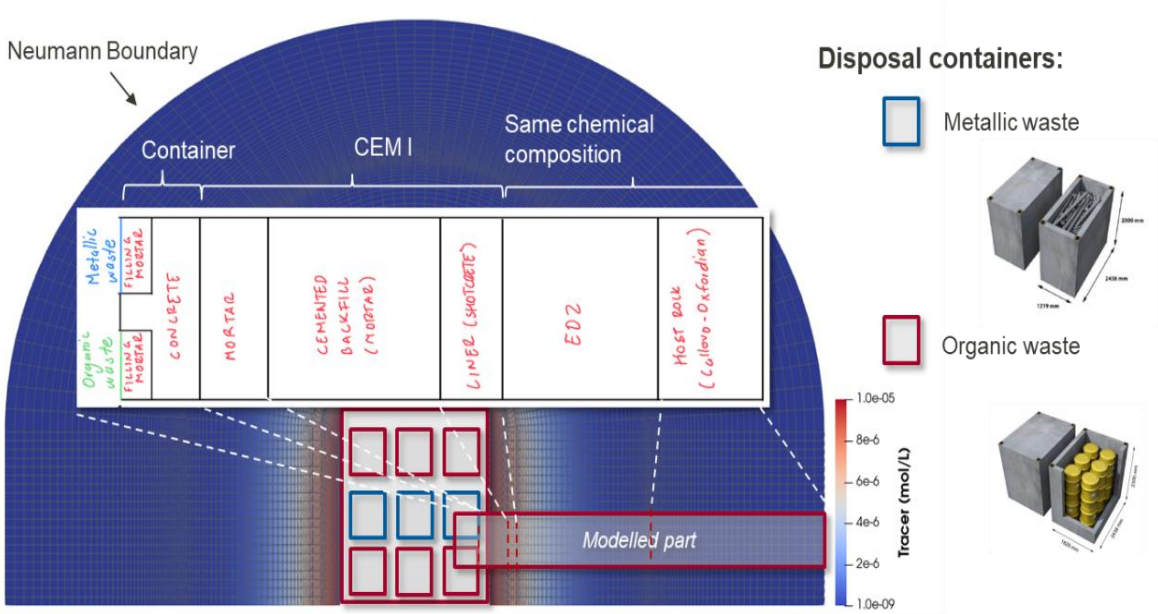

Figure 5.3. Waste zone (as presented in ACED meeting, January 2021).

5.2. Conceptual Model

The conceptual model used in the granitic system is very similar to the concept used in clay (see Section 4.2). Differences are only related to the hydrodynamic processes which are explained in Section 5.2.1 and the groundwater composition of the granitic rock which could induce different chemical reactions.

5.2.1. Hydrodynamic processes

The reactive transport model of the ILW disposal cell in granite assumes that the system is initially fully water-saturated. Advection and diffusion-dispersion processes for solute transport will be considered in the model. The changes in the permeability and transport parameters of the materials due to mineral dissolution/precipitation will not be considered initially. However porosity changes due to reactions will be consider as sensitivity case.

The groundwater flow is arbitrarily assumed to be horizontal from left to right. The water flow is imposed by setting different hydraulic head at the left and the right boundaries of the model domain. Water flow rate through the Spanish granite was defined based on data presented in Samper et al. (2008). It is assumed in the reactive transport model in Samper et al. (2008) that hydraulic gradient over 6.5 m distance is 0.55. Taking into account that the hydraulic conductivity of the Spanish granite is $8.72 \cdot 10^{-12}$ m/s (Table 5.5), the obtained water flow velocity is $7.38 \cdot 10^{-13}$ m/s. In order to represent such water flow velocity, the corresponding hydraulic head at the outflow (right boundary of the domain) is set to 0 m and at the left boundary – to 2.62 m. Such hydraulic gradient over a distance of 31 m (the distance between the left and the right boundaries) will produce the required water flow rate.

5.3. Mathematical model

Similar to the mathematical model described in Section 4.3, the model for the ILW in crystalline rock integrates multicomponent transport in porous media coupled with chemical reactions. Initially, the transport of solutes is assumed to take place under isothermal fully water-saturated media throughout the emplacement cavern. Solute transport will be mainly driven by the hydraulic gradients of the host rock. Equations are given in Section 4.3.

5.4. Parameter values

5.4.1. Waste zone

The region with metallic/organic waste packages (waste zone) will not be modelled explicitly. It is intended to represent it through application of appropriate boundary conditions on the waste zone outer perimeter as indicated by the red line in Figure 5.1. Differences compared to the ILW in clay is that the functional concrete wall and the waste package backfill mortar will not be considered in the ILW-crystalline in order to observe the influence of these domains in the system. After the first simulations, it will be decided if the walls of the container should be part of the system or should be excluded. In addition, it is expected that input for boundary conditions (e.g. H_2(g) flux) will be available from ACED WP Task 3, this information will not be initially considered (as it is not available yet) and a constant rate for H_2 will be used.

Therefore, two cases are under consideration at the present moment: in one case the waste zone is treated as inactive region while in the other case it is included in the model with the properties as presented in Table 5.1. In detail, the waste zone will be modelled as an empty space, initially filled with concrete (backfill) pore water. It is intended to include this void into the model but to assign transport properties that ensure that there are no practical resistances to flow or diffusion in this volume. Such an approach is adopted from the Swedish model presented in SKB Report (Höglund, 2014). Waste zone material properties assumed for the modelling are presented in Table 2.3.

Table 5.1. Waste zone material properties (based on *Höglund, 2014*).

Parameter	Value
Porosity (-)	1
Tortuosity (-)	1
Effective diffusion coefficient, D_e (m^2/s)	$1 \cdot 10^{-9}$
Hydraulic conductivity, K (m/s)	0.1

5.4.2. Backfill

The backfill material used in the disposal cell in clay will be used here as well. However, other backfill cementitious material with different porosity will be tested as sensitivity case. Therefore, for the sensitivity case it is assumed in the modelling that the space between the waste zone and the host rock is filled with NRVB backfill (UK concept). Such an assumption is made based on several reasons:

- NRVB was specifically developed as potential backfill for UK geologic radioactive waste disposal facility in a higher strength rock;
- UK concept was proposed as one of the potential backfill for ILW cell in granite during ACED T4 meeting;
- UK concept was previously used by LEI for modelling purposes;
- There is sufficient available information on NRVB physical and chemical properties (e.g. Wilson et al., 2017; 2018).

According to Wilson et al. (2017), the main safety functions assigned to NRVB are:

- Maintenance of alkaline conditions;
- Maintenance of the sorption capacity;
- Sufficient gas permeability
- Mechanical and dimensional stability and the ability for waste package retrieval, if required.

The flow properties of the NRVB are presented in Table 5.2.

Table 5.2. Flow properties of the NRVB (based on Wilson et al., *2017*).

Parameter	Value
Porosity (-)	0.55
Tortuosity (-)	0.87*
Effective diffusion coefficient, D_e (m^2/s)	$4.8 \cdot 10^{-10}$
Hydraulic conductivity, K (m/s)	$1 \cdot 10^{-9}$

*Derived value assuming diffusion coefficient in the free water as $1 \cdot 10^{-9}$ m^2/s.

NRVB comprises Ordinary Portland Cement (OPC) with a fine aggregate containing crushed limestone filler (primarily calcium carbonate) and hydrated lime (calcium hydroxide) (Wilson et al., 2018). Two potential compositions of NRVB after hydration, depending on the hydration conditions, were found in the literature when modelling NRVB evolution (Wilson et al., 2018; Wilson et al., 2017). In one case hydrogarnet is present in the solid phase assemblage while in the other case it is assumed that

monocarboaluminate and ettringite form in addition to portlandite, calcite and C-S-H gel. The latter solid phase assemblage correlates to findings reported by Vasconcelos et al. (2018), thus it was selected for modelling the chemical evolution of the ILW disposal cell in granitic rock within ACED. The assumed hydrated solid phase assemblage of the NRVB is presented in Table 5.3.

Table 5.3. Hydrated solid phase assemblage of the NRVB assumed in the model (based on Wilson et al., *2018*).

Solid phase	Formula	Composition	
		wt%	vol%
Portlandite	$Ca(OH)_2$	19.8	9.5
C-S-H		23.9	10.6
Jennite-type	$(CaO)_{1.6667}(SiO_2)(H_2O)_{2.1}$		9.6
Tobermorite-type	$(CaO)_{0.8333}(SiO_2)(H_2O)_{1.3333}$		1.0
Calcite	$CaCO_3$	38.2	15.2
Monocarboaluminate	$Ca_4Al_2(CO_3)(OH)_{12}\cdot 5H_2O$	12.6	6.3
Ettringite	$Ca_6Al_2(OH)_{12}(SO_4)_3\cdot 26\ H_2O$	5.5	3.3
Total solids		100	45.0
Porosity		0	55.0

Initial NRVB pore water composition, corresponding to the assumed solid phase assemblage (see Table 5.3) is taken from Wilson et al. (2018) and presented in Table 5.4. It was obtained by equilibrating primary solids with water that contains dissolved Na, K, Cl, Mg, S and I at concentrations measured in NRVB pore water.

Table 5.4. Initial NRVB pore water composition (based on Wilson et al., *2018*).

Component	Concentration (mol/kg)
Na	$1.93\cdot10^{-4}$
K	$6.50\cdot10^{-4}$
Mg	$2.03\cdot10^{-6}$
Ca	$1.88\cdot10^{-2}$
Al	$3.54\cdot10^{-5}$
C (TIC)	$7.76\cdot10^{-6}$
Si	$1.09\cdot10^{-6}$
SO_4^{2-}	$2.22\cdot10^{-5}$
Cl	$3.05\cdot10^{-6}$
I	$8.12\cdot10^{-7}$
pH of the solution is 12.47.	

5.4.3. Granitic host rock

The Spanish granite is used as a reference host rock for the ILW disposal cell in granite as agreed by ACED Task 4 partners. The granitic formation is selected to have a low fracture density, tectonic stability and low seismicity. Physical, flow and solute transport parameters of the Spanish granite are provided in Table 5.5. Values are very similar to those used in Chapter 2, except for the temperature effects. The

granitic rock will be treated as an equivalent porous medium in the model with a uniform distribution of hydraulic conductivity and porosity.

Table 5.5. Physical, flow and solute transport parameters of the Spanish granite (Samper et al., *2008*).

Parameter	Value
Porosity (-)	0.005
Tortuosity (-)	0.01*
Effective diffusion coefficient, D_e (m^2/s)	$5.02 \cdot 10^{-14}$
Hydraulic conductivity, K (m/s)	$8.72 \cdot 10^{-12}$

*Derived value assuming diffusion coefficient in the free water as $1 \cdot 10^{-9}$ m^2/s.

The chemical composition of the granite boundary water is the same described in Table 2.5. It will be assumed that granite is an inert material, however, secondary minerals are planned to be allowed to precipitate and re-dissolve as the chemical conditions progress.

5.5. Expected outcomes

The expected outcomes are analogs to the one described in Section 4.6.

5.6. Computer code

OpenGeoSys (OGS) will be used for the ILW in crystalline rock. For more details about the code, see Section 4.7.

5.7. Summary

The contribution of Subtask 4.1 to the ILW disposal cell in a crystalline rock is based on the concepts and design available in Finland, Sweden, UK and Lithuania. The same multibarrier system considered for the ILW disposal cell in clay is used here except the host rock. In this case the Spanish granitic rock is considered and not EDZ is present. Advective flow from the host rock is considered and no temperature effects has been considered. Aqueous complexation reactions, mineral dissolution/precipitation reactions, cation exchange and surface complexation reactions are part of the model. When considering changes of porosity due to precipitation/dissolution of minerals, standard molar volumes are used. All this information is contained in the same chemical thermodynamic database, CEMDATA v18.1. Simulations will be for 100 000 years and will be performed with the T-H-M-C code OpenGeoSys v.6.

6. Integration, communalities and differences from HLW and ILW reference concepts

This section presents the integration, communalities and differences from the HLW and ILW disposal cell in granite and clay.

The generic configuration of the HLW disposal cell concept in granite and clay is similar. Both reference concepts share the following materials: (1) The vitrified waste (40 cm in diameter) which is explicitly considered in the reactive transport model and is coupled with the rest of the engineered barrier components; and (2) The overpack (5 cm thick) which is a low alloy carbon-steel canister. The differences in the reference concepts configuration are in the other two considered materials. A bentonite-base buffer (water-saturated FEBEX bentonite) and the Spanish Reference Granitic host rock are used in the case of the HLW concept in granite while a cement-base buffer (composed of Portland cement and calcareous aggregate without any reinforcement by steel structures) and the French Callovo-Oxfordian claystone in the HLW concept in clay.

Both HLW reference concepts in granite and clay will use the same vitrified waste (the French glass references SON-68 or the ISG) which will be considered as an equivalent porous medium accessible only to water. A similar glass dissolution model will also be used. The results of the numerical analyses performed by the ACED Task 3 (with the GRAAL model or other mechanistic ones) will provide simpler glass dissolution models (R_0/Rr model) to both HLW reference concepts.

The carbon-steel canister will be chemically treated in both HLW reference concepts as a non-porous material made of 100% metallic iron at the initial stage, and then as a porous material filled by corrosion products and remaining metallic iron. The carbon-steel corrosion will be kinetically controlled. The differences will be in the values of the corrosion rates.

Although the bentonite blocks are initially unsaturated, the reactive transport model of the HLW disposal cell in granite assumes that the bentonite is initially water-saturated. The model accounts for molecular diffusion. Advection is negligible due to the hydraulic conductivity of the bentonite is extremely low ($6 \cdot 10^{-14}$ m/s). Therefore, solute diffusion is the main solute transport mechanism. In the case of the reactive transport model of the HLW disposal cell in clay, diffusion is also the only considered transport process. Advection is never considered.

The accurate thermal transient stage and the cooling of the vitrified waste will be considered in the reactive transport model of the HLW disposal cell in granite while a simplified thermal stage over the first 1 000 y will be considered in the reactive transport model of the HLW disposal cell in clay.

The methodology of the reactive transport models of the geochemical evolution of the two HLW disposal cells is the same. Firstly, a reference base case is performed and lately several optional scenarios cases are proposed.

The generic configuration of the ILW disposal cell concept in granite and clay is very similar and the dimensions of the multibarrier system as well. Both reference concepts share the same boundaries conditions, regarding the waste source and its degradation, and the following materials: (1) the concrete walls of the waste containers, (2) the waste package backfill mortar, filling the voids between the containers and (3) the vault backfill mortar. The differences are related to the host rock considered, namely, the Callovo-Oxfordian claystone and the Spanish Reference Granitic host rock in the ILW concept in clay and crystalline rock, respectively. In addition, a low-pH shotcrete liner and the excavation damage zone (EDZ) is considered in the ILW cell in clay, only. Water inflow from the host-rock to the multibarrier system is also considered differently, since in the ILW disposal cell in clay diffusion is the main transport process, advection is considered in the case of crystalline rock. Simulation time in both cases is 100 000 years

Both ILW concepts use the same amount of waste which means they both assume the same number of waste box-shaped containers (with organic or metallic waste). The degradation of the waste is kinetically

control and considered as boundary in the disposal cell model. No temperature effects are part of the model according to the characteristics of the studied waste.

7. References

HLW disposal cell in granite

Águila, J.F., Samper, J., Mon, A., Montenegro, L., (2020). Dynamic update of flow and transport parameters in reactive transport simulations of radioactive waste repositories. Applied Geochemistry, https://doi.org/10.1016/j.apgeochem.2020.104585.

Appelo, C. A. J., Postma, D., (1993). Geochemistry, Groundwater and Pollution, A. A. Balkema, Brookfield, Vt.

Archie, G., (1942). The electrical resistivity log as an aid in determining some reservoir characteristics. Pet. Trans. AIME 146, 54-62.

Bradbury, M.H., Baeyens, B., (1997). A mechanistic description of Ni and Zn sorption on Na-montmorillonite. Part II: Modelling. J. Contaminant Hydrology, 27, 223-248.

Bradbury, M.H., Baeyens, B., (2002). Porewater chemistry in compacted re-saturated MX-80 bentonite: physicochemical characterisation and geochemical modelling. PSI Bericht 02-10, Villigen PSI and NTB 01-08, Nagra, Wettingen, Switzerland.

Bradbury, M.H., Baeyens, B., (2003). Porewater chemistry in compacted re-saturated MX-80 bentonite. Journal of Contaminant Hydrology 61, 329-338.

Bradbury, M.H., Baeyens, B., (2005). Modelling the sorption of Mn(II), Co(II), Ni(II), Zn(II), Cd(II), Eu(III), Am(III), Sn(IV), Th(IV), Np(V) and U(VI) on montmorillonite: linear free energy relationships and estimates of surface binding constants for some selected heavy metals and actinides. Geochim. Cosmochim. Acta 69, 875-892.

Buil, B., Gómez, P., Peña, J., Garralón, A., Turrero, M.J., Escribano, A., Sánchez, L., Durán, J.M., 2010. Modelling of bentonite–granite solutes transfer from an in situ fullscale experiment to simulate a deep geological repository (Grimsel Test Site, Switzerland). Appl. Geochem. 25, 1797-1804.

Cama, J., Ganor, J., Ayora, C., Lasaga, C.A. (2000). Smectite dissolution kinetics at 80ºC and pH 8.8. Geochim. Cosmochim. Acta 64, 15, 2701-2717.

Carman, P.C., (1937). Fluid through granular beds. Trans. Inst. Chem. Eng. 15, 150-166.

Červinka, R., Klajmon, M., Zeman, J., Vencelides, T., (2018). Geochemical calculations and reactive transport modelling. SURAO Technical Report 271/2018/ENG.

Dai, Z., Samper, J., (2004). Inverse problem of multicomponent reactive chemical transport in porous media: formulation and applications. Water Resour Res 40, W07407.

De Echave, T., M. Tribet, P. Jollivet, C. Marques, S. Gin, C. Jégou, (2018). Effect of clayey groundwater on the dissolution rate of SON68 simulated nuclear waste glass at 70 ºC. Journal of Nuclear Materials 503, 279-289.

De Marsily, G., (1986). Quantitative Hydrogeology. Academic Press Inc., San Diego, 440 pp.

De Windt, L., Lemmens, K., Samper, J., (2020). Definition of the materials and scenarios for HLW in tasks 3 & 4. ACED Work Package Technical note.

Deissmann G., Ait Mouheb N., Martin C., Name N., Jacques, D., Weetjens E., Kursten B., Leivo M., Somervuori, M., Carpen, L. (2020): Experiments and numerical model studies on interfaces. Final version as of xx.xx.xxxx of deliverable D2.5 of the HORIZON 2020 project EURAD. EC Grant agreement no: 847593.

Dzombak, D. A., Morel, F.M.M., (1990). Surface Complexation Modeling. Wiley Interscience, New York.

ENRESA, (2001). ENRESA 2000. Evaluación del comportamiento y de la seguridad de un almacén geológico profundo de residuos radiactivos en arcilla. ENRESA (in Spanish).

ENRESA, (2006). FEBEX: Updated final report 1994-2004. ENRESA Technical Publication PT 05-0/2006.

Fernández, J., (2017). Reactive Transport Models of low Permeability Structured Porous and Fractured Media. Ph.D. Dissertation. Universidad de A Coruña, Spain.

Fernández, A.M., Baeyens, B., Bradbury, M., Rivas, P., (2004). Analysis of the pore water chemical composition of a Spanish compacted bentonite used in an engineered barrier. Physics and Chemistry of the Earth 29(1), 105-118.

Fernández R, J Cuevas & U Mäder (2009). Modelling concrete interaction with a bentonite barrier. Eur. J. Mineral 21, 177-191.

Ferrand, K., Liu, S., Lemmens, K. (2015). International technical evaluation of alteration mechanisms relevant to glass corrosion, EXTERNAL REPORT SCK•CEN-ER-297, 49 p.

Féron, D., Crusset, D., Gras, J.-M., (2008). Corrosion issues in nuclear waste disposal. Journal of Nuclear Materials 379, 16-23.

Garrels, R.M., Christ, C.L., (1965). Solutions, Minerals, and Equilibria. Harper and Row, New York.

Gin, S., Abdelouas, A., Criscenti, L.J., Ebert, W.L., Ferrand, K., Geisler, T., Harrison, M.T., Inagaki, Y., Mitsui, S., Mueller, K.T., Marra, J.C., Pantano, C.G., Pierce, E.M., Ryan, J.V., Schofield, J.M., Steefel, C.I., Vienna, J.D., (2013). An international initiative on long-term behaviour of high-level nuclear waste glass. Materials Today 16, 243-248.

Gdowski, G.E., Bullen, D.B. (1988): Survey of degradation modes of candidate materials for high-level radioactive waste disposal containers. Oxidation and corrosion. Lawrence Livermore National Laboratory. Report UCID-21362. Vol.2.

Gdowski G.E., Estill J.C. (1996): The effect of water vapor on the steel at 65°C. Mat. Res. Soc. Symp. Proc.412: 533–535.

Gómez P., Turrero, M.J., Garralón, A., Peña, J., Buil, B., de la Cruz, B., Sánchez, M., Sánchez, D.M., Quejido, A., Bajos, C., Sánchez, L., (2006). Hydrogeochemical characteristics of deep groundwaters of the Hesperian Massif (Spain). Journal of Iberian Geology 32 (1), 113-131.

Giffaut, E., Grivé, M., Blanc, P., Vieillard, P., Colàs, E., Gailhanou, H., Gaboreau, S., Marty, N., Madé, B., Duro, L. (2014). Andra thermodynamic database for performance assessment: ThermoChimie. Applied Geochemistry 49, 225-236.

Hadi, J., Wersin, P., Serneels, V., Greneche, J.-M., (2019). Eighteen years of steel-bentonite interaction in the FEBEX in situ test at the Grimsel Test Site in Switzerland. Clays and Clay Minerals 67(2), 111-131.

Helgeson, H. C., Kirkham, D.H., (1974). Theoretical prediction of the thermodynamic behaviour of aqueous electrolytes at high pressures and temperatures: II. Debye-Hückel parameters for activity coefficients and relative partial molal properties. Am. J. Sci. 274, 1199-1261.

Hommel, J., Coltman, E., Class, H., (2018). Porosity-Permeability Relations for Evolving Pore Space: A Review with a Focus on (Bio-)geochemically altered Porous Media. Transp. Porous Med. 124, 589-629. https://doi.org/10.1007/s11242-018-1086-2.

Kwon, S, Lee, C.S., Cho, S.J., Jeon, S.W., Cho, W.J., (2009). An investigation of the excavation damaged zone at the KAERI underground research tunnel. Tunnelling and Underground Space Technology 24(1), 1-13. ISSN 0886-7798. https://doi.org/10.1016/j.tust.2008.01.004.

Lemmens, K., (2001). The effect of clay on the dissolution of nuclear waste glass. Journal of Nuclear Materials 298, 11-18.

Lu, C (2009) Reactive transport models in nuclear waste disposal and acid mine drainage. PhD Dissertation. University of A Coruña. Spain.

Martínez-Landa, L., Carrera, J., Pérez-Estaún, A., Gómez, P., Bajos, C., (2016). Structural geology and geophysics as a support to build a hydrogeologic model of granite rock. Solid Earth 7(3), 881-895. 10.5194/se-7-881-2016.

Mon, A., (2017). Coupled Thermo-Hydro-Chemical-Mechanical Models for the Bentonite Barrier in a Radioactive Waste Repository. Ph.D. Dissertation. University of A Coruña, Spain, 483 pp.

Neeft, E., (2020). Personal communication.

Neeft, E., Weetjens E., Vokal A., Leivo M., Cochepin B., Martin C., Munier I., Deissmann G., Montoya V., Poskas P., Grigaliuniene D., Narkuniene A., García E., Samper J., Montenegro L., Mon A. (2019): Treatment of chemical evolution in National Programmes, Deliverable 2.4 of the HORIZON 2020 project EURAD. EC Grant agreement no: 847593.

Ortiz, L., Volckaert, G., Mallants, D., (2002). Gas generation and migration in Boom clay, a potential host rock formation for nuclear waste storage. Eng. Geol. 64, 287-296.

Poonoosamy, J., Wanner, C., Alt Epping, P., Águila, J.F., Samper, J., Montenegro, L., Xie, M., Su, D., Mayer, K.U., Mäder, U., Van Loon, L.R., Kosakowski, G., (2018). Benchmarking of reactive transport codes for 2D simulations with mineral dissolution–precipitation reactions and feedback on transport parameters. Computat. Geosci. https://doi.org/10.1007/s10596-018-9793-x.

Pusch, R. (2001). The microstructure of MX-80 clay with respect to its bulk physical properties under different environmental conditions. SKB Technical Report TR-01-08.

Rébiscoul, D. & Tormos, V. & Godon, Nicole & Mestre, J.-P & Cabié, Martiane & Amiard, Guillaume & Foy, Eddy & Frugier, P. & Gin, Stephane. (2015). Reactive transport processes occurring during nuclear glass alteration in presence of magnetite. Applied Geochemistry. 58. 10.1016/j.apgeochem.2015.02.018. 58. 10.1016/j.apgeochem.2015.02.018.

Rozalén, M.L., Huertas, F.J., Brady, P.V., Cama, J., García-Palma, S., Linares, J. (2008). Experimental study of the effect of pH on the kinetics of montmorillonite dissolution at 25 ºC. Geochim. Cosmochim. Acta 72, 4224-4253.

Samper, J., Lu, C., Montenegro, L., (2008). Coupled hydrogeochemical calculations of the interactions of corrosion products and bentonite. Physics and Chemistry of the Earth 33, S306-S316, doi:10.1016/j.pce.2008.10.009.

Samper, J., Xu, T., Yang, C., (2009). A sequential partly iterative approach for multicomponent reactive transport CORE^{2D}. Comput. Geosci. 13, 301-316.

Samper, J., Naves, A., Montenegro, L., Mon, A., (2016) Reactive transport modelling of the long-term interactions of corrosion products and compacted bentonite in a HLW repository in granite: uncertainties and relevance for performance assessment. Applied Geochemistry 67: 42–51.

Samper, J., Mon, A., Montenegro, L., (2018), A revisited thermal, hydrodynamic, chemical and mechanical model of compacted bentonite for the entire duration of the FEBEX in situ test, Applied Clay Sciences, Vol 160: 58-70. doi.org/10.1016/j.clay.2018.02.019.

Savage D, R Arthur, C Watson, J Wilson & B Strömberg (2011). Testing geochemical models of bentonite pore water evolution against laboratory experimental data. Physics and Chemistry of the Earth 36 (2011) 1817–1829.

Seigneur, N., Mayer, U., Steefel, C., (2019). Reactive Transport in Evolving Porous Media, Rev. Mineral. Geochem. 85 (1), 197-238. https://doi.org/10.2138/rmg.2019.85.7.

Simunek, J., Suares, D.L., (1993). UNSATCHEM-2D. Code for simulating two-dimensional variably saturated water flow, heat transport, carbon dioxide production and transport, and multicomponent

solute transport with major ion equilibrium and kinetic chemistry. User's manual. U.S. Salinity Laboratory, Agricultural Research Service, U.S. Department of Agriculture, Riverside, California.

Steefel, C.I., Appelo, C.A.J., Arora, B., Jacques, D., Kalbacher, T., Kolditz, O., Lagneau, V., Lichtner, P.C., Mayer K.U., Meeussen J.C.L., Molins, S., Moulton, D., Shao, H., Simunek, J., Spycher, N., Yabusaki, S.B., Yeh, G.T., (2015). Reactive transport codes for subsurface environmental simulation. Comput. Geosci. 19, 445-478. https://doi.org/10.1007/s10596-014-9443-x.

Tournassat, C., (2003). Cations-clay interactions: The Fe(II) case. Application to the problematic of the French deep nuclear repository field concept. Ph.D. Dissert. Grenoble, France.

Wilson JC, S Benbow, H Sasamoto, D Savage & C Watson (2015). Thermodynamic and fully-coupled reactive transport models of a steel–bentonite interface. App. Geochem. 61,10-28.

Wolery, T.J., (1992). EQ3/6, a software package for geochemical modeling of aqueous systems: package overview and installation guide (version 7.0). Technical Report UCRL-MA-110662-Pt 1. Lawrence Livermore National Laboratory, CA, USA.

Yandrisevits M.A., Londero P., Carò F., Rizzo A., Cappuccini C. (2017): Wavelength-dependent absorption and scattering effects on laser cleaning of a corroded iron alloy European scale armor. Lasers in the Conservation of Artworks XI, Proceedings of LACONA XI, P. Targowski *et al*. (Eds.), NCU Press, Toruń 2017.

Zheng, L., Samper, J., (2008). A coupled THMC model of FEBEX mock-up test. Physics and Chemistry of the Earth 33, S486-S498.

Zheng, L., Samper, J., Montenegro, L., (2011). A coupled THC model of the FEBEX in situ test with bentonite swelling and chemical and thermal osmosis, Journal of Contaminant Hydrology 126, 45-60.

HLW disposal cell in clay

Agullo, J., Bataillon, C., Michaud, N. (2015). Corrosion monitoring in mixture cement paste – bentonite. Global 2015, Sep 2015, Paris, France.

Agullo, J., Bataillon, C., Michaud, N. (2017). Preliminary electrochemical corrosion monitoring of iron in mixture cement paste–bentonite. Corrosion Engineering, Science and Technology 52, 155–161.

Andra (2016a). Safety Options Report - Operating Part (DoS-Expl). Report CG-TE-D-NTE-AMOA-SRr0000-5-0060, Andra, France.

Andra (2016b). Safety Options Report - Operating Part (DoS-AF). Report CG-TE-D-NTE-AMOA-SR2-0000-r5-0062, Andra, France.

Bildstein, O., Claret, F., Frugier, P. (2019). RTM for Waste Repositories. Reviews in Mineralogy and Geochemistry 85, 419–457.

Blanc, P., Lassin, A., Piantone, P., Azaroual, M., Jacquemet, N., Fabbri, A., and Gaucher, E. C. (2012). Thermoddem: A geochemical database focused on low temperature water/rock interactions and waste materials. Appl. Geochem. 27, 2107–2116.

Bodén, A., Pettersson, S. (2011). Development of rock bolt grout and shotcrete for rock support and corrosion of steel in low-pH cementitious materials. Report SKB R-11-08, SKB, Sweden.

Bradbury, M.H., Baeyens, B. (2002). Sorption of Eu on Na- and Ca-montmorillonites: Experimental investigations and modelling with cation exchange and surface complexation. Geochimica et Cosmochimica Acta 66, 2325–2334.

Cox, J.D., Wagman, D.D., Medvedev, V.A. (Vadim A., 1989. CODATA key values for thermodynamics. Hemisphere Pub. Corp, New York

Craeye, B., De Schutter, G., Van Humbeeck, H., Van Cotthem, A. (2009). Early age behaviour of concrete supercontainers for radioactive waste disposal. Nuclear Engineering and Design 239, 23–35.

Dauzeres, A., Achiedo, G., Nied, D., Bernard, E., Alahrache, S., Lothenbach, B. (2016). Magnesium perturbation in low-pH concretes placed in clayey environment - Solid characterizations and modeling. Cem. Conc. Res., 79, 137-150.

Debure, M., Frugier, P., De Windt, L., Gin, S. (2012). Borosilicate glass alteration driven by magnesium carbonates, Journal of Nuclear Materials 420, 347-361.

Debure, M., De Windt, L., Frugier, P., Gin, S. (2013). HLW glass dissolution in the presence of magnesium carbonate: Diffusion cell experiment and coupled modeling of diffusion and geochemical interactions. Journal of Nuclear Materials 443, 507–521.

Debure, M., Linard, Y., Martin, C., Claret, F. (2019). In situ nuclear-glass corrosion under geological repository conditions. Materials Degradation 3, 38.

De Craen, M., Wang, L., Van Geet, M., Moors, H. (2004). Geochemistry of Boom Clay pore water at the Mol site. Report SCK•CEN-BLG-990, CSK-CEN, Belgium.

De Echave, T., Tribet, M., Jollivet, P., Marques, C., Gin, S., Jégou, C. (2018). Effect of clayey groundwater on the dissolution rate of SON68 simulated nuclear waste glass at 70 ºC. Journal of Nuclear Materials 503, 279-289.

Deissmann, G., Haneke, K., Filby, A., Wiegers, R. (2016). Dissolution behaviour of HLW glasses under OPERA repository conditions. Report OPERA-PU-IBR511A.

Deissmann G., Ait Mouheb N., Martin C., Name N., Jacques, D., Weetjens E., Kursten B., Leivo M., Somervuori, M., Carpen, L., 2021. Experiments and numerical model studies on interfaces. Final version as of xx.xx.xxxx of deliverable D2.5 of the HORIZON 2020 project EURAD. EC Grant agreement no: 847593.

De Windt, L., Pellegrini, D., van der Lee, J. (2004). Coupled modeling of cement/ claystone interactions and radionuclides migration, Journal of Contaminant Hydrology 68, 165–182.

De Windt, L., Leclercq, S., van der Lee, J. (2006). Assessing the durability of nuclear glass with respect to silica controlling processes in a clayey underground disposal. Materials Research Society Proceedings 932, 313–320.

De Windt, L., Marsal, F. Tinseau, E., Pellegrini, D. (2008). Reactive transport modeling of geochemical interactions at a concrete/argillite interface, Tournemire site (France). Physics and Chemistry of the Earth 33, 295–305.

De Windt, L., Marsal, F., Corvisier, J., Pellegrini, D. (2014). Modeling of oxygen gas diffusion and consumption during the oxic transient in a disposal cell of radioactive waste. Applied Geochemistry 41, 115–127.

De Windt, L., Spycher, N. (2019). Reactive transport modeling: a key performance assessment tool for the geologic disposal of nuclear waste. Elements 15, 99–102.

Duro, L., Altmaier, M., Holt, E., Mäder, U., Claret, F., Grambow, B., Idiart, A., Valls, A., Montoya, V. (2020). Contribution of the results of the CEBAMA project to decrease uncertainties in the Safety Case and Performance Assessment of radioactive waste repositories. Applied Geochemistry 112, 104479.

Fleury, B., Godon, N., Ayral, A., Perret, D., Dussossoy, J.-L., Gin, S. (2014). Development of an Experimental Design to Investigate the Effects of R7T7 Glass Composition on the Residual Rate of Alteration. Procedia Materials Science 7, 193 – 201.

Fournier, M., Ducasse, T., Pérez, A., Barchouchi, A., Daval, D., Gin, S. (2019). Effect of pH on the stability of passivating gel layers formed on International Simple Glass. Journal of Nuclear Materials 524, 21–38.

Frugier, P., Gin, S., Minet, Y., Chave, T., Bonin, B., Godon, N., Lartigue, J.E., Jollivet, P., Ayral, A., De Windt, L., Santarini, G. (2008). SON68 nuclear glass dissolution kinetics: Current state of knowledge and basis of the new GRAAL model. Journal of Nuclear Materials 380, 8–21.

Frugier, P., Rajmohan, N., Minet, Y., Godon, N., Gin, S., 2018. Modeling glass corrosion with GRAAL. Materials Degradation 2:35.

García Calvo, J.L., Sánchez Moreno, M., Alonso Alonso, M.C., Hidalgo López, A., García Olmo, J. (2013). Study of the Microstructure Evolution of Low-pH Cements Based on Ordinary Portland Cement (OPC) by Mid- and Near-Infrared Spectroscopy, and Their Influence on Corrosion of Steel Reinforcement. Materials 6, 2508–2521.

Giffaut, E., Grivé, M., Blanc, P., Vieillard, P., Colàs, E., Gailhanou, H., Gaboreau, S., Marty, N., Madé, B., Duro, L. (2014). Andra thermodynamic database for performance assessment: ThermoChimie. Applied Geochemistry 49, 225–236.

Gin, S., Abdelouas, A., Criscenti, L.J., Ebert, W.L., Ferrand, K., Geisler, T., Harrison, M.T., Inagaki, Y., Mitsui, S., Mueller, K.T., Marra, J.C., Pantano, C.G., Pierce, E.M., Ryan, J.V., Schofield, J.M., Steefel, C.I., Vienna, J.D. (2013). An international initiative on long-term behaviour of high-level nuclear waste glass. Materials Today 16, 243-248.

Govaerts, J., Weetjens, E. (2010). Scoping Calculation: When and in which concentration will aggressive species reach the overpack surface. Report SCK•CEN-ER-133, SCK-CEN, Belgium.

Huang, Y., Shao, H., Wieland, E., Kolditz, O., Kosakowski, G. (2018). A new approach to coupled two-phase reactive transport simulation for long-term degradation of concrete. Construction and Building Materials 190, 805–829.

Idiart, A., Laviña, M. (2019). Final results and main outcomes of the Modelling Task. Deliverable n°D3.07. CEBAMA European Project n° 662147.

Idiart, A., Olmeda, J., Laviña, M. (2019). Modelling of Concrete Degradation in SFL - Influence of Concrete Mix Design. Svensk Kärnbränslehantering AB. SKB R-19-14.

Idiart, A., Laviña, M., Cochepin B, Pateau, A. (2020). Hydro-chemo-mechanical modelling of long-term evolution of bentonite swelling. Appl. Clay Sci., 195.

Idiart, A., Laviña, M., Kosakowski, G. *et al*. (2020). Reactive transport modelling of a low-pH concrete / clay interface. Applied Geochemistry 115, 104562.

Jacques, D., Perko, J., Seetharam, S., Mallants, D. (2011). Model abstraction addressing long-term simulations of chemical degradation of large- scale concrete structures. Cement-based Materials for Nuclear Wastes. NUWCEM 2011, 11-13 October, Avignon, France.

Jollivet, P., Gin, S., Schumacher, S. (2012). Forward dissolution rate of silicate glasses of nuclear interest in clay-equilibrated groundwater. Chemical Geology 330–331, 207-217.

Kosakowski, G. (2020). Reference document for properties of cementitious materials in ACED with GEM-Selektor and based on CEMDATA V18.1. Technical note, HORIZON 2020 project EURAD. EC Grant agreement no: 847593.

Kulik, D.A (2011). Improving the structural consistency of C-S-H solid solution thermodynamic models. Cement and Concrete Research 41, 477–495.

Kursten, B., Druyts, F. (2015). Assessment of the uniform corrosion behaviour of carbon steel radioactive waste packages with respect to the disposal concept in the geological Dutch Boom Clay formation. Report OPERA-PU-SCK513, Netherlands.

Liu, S., Jacques, D., Govaerts, J., Wang, L. (2014). Conceptual model analysis of interaction at a concrete–Boom Clay interface. Physics and Chemistry of the Earth 70–71, 150–159.

Lothenbach, B., Le Saout, G., Ben Haha, M., Figi, R., Wieland, E. (2012). Hydration of a low-alkali CEM III/B–SiO2 cement (LAC). Cem Concr Res 42, 410–423.

Lothenbach, B., Rentsch, D., Wieland, E. (2014). Hydration of a silica fume blended low-alkali shotcrete cement. Phys. Chem. Earth 70-71, 3–16.

Lothenbach, B., Kulik, D.A., Matschei, T., Balonis, M., Baquerizo, L., Dilnesa, B., Miron, G.D., Myers, R.J. (2019). Cemdata18: A chemical thermodynamic database for hydrated Portland cements and alkali-activated materials. Cem. Concr. Res. 115, 472–506.

Marmier, N., Fromage, F. (2000). Sorption of Cs(I) on magnetite in the presence of silicates. J. Colloid Interface Sci., 223, 83–88.

Marques Fernandes, M., Baeyens, B., Dähn, R., Scheinost, A.C., Bradbury, M.H. (2012). U(VI) Sorption on Montmorillonite in the Absence and Presence of Carbonate: A Macroscopic and Microscopic Study. Geochimica et Cosmochimica Acta 93, 262–277.

Marty, N.C.M., Bildstein, O., Blanc, P. *et al*. (2015). Benchmarks for multicomponent reactive transport across a cement/clay interface. Comput Geosci 19, 635–653.

McCarter, W.J., Starrs, G. and Chrisp, T.M. (2000). Electrical conductivity, diffusion, and permeability of Portland cement-based mortars. Cement and Concrete Research 30, 1395-1400.

Michau, N., Bourbon, X. (2016). Coulis cimentaire pour remplissage d'un espace annulaire autour d'une alvéole de stockage de déchets radioactifs creusée dans un milieu argileux. Brevet FR 3 031 103 - A1, INPI, France.

Nardi, A., Idiart, A., Trinchero, P., de Vries, L. M., Molinero J. (2014). Interface COMSOL-PHREQC (iCP), an efficient numerical framework for the solution of coupled multiphysics and geochemistry. Computers & Geosciences 69, 10-21.

Neeft, E., Weetjens, E., Vokal, A., Leivo, M., Cochepin, B., Martin, C., Munier, I., Deissmann, G., Montoya, V., Poskas, P., Grigaliuniene, D., Narkuniene, A., Garcia, E., Samper, J., Montenegro, L., Mon, A. (2019). Treatment of chemical evolution in National Programmes, D 2.4 of the HORIZON 2020 project EURAD. EC Grant agreement no: 847593.

Odorowski, M., Jégou, C., De Windt, L., Broudic, V., Jouan, G., Peuget, S., Martin, C. (2017). Effect of metallic iron on the oxidative dissolution of UO2 doped with a radioactive alpha emitter in synthetic Callovian-Oxfordian groundwater. Geochimica et Cosmochimica Acta 219, 1–21.

Parkhurst, D.L., Appelo, C.A.J. (2013). Description of input and examples for PHREEQC Version3— a computer program for speciation, batch-reaction, one-dimensional transport, and inverse geochemical calculations. U.S.Department of the Interior, U.S. Geological Survey Techniques and Methods 6-A43.

Perko, J., Mayer, K.U., Kosakowski, G., De Windt, L., Govaerts, J., Jacques, D., Su, D., Meeussen J.C.L. (2015). Decalcification of cracked cement structures. Computational Geosciences 19, 673–693.

Saheb, M., Gallien, J.P., Descostes, M., Raimbault, L., Perez, A., Neff, D., Marsal, F., Pellegrini, D., Dillmann, P. (2014). Influence of an aerated/anoxic transient phase on the long-term corrosion of iron. Corros. Sci. 86, 71–80.

Seetharam, S., Jacques, D. (2015). Potential Degradation Processes of the Cementitious EBS Components, their Potential Implications on Safety Functions and Conceptual Models for Quantitative Assessment, report OPERA-PU-SCK514, Netherlands.

Seigneur, N., Kangni-foli, E., Lagneau, V., Dauzères, A., Poyet, S., Le Bescop, P. (2020). Cement and concrete research predicting the atmospheric carbonation of cementitious materials using fully coupled two-phase reactive transport modelling. Cem. Concr. Res. 130, 105966.

Sin, I., Lagneau, V., Corvisier, J. (2017). Integrating a compressible multicomponent two-phase flow into an existing reactive transport simulator. Advances in Water Resources 100, 62–77.

Smart, N.R., Rance, A.P., Nixon, D.J., Fennell, P.A.H., Reddy, B., Kursten, B. (2017). Summary of studies on the anaerobic corrosion of carbon steel in alkaline media in support of the Belgian supercontainer concept. Corrosion Engineering, Science and Technology 52:sup1, 217–226.

Swanton, S.W., Baston, G.M.N., Smart N.R. (2015). CArbon-14 Source Term CAST – Rates of steel corrosion and carbon-14 release from irradiated steels – state of the art review (D2.1).

van der Lee, J., De Windt, L., Lagneau, Goblet, P. (2003). Module-oriented modeling of reactive transport with HYTEC. Computers and Geosciences 29, 265–275.

Wang, L., Jacques, D., De Cannière, P. (2010). Effects of an alkaline plume on the Boom Clay as a potential host formation for geological disposal of radioactive waste. Report SCK•CEN-ER-28, SCK-CEN, Belgium.

Weetjens, E., Marivoet J., Govaerts, J. (2012). Preparatory Safety Assessment. Report SCK•CEN-ER-215, SCK-CEN, Belgium.

Yu, L., Weetjens, E. (2012). Estimation of the gas source term for spent fuel, vitrified high-level waste, compacted waste and MOSAIK waste. Report SCK•CEN-ER-162, SCK-CEN, Belgium.

ILW disposal cell in clay

Águila, J.F., Montoya, V., Samper, J., Montenegro, L., Kosakowski, G., Krejci, P., Pfingsten W. (2021) Modelling cesium migration through Opalinus clay: A benchmark for single- and multi-species sorption-diffusion models. Computational Geosciences. https://doi.org/10.1007/s10596-021-10050-5.

Ait Mouheb, N, Joseph, C., Schäfer T, Montoya V (2022) Multi-method approach for studying chloride-36 and tritiated water migration through “low-pH” cement pastes and mortars. Cement and Concrete Research (submitted).

Andra (2016a) Safety Options Report - Operating Part (DoS-Expl).

Andra (2016b) Safety Options Report - Operating Part (DoS-AF).

Baes, C.F., Mesmer, R.E., (1977). The Hydrolysis of Cations. Wiley-Blackwell. https://doi.org/10.1002/bbpc.19770810252

Ballarini, E., Beyer, C., Bauer, R. D., Griebler, C., and Bauer, S. (2014) Model based evaluation of a contaminant plume development under aerobic and anaerobic conditions in 2-D bench-scale tank experiments, Biodegradation, 25, 351–371, 2014.

Bamforth, P. B., G. M. N. Baston, J. A. Berry, F. P. Glasser, T. G. Heath, C. P. Jackson, D. Savage, and S. W. Swanton. 2012. “Cement Materials for Use as Backfill, Sealing and Structural Materials in Geological Disposal Concepts. A Review of Current Status.” Serco, no. SERCO/005125/001 Issue 3: 1–235.

Bernard, E., Lothenbach, B., Chlique, C., Wyrzykowski, M., Dauzeres, A., Pochard, I., & Cau-Dit-Coumes, C. (2019). Characterization of magnesium silicate hydrate (MSH). Cement and concrete research, 116, 309-330.

Berner, U., Kulik, D.A, Kosakowski, G. (2013) Geochemical impact of a low-pH cement liner on the near field of a repository for spent fuel and high-level radioactive waste. Physics and Chemistry of the Earth, Parts A/B/C, 64, 46-56.

Beyer C., Li, D., De Lucia M., Kühn M., Bauer S. (2012) Modelling CO2-induced fluid–rock interactions

in the Altensalzwedel gas reservoir. Part II: coupled reactive transport simulation. Environmental Earth Sciences, 67, 573–588.

Bilke, L., Flemisch, B., Kolditz, O., Helmig, R., Nagel T. (2019). Development of open-source porous-media simulators: principles and experiences. Transport in Porous Media. 130 (1), 337 – 361.

Birkholzer, J.T, Bond, A.E., Hudson, J.A, Jing, L., Tsang, C.F., Shao, H., Kolditz, O. (2018) Decovalex-2015: an international collaboration for advancing the understanding and modeling of coupled thermo-hydro-mechanical-chemical (thmc) processes in geological systems. Environmental Earth Sciences, 77(14).

Blanc, P., Lassin, A., Piantone, P., Azaroual, M., Jacquemet, N., Fabbri, A., Gaucher, E. C., (2012). Thermoddem: A geochemical database focused on low temperature water/rock interactions and waste materials. Appl. Geochem. 27, 2107–2116. https://doi.org/10.1016/j.apgeochem.2012.06.002

Boog, J., Kalbacher, T., Nivala, J., Forquet, N., van Afferden, M., Müller, R.A., (2019a) Modeling the relationship of aeration, oxygen transfer and treatment performance in aerated horizontal flow treatment wetlands, Water Res. 157 , 321 – 334.

Boog, J., Nivala, J., Kalbacher, T., van Afferden, M., Müller, R.A., (2020) Do wastewater pollutants impact oxygen transfer in aerated horizontal flow wetlands? Chem. Eng. J, art. 123173.

Böttcher, N., Görke, U-J, Kolditz, O., Nagel, T (2017). Thermo-mechanical investigation of salt caverns for short-term hydrogen storage. Environmental Earth Sciences, 76(3), 98

Bradbury, M.H., Baeyens, B. (2005a). Experimental and Modelling Investigations on Na-Illite: Acid-Base Behaviour and the Sorption of Strontium, Nickel, Europium and Uranyl. NAGRA Technical Report 04–02 (June).

Bradbury, M.H., Baeyens, B., (2005b). Modelling the sorption of Mn(II), Co(II), Ni(II), Zn(II), Cd(II), Eu(III), Am(III), Sn(IV), Th(IV), Np(V) and U(VI) on montmorillonite: linear free energy relationships and estimates of surface binding constants for some selected heavy metals and actinides. Geochim. Cosmochim. Acta 69, 875–892.

Calvo, J. G., Hidalgo, A., Alonso, C., Luco, L. F. (2010). Development of low-pH cementitious materials for HLRW repositories: Resistance against ground waters aggression. Cement and Concrete Research, 40 (8): 1290–97.

Carman, P.C., (1937). Fluid through granular beds. Trans. Inst. Chem. Eng. 15, 150-166.

Centler, F., Shao, H. B., De Biase, C., Park, C. H., Regnier, P., Kolditz, O., and Thullner, M.: GeoSysBRNS – A flexible multidimensional reactive transport model for simulating biogeochemical subsurface processes, Comput. Geosci., 36, 397–405, 2010.

Chen, C., Shao, H., Naumov, D., Kong, Y., Tu, K., Kolditz, O., (2019). Numerical investigation on the performance, sustainability, and efficiency of the deep borehole heat exchanger system for building heating. Geotherm. Energy 7, 18.

Chen Y.M., Xua W.J., Ling D.S, Zhan L.T, Gao W. (2020) A degradation–consolidation model for the stabilization behavior of landfilled municipal solid waste. Computers and Geotechnics, 118, 103341

Crossland, I. G. (2007). Cracking of the Nirex Reference Vault Backfill: A Review of Its Likely Occurence and Significance. Nda, no. Report CCL/2007/1: 1–49.

Diomidis, N, Cloet, V, Leupin, O.X., Marschall, P., Poller, A., Stein M. (2016) Production, consumption and transport of gases in deep geological repositories according to the Swiss disposal concept. NAGRA Technical Report 16-03, Switzerland.

Dzombak, D. A., Morel, F.M.M., (1990). Surface Complexation Modeling. Wiley Interscience, New York.

Diersch H.-J. (2014) FEFLOW: Finite element modeling of flow, mass and heat transport in porous and fractured media. Springer.

Duro, L., Grivé, M., Giffaut, E. (2012). ThermoChimie, the ANDRA Thermodynamic Database. Materials Research Society Symposium Proceedings, 1475: 589–92.

Enssle, C. P., Cruchaudet, M., Croisé, J., Brommundt, J. (2011). Determination of the permeability of the Callovo-Oxfordian clay at the metre to decametre scale. Physics and Chemistry of the Earth, 36 (17–18): 1669–78.

Fischer, T., Naumov, D., Magri, F., Walther, M., Wang, W., Kolditz O. (2019) Parallelization schemes in OpenGeoSys and applications to density driven flow and crack evolution in geosystems. Geophysical Research Abstracts, 21, EGU2019-16844.

Giffaut, E., Grivé, M., Blanc, P., Vieillard, P., Colàs, E., Gailhanou, H., Gaboreau, S., Marty, N., Madé, B., Duro, L., 2019. Andra thermodynamic database for performance assessment: ThermoChimie, Appl. Geochem. 49, 225–236. doi:10.1016/j.apgeochem.2014.05.007.

Glaus M, Van Loon (2004) A generic procedure for the assessment of the effect of concrete admixtures on the retention behaviour of cement for radionuclides: Concept and case studies. PSI Bericht Nr. 04-02, Switzerland.

Glynn, P., (2019). Solid-solution solubilities and thermodynamics: Sulfates, carbonates and halides, in: Sulfate Minerals: Crystallography, Geochemistry, and Environmental Significance. Walter de Gruyter GmbH, pp. 481–511. https://doi.org/10.2138/rmg.2000.40.10

Govaerts, J., Weetjens, E. (2010). Scoping Calculation: When and in which concentration will aggressive species reach the overpack surface. Report SCK•CEN-ER-133, SCK-CEN, Belgium.

Grunwald, N., Maßmann, J., Kolditz, O., Nagel, T., (2020): Non-iterative phase-equilibrium model of the H_2O-CO_2-NaCl-system for large-scale numerical simulations. Math. Comput. Simul. 178 , 46 – 61.

He, W., Beyer, C, Fleckenstein, J.H, Jang, E., Kolditz, O., Naumov, D., Kalbacher, T (2015) A parallelization scheme to simulate reactive transport in the subsurface environment with OGS#IPhreeqc 5.5.7-3.1.2. Geosci. Model Dev., 8, 3333–3348.

Hein, P., Zhu, K., Bucher, A., Kolditz, O., Pang, Z., Shao, H. (2016). Quantification of exploitable shallow geothermal energy by using borehole heat exchanger coupled ground source heat pump systems. Energy Conversion and Management, 127, 80 – 89.

Helgeson, H.C., Delany, J.M., Nesbitt, H.W., Bird, D.K., (1978). Summary and critique of the thermodynamic properties of rock-forming minerals. Am. J. Sci. 278A, 1–229.

Helmig, R. (1993). Theorie und Numerik der Mehrphasenströmungen in geklüftet-poösen Medien. PhD thesis, Institut fr Strömungsmechanik und Elektronisches Rechnen im Bauwesen, Universitt Hannover.

Huang, H., Shao, H., Wieland, E., Kolditz, O., Kosakowski G. (2018) A new approach to coupled two-phase reactive transport simulation for long-term degradation of concrete, Construction and Building Materials 190: 805-829.

Hummel W., Berner, U. Curti, E., Pearson F.J., Thoenen T (2002) Nagra/PSI Chemical Thermodynamic Data Base 01/01. Radiochim. Acta 90, 805–813

Idiart, A., Lavina, M., Kosakowski, G., Cochepin, B., Meeussen, J.C.L., Samper, J., Mon, A., Montoya, V., Munier, I., Poonoosamy, J. Montenegro, L., Deissmann, G., Rohmen, S., Damiani, H. Coene, E., Nieves A (2020) Benchmark of reactive transport modelling of a low-pH concrete/clay interface. Appl. Geochem., 104562.

Jacobs, E. Vockaert G., Maes, N., Weetjens E., Govaerts J. (2013). Determination of gas diffusion coefficients in saturated porous media: He and CH4 diffusion in Boom Clay. Applied Clay Science, 83–84, 217-223

Jang, E., Boog, J., He, W. Kalbacher, T (2017) OpenGeoSys Tutorial: Computational Hydrology III: OGS# IPhreeqc Coupled Reactive Transport Modeling.

Jing, M., Heße, F., Kumar, R., Kolditz, O., Kalbacher, T., Attinger, S., (2019) Influence of input and parameter uncertainty on the prediction of catchment-scale groundwater travel time distributions. Hydrol. Earth Syst. Sci. 23 (1), 171 – 190.

Jing, M, Hee, F., Kumar, R., Wang, W., Fischer, T., Walther, M., Zink, M., Zech, A., Samaniego, L., Kolditz, O., Attinger S. (2018). Improved regional-scale groundwater representation by the coupling of the mesoscale hydrologic model (mhm v5.7) to the groundwater model opengeosys (ogs). Geoscientific Model Development, 11(5), 1989–2007.

Johnson, J.W., Oelkers, E.H., Helgeson, H.C., (1992). SUPCRT92: A software package for calculating the standard molal thermodynamic properties of minerals, gases, aqueous species, and reactions from 1 to 5000 bar and 0 to 1000°C. Comput. Geosci. 18, 899–947. https://doi.org/10.1016/0098-3004(92)90029-Q

Kolditz, O. (1990) Zur Modellierung und Simulation geothermischer Transportprozesse in untertägigen Zirkulationssystemen. PhD thesis, Akademie der Wissenschaften der DDR, Berlin.

Kolditz O., Bauer S. (2004). A process-oriented approach to computing multi-field problems in porous media. Journal of Hydroinformatics, 6(3), 225–244.

Kolditz, O., Bauer, B., Beyer, C., Böttcher, N., Dietrich, P., Gürke, U-J., Kalbacher, T., Park, C.H, Sauer, U., Schtze, C, Shao, H, Singh, A., Taron, J., Wang W., Watanabe, N (2012b). A systematic benchmarking approach for geologic CO2 injection and storage. Environmental Earth Sciences, 67(2), 613–632.

Kolditz O., Bauer S., Bilke L., Böttcher N., Delfs J.O., Fischer T., Görke U.J., Kalbacher T., Kosakowski G., McDermott C.I., Park C.H., Radu F., Rink K., Shao H., Shao HB., Sun F., Sun Y.Y., Singh A.K., Taron J., Walther M., Wang W., Watanabe N., Wu N., Xie M., Xu W., Zehner B. (2012a): OpenGeoSys: an open-source initiative for numerical simulation of thermo-hydro-mechanical/chemical (THM/C) processes in porous media, Environ. Earth Sci., 67(2): 589-599.

Kolditz, O., Nagel, T., Shao, H., Wang, W., Bauer, S. (ed.). (2018) Thermo-Hydro-Mechanical-Chemical Processes in Fractured Porous Media: Modelling and Benchmarking. Terrestrial Environmental Sciences. Springer International Publishing, Cham.

Kosakowski, G., Berner, U (2013) The evolution of clay rock/cement interfaces in a cementitious repository for low- and intermediate level radioactive waste. Physics and Chemistry of the Earth, Parts A/B/C, 64, 65-86.

Kosakowski, G., Berner, U., Wieland, E., Glaus, M., Degueldre C (2014) Geochemical Evolution of the L/ILW Near-field, NAGRA Technical report 14-11, Switzerland.

Kosakowski, G., Huang, Y. (2019) Notes on modelling coupled processes in a single waste package. Internal Report TM-44-19-09, Paul Scherrer Institut, Villigen, Switzerland.

Kosakowski, G., Watanabe, N. (2014) OpenGeoSys-Gem: a numerical tool for calculating geochemical and porosity changes in saturated and partially saturated media, Phys. Chem. Earth, 70–71, 138–149.

Kozeny, J. (1927). Uber Kapillare Leitung Der Wasser in Boden. Sitzungsber. Akad. Wiss. Wien 136: 271– 306.

Kroehn, K. P. (1991) Simulation von Transportvorgngen im klüftigen Gestein mit der Methode der Finiten Elemente. PhD thesis, Institut fr Strömungsmechanik und Elektronisches Rechnen im Bauwesen, Universitt Hannover.

Kulik, D.A (2011). Improving the structural consistency of C-S-H solid solution thermodynamic models. Cement and Concrete Research 41, 477–495.

Kulik, D. A., Miron, G. D., & Lothenbach, B. (2022). A structurally-consistent CASH+ sublattice solid solution model for fully hydrated C-S-H phases: thermodynamic basis, methods, and Ca-Si-H2O core sub-model. Cement and Concrete Research, 151, 106585 (21 pp.). https://doi.org/10.1016/j.cemconres.2021.106585

Kulik, D. A., Wagner, T., Dmytrieva, S. V., Kosakowski, G., Hingerl, F. F., Chudnenko, K. V., Berner, U.

R. (2013). GEM-Selektor geochemical modeling package: revised algorithm and GEMS3K numerical kernel for coupled simulation codes. Computational Geosciences, 17(1), 1-24.

Lehmann, C., Kolditz, O., Nagel, T. (2018). Models of Thermochemical Heat Storage. Computational Modeling of Energy Systems. Springer International Publishing.

Lehmann, C., Kolditz, O., Nagel T. (2019). Modelling sorption equilibria and kinetics in numerical simulations of dynamic sorption experiments in packed beds of salt/zeolite composites for thermochemical energy storage. International Journal of Heat and Mass Transfer, 128, 1102–1113.

Lemire, R.J., Berner, U., Musikas, C., Palmer, D.A., Taylor, P., Tochiyama, O., (2013). Chemical thermodynamics of iron Part 1. Chem. Thermodyn. 13a, 1–1082. https://doi.org/NEA No. 6355

Lepillier, B, Yoshioka K., Parisio, F., Bakker R R., Bruhn D (2020). Variational Phase-field modeling of hydraulic fracture interaction with natural fractures and application to Enhanced Geothermal Systems. Earth and Space Science Open Archive, 51.

Leupin, O. X., Marschall, P., Johnson, L., Cloet, V., Schneider, J., Smith, P., Savage, D., Senger, R. (2016). Low-and intermediate-level waste repository-induced effects (No. NTB--14-14). National Cooperative for the Disposal of Radioactive Waste (NAGRA).

Leygraf, C. & Graedel, T.E. (2000): Atmospheric corrosion. ECS Corrosion Monograph Series, Wiley Interscience.

Li, D, Bauer, S., Benisch, K., Graupner, B. Beyer C. (2014). Opengeosys-chemapp: a coupled simulator for reactive transport in multiphase systems and application to CO2 storage formation in northern Germany. Acta Geotechnica, 9 (1), 67-79.

Liu, S., Jacques, D., Govaerts, J., Wang, L. (2014). Conceptual model analysis of interaction at a concrete–Boom Clay interface. Physics and Chemistry of the Earth 70–71, 150–159.

Liu, P, Zhang T., Su S. (2019) Tutorial review of reactive transport modeling and risk assessment for geologic CO2 sequestration. Computers & Geosciences, 127, 1-11.

Lothenbach, B., Kulik, D.A., Matschei, T., Balonis, M., Baquerizo, L., Dilnesa, B., Miron, G.D., Myers, R.J. (2019). Cemdata18: A chemical thermodynamic database for hydrated Portland cements and alkali-activated materials. Cem. Concr. Res. 115, 472–506.

Lothenbach, B., Matschei, T., Möschner, G., Glasser, F. P. (2008). Thermodynamic modelling of the effect of temperature on the hydration and porosity of Portland cement. Cement and Concrete Research, 38(1), 1-18.

Lothenbach, B., Rentsch, D., Wieland, E. (2014). Hydration of a silica fume blended low-alkali shotcrete cement. Physics and Chemistry of the Earth, Parts A/B/C, 70, 3-16.

Lu, R., Nagel, T., Shao, H., Kolditz, O., Shao, H. (2018) Modeling of Dissolution-Induced Permeability Evolution of a Granite Fracture Under Crustal Conditions. Journal of Geophysical Research: Solid Earth, 123, 5609-5627.

Lu, R., Nagel, T., Poonoosamy J, Naumov D, Fischer T, Shao H., Kolditz, O. Montoya V (2022) A consistent integration-point collocation scheme for1reactive transport modeling with the operator splitting approach. Computational Geosciences (submitted).

Ma, B., Lothenbach, B. (2020). Thermodynamic study of cement/rock interactions using experimentally generated solubility data of zeolites. Cement and Concrete Research, 135, 106149.

Marques Fernandes, M., Baeyens, B., Dähn, R., Scheinost, A.C., Bradbury, M.H. (2012). U(VI) Sorption on Montmorillonite in the Absence and Presence of Carbonate: A Macroscopic and Microscopic Study. Geochimica et Cosmochimica Acta 93, 262–277.

Marty, N. C., Munier, I., Gaucher, E. C., Tournassat, C., Gaboreau, S., Vong, C. Q., et al. (2014). Simulation of cement/clay interactions: feedback on the increasing complexity of modelling strategies. Transport in porous media, 104(2), 385-405.

Maxwell, R. M, Putti, M., Meyerhoff, S., Delfs, J.O., Ferguson, I.M., Ivanov, V., Kim, J., Kolditz, O., Kollet, S.J., Kumar, M., Lopez, S., Niu, J., Paniconi, C., Park, Y., Phanikumar, M.S, Shen, C., Sudicky, E.A, Sulis, M. (2016). Surface subsurface model intercomparison: A first set of benchmark results to diagnose integrated hydrology and feedbacks. Water Resources Research, 50(2):1531–1549.

McCarter, W. J., Starrs, G., Chrisp, T. M. (2000). Electrical conductivity, diffusion, and permeability of Portland cement-based mortars. Cement and Concrete Research, 30(9), 1395-1400.

Meng, B., Vienken, T, Kolditz, O., Shao, H. (2018). Modeling the groundwater temperature response to extensive operation of ground source heat pump systems: A case study in germany. Energy Procedia, 152:971–977.

Meng, B., Vienken, T, Kolditz, O., Shao, H. (2019). Evaluating the thermal impacts and sustainability of intensive shallow geothermal utilization on a neighborhood scale: Lessons learned from a case study. Energy Conversion and Management,199, 111913.

Miao, X.-Y. Kolditz, O., Nagel, T. (2019). Modelling thermal performance degradation of high and low-temperature solid thermal energy storage due to cracking processes using a phase field approach. Energy Conversion and Management, 977–989.

Miron, G.D., Kulik, D.A., Lothenbach, B., (2018). A PHREEQC version of CEMDATA'18 generated using ThermoMatch, in: Calcium-Silicate Hydrates Containing Aluminium: C-A-S-H II. Dübendorf, Switzerland.

Missana, T., García-Gutiérrez, M., Mingarro, M., Alonso, U. (2017). Analysis of barium retention mechanisms on calcium silicate hydrate phases. Cement and Concrete Research, 93, 8-16.

Nagel, T., Minkley, W., Böttcher, N., Naumov, D.Y., Görke, U.J., Kolditz, O. (2017). Implicit numerical integration and consistent linearization of inelastic constitutive models of rock salt. Computers & Structures, 182, 87–103.

NAGRA (2002): Project Opalinus Clay: Safety Report. Demonstration of disposal feasibility for spent fuel, vitrified high-level waste and long-lived intermediate-level waste (Entsorgungsnachweis). Nagra Tech. Rep. NTB 02-05.

NAGRA. (2008). Effects of Post-Disposal Gas Generation in a Repository for Low- and Intermediate-Level Waste Sited in the Opalinus Clay of Nothern Switzwerland. NAGRA-NTB--08-07.

NAGRA (2010): Beurteilung der geologischen Unterlagen für die provisorischen Sicherheitsanalysen in SGT Etappe 2: Klärung der Notwendigkeit ergänzender geologischer Untersuchungen. Nagra Tech. Rep. NTB 10-01.

NAGRA. (2014). Modellhaftes Inventar Für Radioaktive Materialien MIRAM 14. NAGRA Technischer Bericht. NAGRA-NTB 14-04: 108.

Naumov, D.Y., Bilke, L., Fischer, T., Huang, Y., Lehmann, C., Miao, X-Y. Nagel, T., Parisio, F., Rink, K., Shao, H., Wang, W., Watanabe, N., Zheng, T., Kolditz, O. (2018). Appendix a: Opengeosys6. In Kolditz, O., Nagel, T., Shao, H., Wang, W., Bauer, S. (ed), Thermo-Hydro-Mechanical-Chemical Processes in Fractured Porous Media: Modelling and Benchmarking, pages 271–277. Springer International Publishing.

Naumov, D.Y., Fischer T., Bilke, L., Rink, K., Watanabe, N., Wang, W., Lu, R., Grundwald, N., Zill, F., Huang, Y, Bathmann, J., Chen, C., Shao, H., Chen, S., Miao, X., Meng, B., Walther, M., Buchwald, J., Boog, J., Zheng, T Yoshioka, K., Zhang, N., Thiedau, J., Parisio, F., Nagel, T., Helbig, C., Kalbacher, T., Lehmann, C., Wanlong C., Herfurth, J., Montoya, V., (2020) ufz/ogs: 6.2.2, June, 2020.

Neck, V., Altmaier, M., Seibert A., Yun J., Marquardt, C., Fanghanel, Th (2007) Solubility and redox reactions of Pu(IV) hydrous oxide: Evidence for the formation of PuO2+x(s, hyd). Radiochim. Acta 95, 193–207 / DOI 10.1524/ract.2007.95.4.193

Nixdorf, E., Sun, Y., Lin, M, Kolditz O. (2017). Development and application of a novel method for regional assessment of groundwater contamination risk in the songhua river basin. Science of the Total Environment, 605-606, 598–609.

Nordstrom, D.K., Plummer, L.N., Langmuir, D., Busenberg, E., May, H.M., Jones, B.F., Parkhurst, D.L., (1990). Revised Chemical Equilibrium Data for Major Water—Mineral Reactions and Their Limitations. pp. 398–413. https://doi.org/10.1021/bk-1990-0416.ch031
Papafotiou, A. & Senger, R. (2014): Sensitivity analyses of gas release from a L/ILW repository in the Opalinus Clay in the candidate siting regions of Northern Switzerland. Nagra Arbeitsber. NAB 13-92.

Parisio, F., Naumov, D. Y., Kolditz, O., Nagel T. (2018). Material forces: An insight into configurational

mechanics. Mechanics Research Communications, 93:114–118.

Parisio, F, Vinciguerra, S., Kolditz, O., Nagel, T. (2019a) The brittle-ductile transition in active volcanoes. Scientific Reports, 9(1).

Parisio, F., Vilarrasa, V., Wang, W., Kolditz, O., Nagel, T., (2019b). The risks of long-term re-injection in supercritical geothermal systems. Nat. Commun. 10 (1), 4391.

Parkhurst, D. L., Appelo, C. A. J. (2013). Description of input and examples for PHREEQC version 3: a computer program for speciation, batch-reaction, one-dimensional transport, and inverse geochemical calculations (No. 6-A43). US Geological Survey.

Pearson, F.J., Berner, U., (1991). Nagra Thermochemical Data Base I. Core Data. Nagra Technical Report NTB 91-17. Nagra, Wettingen, Switzerland.

Pearson, F.J., Berner, U., Hummel, W., (1992). Nagra Thermochemical Data Base II. Supplemental Data 05/92. Nagra Technical Report NTB 91-18. Nagra, Wettingen, Switzerland.

Pfeiffer, W.T., Graupner, B., Bauer, S. (2016) The coupled non-isothermal, multiphase-multicomponent flow and reactive transport simulator OpenGeoSys–ECLIPSE for porous media gas storage. Environ Earth Sci 75, 1347.

Poller, A., Smith, P., Mayer, G. & Hayek, M. (2014): Modelling of radionuclide transport along the underground access structures of deep geological repositories. Nagra Tech. Rep. NTB 14-10.

Poonoosamy, J., Klinkenberg, M., Deissmann G., Brandt F., Bosbach D., Mäder, U, Kosakowskic G (2020) Effects of solution supersaturation on barite precipitation in porous media and consequences on permeability: Experiments and modelling. Geochimica et Cosmochimica Acta, 270, 43-60.

Poonoosamy J., Kosakowski, G., Van Loon L., Mäder U (2015) Dissolution-Precipitation Processes in Tank Experiments for Testing Numerical Models for Reactive Transport Calculations: Experiments and Modelling Journal of Contaminant Hydrology 177-178C.

Poonoosamy, J., Wanner, C., Alt Epping, P., Águila, J.F., Samper, J., Montenegro, L., Xie, M., Su, D., Mayer, K.U., Mäder, U., Van Loon, L.R., Kosakowski, G., (2018). Benchmarking of reactive transport codes for 2D simulations with mineral dissolution–precipitation reactions and feedback on transport parameters. Computat. Geosci. https://doi.org/10.1007/s10596-018-9793-x.

Robie, R., Hemingway, B.S., (1995). Thermodynamic Properties of Minerals and Related Substances at 298.15K and 1 Bar. U.S. Geol. Surv. Bull.

Shao, H., Hesser, J., Kolditz, O., Wang W. (2019a). Hydraulic characterisation of clay rock under consideration of coupled THM properties. Environmental Science and Engineering, 33– 40.

Shao, H., Kosakowski, G., Berner U., Kulik D.A., Mäder, U., Kolditz, O. (2013) Reactive transport modeling of the clogging process at Maqarin natural analogue site. Physics and Chemistry of the Earth, Parts A/B/C, 64, 21-31.

Shao, H., Wang, Y., Kolditz, O., Nagel, T., Brüning, T., (2019b). Approaches to multi-scale analyses of mechanically and thermally-driven migration of fluid inclusions in salt rocks. Phys. Chem. Earth 113, 1 – 13.

Steefel, C.I, Appelo, C.A.J., Arora, B., Jacques, D., Kalbacher, T., Kolditz, O., Lagneau, V., Lichtner, P.C., Mayer, K.U, Meeussen, J.C.L, Molins, S., Moulton, D., Shao, H., Simunek, J., Spycher, N., Yabusaki, S.B., Yeh G.T (2015). Reactive transport codes for subsurface environmental simulation. Computational Geosciences, 19(3), 445–478.

Stroes-Gascoyne, S. & Hamon, C. (2013): Microbial gas production from superplasticizers in shotcrete. Nagra Working Rep. NAB 13-85.

Tanger, J.C., Helgeson, H.C., (1988). Calculation of the thermodynamic and transport properties of aqueous species at high pressures and temperatures; revised equations of state for the standard partial molal properties of ions and electrolytes. Am. J. Sci. 288, 19–98. https://doi.org/10.2475/ajs.288.1.19

Thoenen, T., Hummel, W-, Berner, U.,Curti E. (2014) The PSI/Nagra Chemical Thermodynamic Database 12/07. PSI Bericht Nr. 14-04

Wagman, D.D., Evans, W.H., Parker, V.B., Schumm, R.H., Halow, I., Bailey, S.M., Churney, K.L., Nuttall, R.L., (1982). The NBS Tables of Chemical Thermodynamic Properties. J. Phys. Chem. Ref. Data

Walther, M, Graf, T., Kolditz, O., Liedl, R., Post V. (2017). How significant is the slope of the sea side boundary for modelling seawater intrusion in coastal aquifers? Journal of Hydrology, 551, 648–659.

Wang, W., Fischer, T., Zehner, B., Böttcher N., Gürke, U.J, Kolditz, O (2015). A parallel finite element method for two-phase flow processes in porous media: Opengeosys with petsc. Environmental Earth Sciences, 73(5), 2269–2285.

Wang W., Kolditz O (2006). Object oriented finite element analysis of thermohydromechanical (THM) problems in porous media. International Journal for Numerical Methods in Engineering, 69(1):162–201.

Wang, W., Kolditz, O., Nagel, T. (2017). Parallel finite element modelling of multi-physical processes in thermochemical energy storage devices. Applied Energy, 185(P2):1954–1964.

Watanabe, N., Wang, W., Taron, J., Görke, U.J, Kolditz, O (2012). Lower-dimensional interface elements with local enrichment: application to coupled hydro-mechanical problems in discretely fractured porous media. International Journal for Numerical Methods in Engineering, 90(8), 1010–1034.

Wollrath, J. (1990) Ein Strömungs- und Transportmodell fr klüftiges Gestein und Untersuchungen zu homogenen Ersatzsystemen. PhD thesis, Institut fr Strömungsmechanik und Elektronisches Rechnen im Bauwesen, Universitt Hannover.

Xie, M. L., Bauer, S., Kolditz, O., Nowak, T., and Shao, H.: Numerical simulation of reactive processes in an experiment with partially saturated bentonite, J. Contam. Hydrol., 83, 122–147, 2006.

Yapparova E., Miron G.D, Kulik D.A., Kosakowski G., Driesner T. (2019) An advanced reactive transport simulation scheme for hydrothermal systems modelling. Geothermics, 78, 138-153.

Yoshioka, K., Naumov, D., Kolditz, O., (2020). On crack opening computation in variational phase-field models for fracture. Comput. Meth. Appl. Mech. Eng. 369 , art. 113210.

Yoshioka, K, Parisio, F., Naumov, D., Lu, R., Kolditz, O., Nagel, T (2019). Comparative verification of discrete and smeared numerical approaches for the simulation of hydraulic fracturing. GEM - International Journal on Geomathematics, 10(1).

Zhu, B., Ye, Z., Wang. L, Kong, D., Xu, W., Kolditz, O., Nagel, T., Chen, Y (2020) Hydro-mechanical behavior of unsaturated soil surrounding a heated pipeline considering moisture evaporation and condensation Computers and Geotechnics 119, 103377.

ILW disposal cell in granite

Höglund L. O. (2014). The impact of concrete degradation on the BMA barrier functions. SKB Report R-13-40, Swedish Nuclear Fuel and Waste Management Company, Stockholm, Sweden.

Parkhurst D. L., Kipp K. L., Charlton S. R. (2010). PHAST version 2: a program for simulating ground-water flow, solute transport, and multicomponent geochemical reactions. Techniques and Methods 6–A35, U.S. Geological Survey, Denver, Colorado.

Samper, J. (UDC), Montenegro, L., (UDC), De Windt L. (MPT) (2021). Conceptual model formulation for a mechanistic based model implementing the initial SOTA knowledge (models and parameters) in existing numerical tools. Draft version of D2.16 of the HORIZON 2020 project EURAD. EC Grant agreement no: 847593.

Samper, J., Lu, C., Montenegro, L., (2008). Coupled hydrogeochemical calculations of the interactions of corrosion products and bentonite. Physics and Chemistry of the Earth 33, S306-S316, doi:10.1016/j.pce.2008.10.009.

Vasconcelos, R. G. W., Beaudoin, N., Hamilton, A., Hyatt, N. C., Provis, J. L., Corkhill, C. L. (2018). Characterisation of a high pH cement backfill for the geological disposal of nuclear waste : the Nirex Reference Vault Backfill. Applied Geochemistry, 89. pp. 180-189. ISSN 1872-9134.

Wilson J. C., Benbow S., Metcalfe R. (2017). Understanding the long-term evolution of cement backfills: alteration of NRVB due to reaction with groundwater solutes. RWM/03/043. RWM Report.

Wilson J.C., Benbow S., Metcalfe R. (2018). Reactive transport modelling of a cement backfill for radioactive waste disposal. Cem. Concr. Res., 111 (2018), pp. 81-93.